Politecnico di Torino

Master's Degree in Energy and Nuclear Engineering
A.y. 2020/2021

Experimental Analysis of a Hydrogen Power-To-Power System based on Solid Oxide Technology

Stack Characterization

Supervisors:

Prof. Andrea Lanzini
Dr. Matteo Testi
Dr. Martina Trini

Candidate:

Francesca Panaccione

October 2021

Abstract

In the framework of the energy transition from a world energy system based on the use of fossil fuels to a less pollutant one, the role of renewable energy is always more predominant. However, due to the intermittent nature of this energy, the renewable energy penetration requires an increasing development of the energy storage technologies. In this context, the Power-to-Power systems represent a non-conventional solution. They are electrochemical systems, based on the electrolyser and fuel cell technologies, able to convert the electrical power in an energy vector, and vice-versa. Therefore, their potentialities in a renewable based energy system are evident: they can store the excess of power in the chemical form to reconvert it when the energy demand increases.

In the present thesis, a hydrogen Power-To-Power system based on solid oxide technology has been experimentally analysed. The aim was to perform the stack characterization in both SOFC and SOEC operation modes and to define the stack round-trip efficiency, in reversible operation mode.

In order to achieve such objective, experimental tests in Fondazione Bruno Kessler (FBK) facility, in Trento, have been performed.
The test campaign has been organized to analyse the stack in two different working conditions: at variable and constant utilization factor, in order to have a detailed map of the stack behaviour in different operating conditions. During the test activity, the tests have been performed with a control voltage and a control current strategy, and the current and voltage data of the stack have been recorded.

Then, through an elaboration phase made with Python, the stack *V-I* curves have been plotted and the stack efficiencies and ASR values have been calculated.
Finally, to obtain the round-trip efficiency, a high-performance region has been defined, for the stack in SOFC and SOEC mode, associated to the area from the 60% up to the 100% of the maximum current value, in which the stack performances are optimal.
For the SOFC, the stack efficiency value in this region is comprised between 35% and 60%, while for the SOEC it stays between 58% and 90%. Therefore, the stack has shown a round-trip efficiency between 20% and 54% when it operates in reversible mode in this working condition.

Finally, the system characterization, also including the heat exchangers and the auxiliary components, has not been performed because of technical problems to the test bench.
However, some proposals of tests have been presented even for the system, with the perspective of future studies on the electrical and thermal characterization of the system in its whole.

Acronyms

AFC: Alkaline Fuel Cell

ASR: Area Specific Resistance

BoP: Balance of Plant

CC: Control Current

CV: Control Voltage

DES: Distributed Energy Storage

DMFC: Direct Methanol Fuel Cell

DoE: Design of Experiment

FU: Fuel Utilization

GHG: Green House Gas

GWP: Global Warming Potential

LCOE: Levelized Cost of Energy

LHV: Low Heating Value

LSCF: Lanthanum Strontium Cobalt Ferrite

LSM: Lanthanum Strontium Manganite

MCFC: Molten Carbonate Fuel Cell

NTP: Normal Temperature and Pressure

PEMFC: Polymer Electrolyte Membrane Fuel Cell

PFD: Process Flow Diagram

PGM: Platinum Group Metal

P2P: Power-To-Power

RES: Renewable Energy Sources

r-SOC: Reversible Solid Oxide Cell

SOEC: Solid Oxide Electrolyser cell

SOFC: Solid Oxide Fuel Cell

TES: Thermal Energy Storage

WGS: Water Gas Shift

YSZ: Yttria Stabilized Zirconia

Table of content

List of Figures

List of Tables

1.Introduction

In the last decades, the injection of CO_2 in the atmosphere has increased from 11.4 Gt per year in 1960 to 37.1 Gt per year in 2018, with a progressive increasing trend[1]. Accomplice of this result has been the industrialization process, coupled with the development of an economy based on the strong consumption of fossil fuels in many application fields, made attractive by their high energy density. In fact, different trials of approach toward the exploitation of renewable energy there have been in the past but, in every case, they have been left in advantage of the use of fossil resources, more performant and cheap.

It is sufficient to think to the development of the first electric cars, in the first years of 1900, commercialized by different automotive companies before to be substituted with the cheaper internal combustion engine cars, then became predominant. Evidently, those times were not enough mature to think about human impact on the environment and on what was the potential damage of CO_2 emissions.

However, now times are changed, and the climate change consequences are becoming more evident, with a lot of scientific studies and proofs which demonstrate the environmental risk we can face[2] [3]. The sensibility of people is increasing and a change of direction toward a more sustainable energy economy is becoming a salient topic. Nevertheless, one of the main problems of the climate change is that its consequences are not so immediate, but it is a slow damaging phenomenon. Because of this characteristic, it is hard to massively sensibilize the perception that people have about it and make them involved in urgent actions that should be done to prevent the reaching of an irreversible situation.

However, these human's reaction times change when a crisis with immediate threat must be faced. To do a recent example, during COVID-19 crisis the impact on reduction of the global energy demand and on CO_2 emissions has been huge, because of the closure of quite all the productive activities to safeguard the public health. On 8th April 2020, the emissions of CO_2 have recorded a cut of 8% with respect to the global total CO_2 emissions in 2019[4]. This fall has been bigger than during any other previous economic crisis.

Nevertheless, a solution like this is unfeasible to prevent the climate change, but it is useful to think how drastic the change in our behaviour should be to prevent critical consequences. In fact, to meet the Paris Agreement target and so to limit the global warming to less than 1.5 ˚C with respect to pre-industrial level, it would be necessary to cut CO_2 emission of 7.6% every year, with respect to 2019 global total emissions[4].

The problem is that, even if the consequences could be not so immediate, data are clear; the CO_2 concentration in the atmosphere has always followed a cyclic path over the past 400,000 years, but its value has always been between 150 and 300 ppm. Today this value overcomes 400 ppm, with an increasing of 45% with respect to pre-industrial levels[4].

The main problem of CO_2 is that it is a Green House Gas (GHG) and it lasts in atmosphere thousands of years, differently from others GHG which have a higher Global Warming Potential (GWP) but last less. Moreover, it is possible to observe that there is a relationship between the trend of CO_2 concentration and the trend of global mean temperature change: at an increase of CO_2 is associated an increase of the mean temperature. However, if the development model in the world will continue with a *business as usual* strategy, the increase of CO_2 will lead to an uncontrolled increase of the global mean temperature value, up to +5˚C in 2070 with respect to pre-industrial levels, as never happened in the past[5].

Then, considering that in Europe the 75% of CO_2 fossil emissions comes from the energy sector[6], it is important to rethink the way we produce energy and move toward a more sustainable strategy, especially if we think that the demand of energy will increase in next decades[7].

For this reason, the penetration of Renewable Energy Sources (RES) holds an important role to meet the energy demand. In this framework the European Union has developed the Green Deal strategy, to promote a new model of development which has as main goals the carbon neutrality to reach by 2050 and an economic growth dissociated from the use of resources, basing on the principle of the 'no one left behind' in the social and economic development.

The European Union (EU) Green Deal promotes an efficient use of resources and a more sustainable and circular economy, through a series of targeted investments on clean technologies and a determined action plan, exploiting part of the 800 billion of the NextGenerationEU[8] [9]. In the framework of the Green Deal, the targets for the 2030 for the European Union in its whole are the followings[6]:

- A reduction of at least 55% of GHG with respect to 1990
- A share of at least 32% of energy from RES
- An improvement in energy efficiency of at least 32.5%

To reach these goals, the European commission has defined in the National Energy and Climate Plan (NECP) the actions to implement for the period from 2021 to 2030. Each European Union country will submit a progress report each 2 years. Concerning the share of energy from RES, some EU countries have a higher share than others and in 2019 had already overcome their national target for the 2020. Between these there are Sweden, Denmark, Finland, Estonia, Bulgaria, Croatia, Island, Norway and Italy. In Italy nowadays around the 20% of all the energy consumed comes from renewable source[6].

To reach the EU targets, over the funds from the NextGenerationEU, some financing programs have been defined too by European Union, based on cooperation mechanisms between European countries: a country will finance a renewable energy project, which will be developed in another hosting country. The advantage for the financer country is that it can access to the renewable energy that is not possible to produce on its territory, because of the absence of the favourable conditions. On the other hand, the advantage for the hosting country is the presence of a renewable local investment, without affect the national budget, which brings a series of benefit, like the increase of

local employment, the decrease of local GHG emissions and the increase of renewable energy local consumption[10].

However, with the increasing production of renewable energy as collective strategy, the presence of energy storage becomes crucial, because of the unpredictable nature of renewable sources. There are different types of energy storage, which can be divided mainly in conventional and unconventional. For conventional ones we mean the electrochemical batteries and supercapacitors, while in the non-conventional group we include mainly the use of energy vectors to store electricity in chemical form. An example of energy vector can be hydrogen, produced through electrolysers exploiting the excess of electricity produced during off-peak times.

This concept can be generalized under the Power-to-X strategy, where X represents the energy vector and can be represented by a gas or a liquid produced through electric power. The energy vector is stored to be then reconverted in electric power if needed. This last operation mode constitutes a Power-To-Power (P2P) system.

A system like this represents an important reference for the increasing installation of renewables, giving flexibility to the generation of electricity and potentially generating an energy hub with multiple energy carriers and energy networks. In fact, the advantage to store electric power in an energy vector is that it can be transported in a network even for long distances to be reconverted where needed.

Moreover, a P2P system could be convenient for all those storage applications for which batteries are not suitable. This happens mainly when big amounts of energy must be stored, for example in a scenario with a big penetration of renewable power installed.

In cases of lower power, the energy losses in the storage process makes the conversion not convenient with respect to the conversion efficiency of the storage in a battery, which has higher round-trip efficiencies for the charge and discharge process.

In a study conducted by P. Marocco et al. [11], the levelized cost of energy (LCOE) in an off-grid area fed by a photovoltaic installation has been analysed and compared considering different storage options. The LCOE has resulted lower in the case of an only battery storage with respect to an only hydrogen-based storage (P2P system), because of the higher conversion efficiency. However, the cheapest solution to store the renewable energy in excess has resulted to be a hybrid storage, which include both the battery and the hydrogen-system. The battery can work as a short-term storage, while the P2P system (composed by an electrolyser and a fuel cell) can work as a long-term storage, to be used only when the battery has reached the maximum state of charge[11].

Concerning European Union's strategy, the EU is investing a lot on the hydrogen as decarbonization mean, as it represents an important part of the Green Deal. The strategy consists in promoting the use of hydrogen to decarbonize all the applications for which electrification is not possible and fossil fuels are used, like in the heavy-duty vehicles, and for the double function to store the excess of renewable power and reproduce green power when is needed, with the development of P2P systems hydrogen-based.

The key factor is that all the hydrogen used must be produced in a sustainable way. The production methods taken into account by the European investment plan are water electrolysis using renewable power, steam reforming from the biomethane produced through anaerobic digestion and finally hydrogen production from the syngas obtained through biomass gasification.

Considering Power-To-Gas-To-Power systems, they are usually based on the fuel cell and electrolyser technology. The electrolyser allows the production of a fuel gas, receiving as input electric power, while the fuel cell allows the generation of electric power starting from a fuel gas. The combination of these two elements can compose a Power-To-Power system, which become interesting if the electrical power involved is produced by renewable source.

There are different types of fuel cells and electrolysers, depending on the electrolyte's materials with which they are realized and so on the temperature they can work.

In section 1.1 and 1.2 an overview of the main fuel cell and electrolyser technologies available and under research-studies nowadays will be presented.

1.1 Fuel cells

Firstly, we can make a division between low temperature (between 60°C and 80°C) and high temperature fuel cell (between 690 °C and 800 °C)[12].

The main fuel cell types working at low temperatures are the Polymer Electrolyte Membrane Fuel Cell (PEMFC), the Alkaline Fuel Cell (AFC) and the Direct Methanol Fuel Cell (DMFC), while for high temperatures the main types are the Solid Oxide Fuel Cell (SOFC) and the Molten Carbonate Fuel Cell (MCFC).

For what concern the high temperature fuel cells, they are better in terms of performances and fuel flexibility. On the other hand, they are more expensive than the low temperature cells and worst in terms of dynamic performances. For this reason, low temperature fuel cells are used for automotive application, in which fast start-up times are required. In particular, fuel cells in automotive are interesting especially for heavy duty vehicles which require big power and for which batteries wouldn't be suitable.

Moreover, the future trend for the low temperature fuel cells is to increase the level of temperature to improve the performances, while for the high temperature fuel cells the trend is to decrease the operating temperature, to decrease the cost of materials used and reduce degradation.

The total electrochemical reaction which takes place in the fuel cell for the power production is the following:

$H_2 + \dfrac{1}{2}O_2 \rightarrow H_2O$	(1)

1.1.1 Low temperature fuel cells

Focusing on the low temperature fuel cells, the PEMFC can work only with quite pure hydrogen as fuel, which is sent to the anode, while air is sent to cathode. The electrolyte is made with a polymer containing SO_4^{2-} ions able to solvate a big amount of water, which allows to transport ions H^+. Therefore, the half reactions which take place at anode and cathode are respectively:

$H_2(g) \rightarrow 2H^+ + 2e^-$	(2)

$\dfrac{1}{2}O_2(g) + 2H^+ + 2e^- \rightarrow H_2O(l)$	(3)
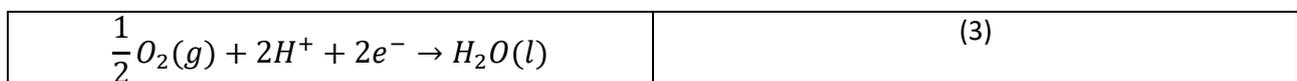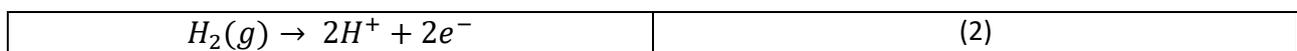
Usually, the material used for the electrolyte is Nafion. It is a polymeric molecule obtained from a molecule called Poly Tetra Fluor Ethylene (PTFE, with chemical formulation $(CF)_n$), also known as Teflon, which then is modified adding a lateral chain containing HSO_3. Then we have to consider that Teflon is hydrophobic while HSO_3 is hydrophilic and so the ion H^+ conductivity is enhanced if the Nafion is humidified. To do this, the inlet air has to be humidified.

Then, due to the low temperature, the kinetic of the electrochemical reactions is low. So, for this reason precious and expensive catalysts are needed: the most used catalysts are Platinum Group Metals (PGM). It is well known that platinum suffers from contamination by carbon compounds

which can deactivate it, because in presence of them it would catalyse carbon deposits. Therefore, PEMFCs are not fuel flexible and need to operate with high hydrogen purity (different levels of hydrogen can be identified on the basis of the purity, and of course to higher level of purity corresponds higher costs).

Another type of low temperature fuel cell spread in the application field since the 60s is the Alkaline Fuel Cell (AFC). In this case the electrolyte is a liquid, composed by an alkaline solution of KOH or NaOH in water, and the ion OH$^-$ is conducted. The problem for this cell is the CO_2 present in the air which reacts with the liquid electrolyte forming carbonates. The formed carbonates could precipitate on the electrodes, blocking their pores, and could reduce the conductivity of the electrolyte, reducing consequently the performances of the cell.

The AFC is the oldest type of fuel cell developed, and therefore the most mature, which now is being considered again because of its good values in efficiency. A stack electric efficiency of 42% has been reported by L.Q. Wang et al [13].

Moreover, the advantage of AFCs with respect to the PEMFCs is in the cost: in the AFCs the kinetic of the reaction is enhanced and so there is no need to use precious metals as catalysts. Therefore, the AFCs represent the cheapest solution on the market, and they are the most diffused fuel cells nowadays, while research goes on trying to obtain always more efficient cells at always lower costs, especially in the high temperature field, interesting for cogeneration purposes.

The electrochemical reactions at anode and cathode in the AFC are respectively:

$2H_2(g) + 4OH^- \rightarrow 4H_2O(l) + 4e^-$	(4)

$O_2(g) + 2H_2O(l) + 4e^- \rightarrow 4OH^-$	(5)
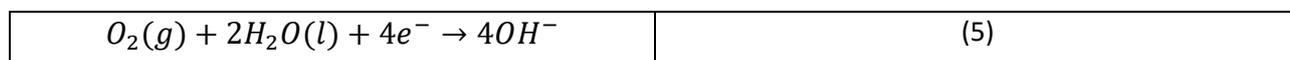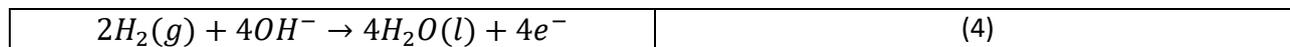
Finally, the Direct Methanol Fuel Cells (DMFCs) are another type of low temperature fuel cells. In this case the fuel is methanol, which is an alcohol. The advantage is the high energy density per unit of volume of the fuel, higher than in the case of hydrogen. One of the main problems of this type of cell is the cross-over of methanol, which means the permeation of methanol through the electrolyte membrane, from anode to cathode, without react. This causes a decrease in the power production and in the efficiency value. Typically, stack electric efficiency is around 30%[14] but there are several studies to improve it[15,16].

The typical operating temperatures are between 50 ˚C and 120 ˚C and the streams usually are not pressurized to avoid leakages which decrease the efficiency value.

In DMFCs at the anode is injected a solution of methanol and water, while at cathode air is provided. The electrochemical reactions produce CO_2 at anode and water at cathode, which is recycled to be injected at the anode. The ion H$^+$ is transferred in the electrolyte formed by a Nafion membrane while the electrons are transferred through the external circuit providing electrical power. The power produced is not very high and so the applications of the DMFCs are limited for small devices, like portable electronics, but the potential of this type of fuel cells stays in the high energy density per unit of volume of fuel.

The anode and cathode electrochemical reactions are respectively:

$CH_3OH(l) + H_2O(l) \rightarrow CO_2(g) + 6H^+ + 6e^-$	(6)

$6H^+ + 6e^- + \dfrac{3}{2}O_2(g) \rightarrow 3H_2O(l)$	(7)

1.1.1 High temperature fuel cells

For what concern the high temperature fuel cells, Solid Oxide Fuel Cells (SOFCs) are the most promising. The electrolyte is realized with a ceramic material (oxide of transition metal or rare earth material). This is a big family of materials, but some ones dominate the market, like zirconia oxides (ZrO_2) doped with yttria (Y_2O_3), known as Yttria-Stabilized Zirconia, (YSZ). The temperature of operation must be quite high in this type of cells because ceramic materials have a sufficient ion conductivity σ only at quite high temperatures.

Moreover, the ion O^{2-} is transferred from cathode to anode in the electrolyte during the electrochemical reactions, while water is produced at anode side. The two half electrochemical reactions in SOFC are reported below, at the anode and at the cathode side, respectively, in the case of hydrogen as fuel:

$H_2(g) + O^{2-} \rightarrow H_2O(g) + 2e^-$	(8)

$\dfrac{1}{2}O_2(g) + 2e^- \rightarrow O^{2-}$	(9)

One of the main advantages of high temperature fuel cells is that transport phenomena are enhanced with respect to the low temperature case, so the over-voltages are lower, the polarization of the cell is better and as consequence the efficiency values are better with respect to the low temperature case. System electric efficiency for SOFCs is around 50 ÷ 55%, for a wide range of output net electric power, as reported by H. Langnickel et al. in an efficiency study on SOFC systems installed in a waste water treatment plant[17]. Therefore, the efficiency value is not bound to the power output, and it is possible to perform power modulation maintaining high efficiency performances, differently from what happen with the power generation with the turbines and the combustion engines.

Moreover, with the SOFCs, because of the improvement of transport phenomena there is no need of precious catalyst at anode, but the most industrial and cheap one can be used, which often is nickel. Nickel is also more tolerant for molecules containing carbon and this means that fuel flexibility is guaranteed for high temperature fuel cells.

Another important advantage is that there is availability of heat at high temperature which can be exploited for Combined Heat and Power (CHP) applications or through the hybridization of the fuel cell with another machine, like a gas turbine or a steam turbine which can use the high temperature exhausted gas to produce additional power, increasing the electrical efficiency of the system.

System efficiencies over 70% are expected to be obtained with these configurations, while up to now system efficiency up to 67% is reached with a system composed by a SOFC and a steam turbine, in which the exhaust heat of the fuel cell is used to produce the steam necessary for the Rankine cycle[18]. Then there is to say that the efficiency value depends on the layout of the hybrid system.

Even with cogeneration, the performances of the SOFC system are better. The waste heat of the SOFC can be used in building applications or in energy requiring units in the plant, like preheaters or steam reforming (in the case of fuel cells fed with natural gas), reducing the thermal energy input. Zink et al.[19] analysed a system composed by a SOFC integrated in a building for the production of electric power, heating and cooling. The system efficiency in this case has reached a value over 87%.

Despite the good performances, high temperature cells present even some disadvantages. For example, at higher temperatures there is also higher degradation of materials and so shorter life of the stack and of the Balance of Plant (BoP). M.V. Ananyev et al.[20] have analysed symmetric cells realized with Lanthanium, doped with Strontium, Manganese oxide and YSZ (LSM-YSZ) composite material and YSZ electrolyte, and have carried out the tests at 850 ˚C with a partial pressure of the oxygen equal to 10^{-2} atm, for 1000 h. They have observed changes in the microstructure of electrodes, related to the particles coarsening of the LSM phase. This has caused the degradation of the kinetic of the LSM-YSZ cathode material, with a consequent decrease of its performances in the reaction with the gaseous oxygen.

Ananyev et al. have also analysed the electrochemical activity of the cell and have noticed that the polarization conductivity and resistance decrease over time. They have reported that to a decrease of 15% of the value of the oxygen coefficient of surface exchange corresponds a decrease of 50% in the electrochemical activity of the cell. This underlines as the degradation of electrodes' material is only a part of the degradation process of the SOFCs.

Concerning the materials, usually for the anode a cermet is used, which means the union between a ceramic material (YSZ) and a metal (often nickel for catalytic activity). The electrodes' materials must ensure good catalytic activity and good electronic conduction, and at the same time they must be porous enough, (porosity $\varepsilon=30\%$) to guarantee the diffusion of molecules, but also the mechanical stability. Then, it is important to have thermo-mechanical compatibility between electrolyte material and electrodes' materials, to avoid the break of the cell in the case one material expands more than another.

For cathode usually LSM is used, which stay for Lanthanium, doped with Strontium, and Manganese oxide (LSM, $(La_{1-x} Sr_x) MnO_3$). It is a perovskite, which is a family of ceramic materials with structure ABO_3, with A and B which are two cations of different dimensions. It is able to conduct well both electrons and ions.

In the stack, the cells are connected through interconnector plates made with CROFER 22C APU, which is a stainless steel with 22% of chromia. It must have similar thermomechanical behaviour of the ceramic material composing the cells and it must be able to work at 700 ˚C. Nevertheless, in contact with O_2 it generates chromia oxide C_rO_2 which deposits over the surface of cathode, causing

the deactivation of the electrode. The solution consists in coating the interconnector with M_nCoO_5 to avoid chromia evaporation.

Another type of high temperature fuel cell is the Molten Carbonate Fuel Cell (MCFC). In this case the electrolyte is a liquid, composed by a molten salt like K_2CO_3 or $NOCO_3$.

The fuel is injected at anode while at cathode is sent O_2 and CO_2. The ion transferred in the electrolyte is CO_3^{-2} and as products of the electrochemical reactions H_2O and CO_2 are obtained at anode. The CO_2 produced at the anode can be separated from the H_2O through condensation and can recirculate to be injected at the cathode; in this way the machine can work even without a CO_2 source.

This type of cell is fuel flexible, but it shows lower efficiency than SOFC. Typical system electric efficiency values are around $43 \div 47\%$, depending also on fuel type[21]. The operating temperature is between 550 ˚C and 650 ˚C.

The electrochemical reactions in MCFCs are the followings, in the case of hydrogen used as fuel.

At anode:

$\begin{aligned} H_2(g) \rightarrow 2\,H^+ + 2e^- \\ 2\,H^+ + CO_3^{-2} \rightarrow H_2O(g) + CO_2(g) \end{aligned}$	(10)

At cathode:

$\frac{1}{2}O_2(g) + CO_2(g) + 2e^- \rightarrow CO_3^{-2}(g)$	(11)
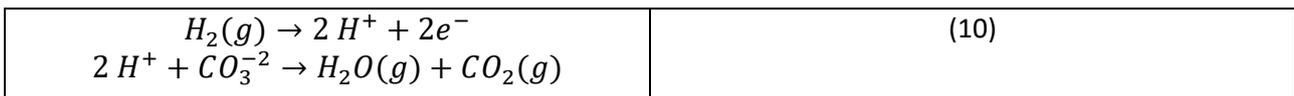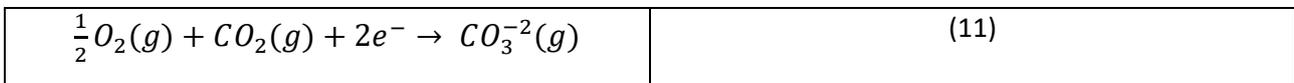
The advantage of a MCFC is that it can concentrate CO_2 and work even with a low concentration cathode CO_2 flow, like a flue gas. Therefore, this type of fuel cell can be considered to recover the CO_2 in the flows in which the concentration is low and the carbon capture with the conventional methods would be difficult.

In South Korea there is a fuel cell-based power generation system, which exploit MCFC technology, managed by POSCO company. It is the largest fuel cell plant in the world, with a power equal to 60 MW composed by a series of MCFCs[22].

However, for what concern the high temperature fuel cells, the long start-up and shut-down times of this types of machines (up to few hours) make them not suitable for automotive application but only for base load production of power and heat recovery.

1.2 Electrolyser

For what concern electrolysers, the EU investment strategies for the next decades show the explosion of interest that there is for this technology and for the production of green hydrogen, considered one of the driving elements for the energy transition. The European Union has planned to invest an amount between 180 and 450 billion of euros up to 2040 in hydrogen technologies, to install an extra power for electrolyser equal 40 GW up to 2030[23].

1.2.1 Hydrogen - Final uses

Hydrogen market is very big, with many application fields: it can be used to produce power and heat (through fuel cells technology), as fuel in the transport sector, as feedstock in industry (for the production of steel, concrete, glass, food and cosmetic products for example) and for the production of synthetic chemicals (like ammonia, used typically as fertilizer, alcohols and fuels like syngas).

In industrial applications, in Europe, the biggest consumption of hydrogen is addressed to oil distillation (33%), followed by ammonia production (27%), methanol production (11%) and steel production (3%)[24], for which hydrogen represents an opportunity to decarbonize this process, that in most cases is done using coal. Moreover, in the future the demand of ammonia and methanol is estimated to increase and even for this reason is important to rethink to the way used to produce hydrogen and do it in a sustainable way.

1.2.2 Hydrogen – Production methods

Hydrogen is not a primary source, but it must be produced. Traditionally it is obtained mainly from fossils which contain atomic hydrogen in their molecule, like coal, oil and natural gas. Between them, natural gas nowadays is the most considered hydrogen source, as it contains a lot of atomic hydrogen in its molecule. However, new and more sustainable ways to produce it are in development in the last years, some more innovative than others, to allow the construction of a hydrogen-based and clean energy system.

Based on the production method, hydrogen can be divided in four categories: green, blue, grey and brown.

The brown hydrogen is those produced starting from a fossil source, like coal and oil. In the case of coal, it is produced through the gasification process and the production of syngas, from which hydrogen is separated. In the case of the oil, it is obtained as subproduct of cracking processes.

The grey hydrogen is produced from natural gas through the steam reforming process. The first step consists in the desulphurization of the natural gas. Then, the clean gas is made to react with steam: from this steam reforming reaction, reported below, hydrogen and carbon monoxide are produced[25].

$CH_4(g) + H_2O(g) \rightarrow 3H_2(g) + CO(g)$	(12)
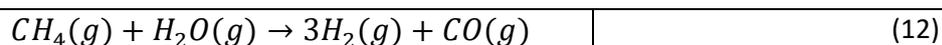
This is an endothermic reaction, which takes place at high temperatures ($T\sim800\ °C$) with an enthalpy required equal to $\Delta h = +206\ \frac{kJ}{kg}$. Usually, to thermally feed the reaction a part of gas is burned in a burner, providing the heat required.

The composition of the output stream at this point is the following: 43%$_v$ H_2, 7%$_v$ CO, 42%$_v$ H_2O, 6%$_v$ CO_2, 2%$_v$ CH_4. The stream is cooled down and the Water Gas Shift (WGS) reaction takes place, to convert the carbon monoxide (which is an unstable molecule) and to increase the hydrogen quantity.

Water gas shift reaction[25]:

| $CO(g) + H_2O(g) \rightarrow H_2(g) + CO_2(g)$ | (13) |
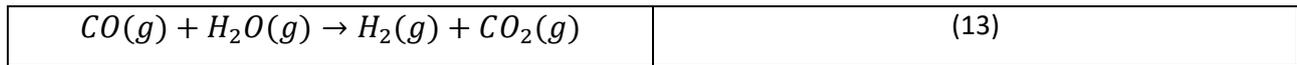
This reaction is exothermic, and the equilibrium is shifted toward products at low temperatures ($T=200\div300\ °C$). The heat obtained from this reaction can be used for the water evaporation, to obtain the steam for the steam reforming reaction.

As output of the WGS reaction, pure hydrogen is not obtained, and the stream is a mixture of mainly H_2, H_2O and CO_2. Pure hydrogen is obtained after a condensation and a clean-up section, realized with adsorption processes (Pressure Swing Adsorption or Temperature Swing Adsorption).

Therefore, the global reforming reaction is defined as follows:

| $CH_4(g) + 2H_2O(g) \rightarrow 4H_2(g) + CO_2(g)$ | (14) |
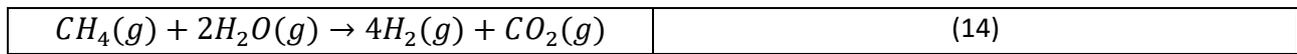
The efficiency of this hydrogen production process is between 60% and 80% (for big plant) and it is defined as follows[25]:

| $\eta_{H_2\ production} = \dfrac{G_{H_2}.LHV_{H_2}}{G_{NG}.LHV_{NG}}$ | (15) |

G_{H_2} and G_{NG} are the mass flow rates of hydrogen and natural gas, while LHV_{H_2} and LHV_{NG} are their low heating values, respectively.

Concerning the blue hydrogen, it is produced from a fossil source but doing carbon capture of the emissions released in the production process.

Finally, the green hydrogen is produced exploiting a renewable source. The most consolidated method is to use the renewable electric energy, produced by a solar, wind or water source, in an electrolyser, using water as feedstock.
The electrolyser can represent a mean to store the excess of renewable energy in off-peak period, in which the production overcomes the demand. Coupled with a fuel cell stack, it can allow the use of the hydrogen as energy vector in Power-to-Power systems.
The diffusion of this types of energy systems could allow a progressive integration of RES in the energy scenario, where hydrogen represents an energy vector which can be transported and reconverted in electrical power when and where needed. This perspective of mobile storage can

give great flexibility to the energy systems, enhancing the penetration of Distributed Energy Sources (DES) in the society.

To realize an energy architecture like this, it is important to have a consistent renewable power installed. In fact, considering that to split water in Normal Temperature and Pressure (NTP) conditions, corresponding to 25 °C and 1 atm, it is not possible to spend less than 3,002 $\frac{kWh}{Nm^3_{H_2O}}$ and that are necessary 0.9 $\frac{l_{H_2O}}{Nm^3_{H_2}}$, for each Nm^3 of hydrogen produced are necessary minimum 2.7 Wh (the energy consumed depend on the operation voltage. Minimum energy is referred to open circuit voltage condition).

However, one problem for a system like this fed with intermittent energy is present in the case high temperature cells are used (like SOEC and SOFC). In fact, they do not work very well with fast load variations, typical of renewable energy production, mainly because of their thermal inertia.

Other methods for the green hydrogen production, which uses water as feedstock, are the chemical looping and the photocatalysis. They use both the solar energy as renewable energy source but, in the case of chemical looping, the solar energy is concentrated to obtain high temperature heat, while, in the case of photocatalytic process, direct photons are used.

Finally, another way to produce green hydrogen is from biomass. There are two possible processes. In case of cellulosic biomass, hydrogen can be obtained through the thermochemical gasification process (as from coal, in the case of brown hydrogen).

In case of less aggregate biomass (like zootechnical, agricultural and food wastes), it is subjected to a biochemical process, though the anaerobic fermentation which allow to obtain biomethane from which hydrogen is produced (see steam reforming process in the description of grey hydrogen production). In this case the production of hydrogen is emission free. In fact, the CO_2 emitted in the process is considered biogenic, as it is the same CO_2 that the biomass has absorbed during its life cycle.

Looking at the current hydrogen production scenario, in 2019 the total demand of hydrogen in the world has been 70 $\frac{Mtonn}{year}$, of which the 76% produced from natural gas (grey hydrogen) and the 22% from coal (brown hydrogen). Less than the 0.7% has been produced from RES (green hydrogen)[24]. In Europe, nowadays the 96% of the total hydrogen is produced from natural gas. The reference cost for hydrogen produced from natural gas is around 1.5 $\frac{€}{kg}$, while the cost for blue hydrogen production, from natural gas with total carbon capture now stays around 2.5 $\div$ 3.5 $\frac{€}{kg}$. For the green hydrogen production, the cost nowadays stays around 5 $\div$ 10 $\frac{€}{kg}$, but it depends on the renewable energy source and the method used for its production[26]. The aim for the green hydrogen is to reach the cost parity with the grey hydrogen. Thanks to the decreasing trend of the cost of wind and solar energy, the prospects for the green hydrogen cost bode well.

So, in the framework of the analysis and study of a P2P system, between all the methods to produce hydrogen, the attention in next paragraphs will be focused on the main electrolysers' technologies, to present an overview on the state of the art.

The global reaction for the water splitting in water electrolyser is the following:

| $$H_2O \rightarrow H_2 + \frac{1}{2}O_2$$ | (16) |
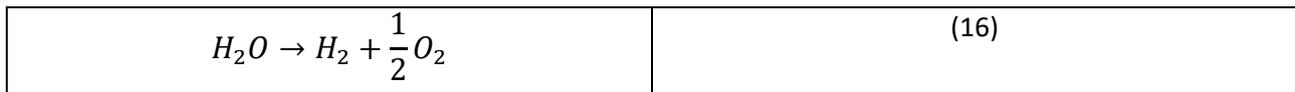
Even for the electrolysers, as for the fuel cells, a distinction can be made between low temperature and high temperature electrochemical cells.

1.2.2 Low temperature electrolysers

The operation temperature in this type of electrolyser is between 60 °C and 80 °C[27].

The main low temperature electrolyser types are the Polymeric Electrolyte Membrane (PEM) ones and the alkaline electrolyser.

In the PEM electrolyser, like in the PEMFC, the electrolyte is made in Nafion, while the catalyst material is a precious metal. Usually, it is different from that used in PEMFC, because of the different kinetic of the reactions which happen in fuel cell and electrolyser mode.

The main anode catalysts used in PEM electrolysers are ruthenium, iridium and their oxides while at cathode usually platinum or palladium are used. These catalysts are often used in nano-particle form to increase the active surface.

Ruthenium oxide RuO_2 based catalyst suffers from instabilities problems at high overpotential while iridium oxide IrO_2 has appeared as one of the most stable anode catalyst for PEM electrolyser[28]. Moreover, the use of a catalytic support material can improve the performances of the catalyst. The reasons can be found in the prevention of catalyst's particles agglomeration and so in the increase of the active surface of catalysis. The choice of a catalyst support material represents a challenge for the electrolyser cells. In fact, with respect to the fuel cell, the electrolysers are subjected to higher anode overpotentials and so to higher degradation risk for the anode catalyst support materials. However, silicon carbide material has shown good stability as support material even in electrolyser mode, improving the performance of the IrO_2 catalyst[28].

For what concern the cathode catalyst, S.A. Grigoriev et al. have analysed the electrochemical performances obtained with palladium catalyst and platinum catalyst. The catalytic activity of palladium resulted slightly lower than that measured with platinum, but however palladium can be considered as a good catalyst substitute of platinum[29].

In literature are present even some studies which try to find other possibilities for catalyst materials, able to maintain good performance as precious catalyst but also to make hydrogen production more economic. One of this is the molybdenum disulphide MoS_2 in nano-capsule morphology, which has a high exposed surface area. S.M. Senthil Kumar et al.[30] have tested this catalyst material coated on the Nafion electrolyte and, after 200 h of operation, no degradation has been noticed.

Moreover, the PEM electrolyser can work even at intermediate temperature levels, above 100 °C, with the steam electrolysis instead than water electrolysis. In this case the materials used are different with respect the low temperature PEM electrolysers because they need more severe corrosion resistance requirements. At intermediate temperatures, for what concern the electrolyte, the electrical conductivity of Nafion strongly decreases above 100 °C, therefore other materials

must be used. The most considered is the polybenzimidazoles (PBI) membrane doped with phosphoric acid. PBI is a polymer resistant to high temperatures and for this reason used also in aerospace applications and in the production of fireproof fabrics. The bipolar plates in low temperature PEM are typically made with titanium. However, at higher temperatures, titanium shows a very poor resistance to corrosion, while stainless steel appears as the most suitable material[31].

The electrochemical reactions for PEM water electrolyser at anode and cathode are respectively:

$H_2O(l) \rightarrow \frac{1}{2}O_2(g) + 2H^+ + 2e^-$	(17)

$2H^+ + 2e^- \rightarrow H_2(g)$	(18)
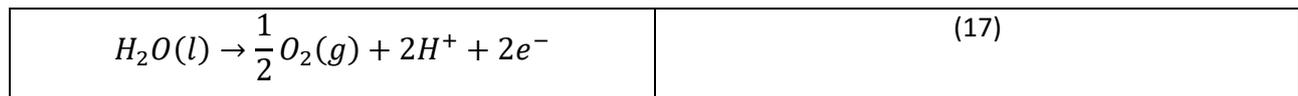
Another low temperature electrolyser is the alkaline one. Like in the AFC, it uses a liquid electrolyte which is an alkaline solution of KOH or NaOH in water. The liquid electrolyte has not good abilities in ion conduction, so the electrolyser must work at lower currents with respect to the PEM one to avoid too high ohmic drops.

The electrode materials employed usually are graphite or low-quality stainless steel (the operating temperature is not too high, so low-quality materials can be used). Due to the low-cost materials, this type of electrolyser is quite cheap, and it is very spread in the market.

However, the stainless steel can't withstand too high concentration alkaline solutions because of corrosion problems. In fact, if the voltage is higher than 1.6 V per each cell, the stainless steel can generate ferrous oxide Fe_3O_4 and hexavalent chromium Cr^{6+}, generated when the chromium contained in the stainless steel is electro-oxidized at the anode[32]. Typical voltages stay between 1.8 V and 2.4 V per cell. Therefore, a solution can be the electro-deposition of nickel on the anode electrode: as studied by R.G. Gonz alez Huerta et al.[32], this techniques has demonstrated to reduce the Cr^{6+} concentration during the operation of electrolyser, reducing as consequence the contamination of electrolyte and the maintenance time. These aspects compensate the higher cost to face for the nickel deposition.

Another study carried out by A. Cruden et al.[33] has tested the performances of two nickel electrodes, with different catalyst materials (Molybdenum Resorcinol Formaldehyde MoRF and the carbon-platinum C-Pt). The electrodes with different catalysts have not showed significant performance's differences, but from the economic point of view the choice of the MoRF catalyst can be preferred, because less expensive than the carbon-platinum one.

The typical operation range of this electrolyser type is between 40 and 90 °C, with a stack electric efficiency between 70 and 80%[27].

One of the main disadvantages of the alkaline water electrolyser is the limited current density, around 0.4 A/cm^2 and the low operating pressure and temperatures[27].

The electrochemical reactions for alkaline electrolyser are the followings.

At anode:

$$2OH^- \rightarrow \frac{1}{2}O_2(g) + H_2O(l) + 2e^-$$	(19)

At cathode:

$$2H_2O(l) + 4e^- \rightarrow 2OH^- + H_2(g)$$	(20)
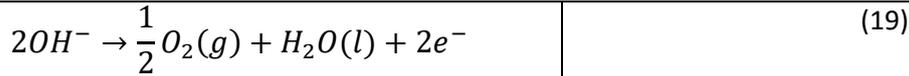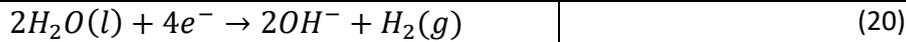
1.2.3 High temperature electrolysers

Solid oxide electrolyser (SOE) is a high temperature working electrolyser. Electrochemical reactions for steam electrolysis are the followings:

At anode:

$$O^{2-} \rightarrow 2e^- + \frac{1}{2}O_2(g)$$	(21)

At cathode:

$$H_2O(g) + 2e^- \rightarrow H_2(g) + O^{2-}$$	(22)
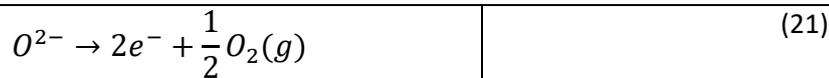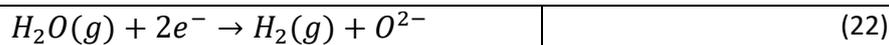
The electrolyte in SOE is a ceramic (YSZ is the most used) like in the SOFC. In fact, the SOE is the same machine of the SOFC, which can operate in reversible mode. So, even in this case, because of high temperatures and good kinetics, precious catalysts are not needed, and nickel can be used. The presence of nickel at cathode electrode allows to the SOE to be tolerant toward carbon molecules and so to split even CO_2, beyond H_2O[34]. The total reaction for the splitting of CO_2 is the following:

$$CO_2(g) \rightarrow CO(g) + \frac{1}{2}O_2(g)$$	(23)

Even the simultaneous splitting of CO_2 and H_2O is possible, to obtain the production of syngas at cathode (H_2+CO). The single reactions, at anode and cathode, in case of simultaneous production of hydrogen and carbon monoxide in a SOE are reported below.

At anode:

$$O^{2-} \rightarrow 2e^- + \frac{1}{2}O_2(g)$$	(24)

At cathode:

$$H_2O(g) + 2e^- \rightarrow H_2(g) + O^{2-}$$ $$CO_2(g) + 2e^- \rightarrow CO(g) + O^{2-}$$	(25)
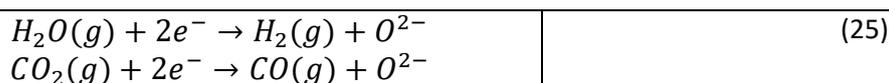
Concerning the cathode materials, a typical cathode in SOE is made with a composite of nickel and yttria-stabilized zirconia (Ni-YSZ). The problem of this material is that it requires a continuous supply of reducing gas, as hydrogen or carbon monoxide, to maintain the nickel in the reduced state[35]. The continuous supply condition is not respected with intermittent energy supply in the framework of

renewable energy feed in a P2P system. Therefore, new materials for cathode electrode are under investigation[36,35].

Anode electrodes in SOE typically are made with LSM perovskite material.
J.C. Grenier et al.[37] have analysed the performances in reversible mode of a solid oxide electrolyser with a Neodymium nickelate Nd_2NiO_4 and have compared them with those of classical LSM anode electrode. The performances of the cell with Neodymium nickelate electrode have resulted to be better for temperatures below 800 ˚C.
Another material tested for air electrode in SOE is $La_{0.75}Ca_{0.25}Fe_{3-\delta}$ (LCF7525)[38]. It has shown to be a proper material for air electrode and as advantage with respect to LSM it is strontium free, which is an element difficult to manage because extremely flammable.

The SOE up to now is less commercialized than the other electrolysers because it has the highest costs due to the materials used, which must be resistant at high temperatures. It has a lower technology readiness level (TRL) and so far, units up to 100 kW have been realized.
However, it is the best in terms of performances (it produces the same amount of hydrogen consuming less electrical power), because of the enhanced kinetic due to higher temperatures and lower operating voltages. M. Noro et al.[39] have showed a primary energy saving of 45% on hydrogen production with respect to a PEM electrolyser. Stack efficiencies with SOEC technology varies between 70 and 90%[27].

1.3 Present research framework on Reversible Solid Oxide Cells (r-SOC)

In this section, the attention will be focused on the solid oxide technology, and in particular on the reversible operation mode of the solid oxide cells (r-SOC).

In fact, concerning the study carried out in this thesis of a P2P system based on the solid oxide technology, some works already present in literature on the reversible operation of solid oxide cells are presented. Some reference values on the actual performances and an indication on what has been already analysed and what needs to be deepened will be presented.

Ferrero et al.[40] have developed, calibrated and validated using experimental data a thermo-electrochemical model for the simulation of *V-I* curves of reversible solid oxide cells working with H_2/H_2O, considering commercial-size cells with the air electrode made with different materials.

From the experimental side, two different types of commercial planar and circular-shaped solid oxide cells have been considered for model calibration and validation. The two cells have the same fuel electrode, realized with nickel/zirconia cermet (Ni/8YSZ), but different materials for the air electrode: in one case the material is Lanthanum Strontium Manganite/Zirconia (LSM/8YSZ), in the other is Lanthanum Strontium Cobalt Ferrite (LSCF).

The model is implemented in MATLAB®. Both the electrochemical and thermal modules are modelled, and the calculation of the heat sink/source term is performed by the electrochemical model and then is given as input to the thermal model.

The electrochemical module simulates the current-voltage characteristic of the cells in both operation mode, SOFC and SOEC. To do this, it must take into account the mass transport of gases and the electrochemical phenomena which occur at electrodes.

The model is validated with experimental tests, in which cells voltage is measured, varying the current with steps of 1 A maintained for 60 s each and generated with a DC power supply. The tests have been done at two different temperatures, 800 °C and 850 °C, measured with a thermocouple located in the fuel inlet electrode channel, and for different humidity values of the mixture injected at fuel cathode. The fuel electrode has been fed with $500 \frac{Nml}{min}$ of the mixture H_2/H_2O while the air electrode has been fed with $1500 \frac{Nml}{min}$ of dry air.

From the experimental tests, the *V-I* curves have been obtained for both the cell types. The cell with the LSCF air electrode has shown better performances than the cell with LSM electrode, in both SOFC and SOEC operation, for all the humidity values analysed in the fuel mixture. In fact, the area specific resistance (ASR) value of the LSCF cell at 800 °C is still lower than the ASR value of the LSM cell at 850 °C, considering a composition H_2/H_2O equal to 50%/50%. Nevertheless, the LSCF cell has shown an asymmetric behaviour between the SOFC and SOEC polarization. This is in accordance with other studies present in literature[41].

Momma et al.[41] in their study analysed the characteristics of the current-voltage curve of SOEC and SOFC. They have considered a cell with YSZ electrolyte, on which is deposited Ni/YSZ powder for negative electrode and perovskite oxides for positive electrode, made with a mixture of LSM ($La_{0.9}$ $Sr_{0.1}$ MnO) and LSC (Sr-doped lanthanum cobaltite).

Polarization curves have been measured with voltage-controlled method, with steps of 1 mV/s. Even in this case an asymmetry between the curve of SOEC and SOFC has been noticed, which has been

mostly attributed to the characteristics of the negative electrode (so to the behaviour of hydrogen and steam formation reactions in SOFC and SOEC operation, respectively). To check the origin of asymmetry, the behaviour of negative electrode has been tested and even in this case a strong asymmetry in its polarization has been noted. It has been shown a limited current behaviour in the electrolysis operation and not in the fuel cell mode.

Some studies have been done also on the thermal self-sustainability of the system in reversible operation. S. Santhanam et al.[42] have investigated a r-SOC system, in which the heat produced by exothermic reactions in fuel cell mode is exploited in endothermic reactions in electrolyser mode and in the heating-up of the inlet streams, though a thermal energy storage (TES) consisting in a phase change material. It allows to the system to reach the thermal self-sustainability, without using external energy to sustain the system. The r-SOC system analysed in this study produces syngas in electrolyser mode and use it in fuel cell mode to produce electricity. Moreover, a methanation reactor is present: in fuel cell mode it produces the syngas useful for the fuel cell, through an endothermic reaction (taking the heat from the thermal storage), while in electrolyser mode it uses the syngas produced to obtain biomethane, through an exothermic reaction (injecting heat in the thermal storage).
The efficiency reached with a configuration like this in the reference conditions of the system is equal to 54.3%, while working out of the reference conditions a system efficiency of 60.4% can be achieved.

M. Frank et al.[43] have analysed the performance of a solid oxide cell system working in reversible mode, operating with hydrogen and steam. The model of the system has been developed and the round-trip efficiency has been calculated. In the basic configuration of the system, it is equal to 45.6%. Then, in order to achieve a higher system efficiency, the plant has been integrated with an internal system of heat recovery (storing the heat produced in fuel cell mode to use it in electrolyser mode) and the hydrogen produced has been stored in compressed tanks. This has led to an increase in the efficiency, up to the value of 51%.

Khalili et al.[44] have analysed a natural gas fed SOFC system integrated downstream with a SOEC system, which uses the fuel cell anode off-gas to produce syngas. The electric power to the electrolyser is provided by a renewable source, through an organic Rankine cycle based on solar thermal energy. For the SOFC system (also considering the auxiliaries which provides power to the fuel cell) the energy efficiency is 51.72%, while for SOEC system it is 12.96%.
Therefore, the round-trip energy efficiency of the plant is 20.15%. Moreover, they have observed that the energy efficiency of the SOFC system decreases when the current density increases, due to the increase of irreversible losses. Then, increasing the utilization factor, the SOFC system efficiency increases while the round-trip efficiency of all the system decreases. In fact, as the utilization factor increases, for the electrolyser increases the power required, causing a decrease in the overall efficiency.

G. Butera et al.[45] have modelled a reversible solid oxide cells system, able to store large amount of excess of electricity in the form of natural gas (which can be injected in the grid thanks to its

composition equal to 97%$_v$ of methane) and then able to produce electricity using the natural gas from the grid, when there is electricity demand.

This system has shown to be technically feasible, thanks to the high round-trip efficiency equal to 80%, considering only DC powers (without the efficiency of conversion of inverter).

Ro. Peters et al.[46] have analysed and tested experimentally a r-SOCs system working with hydrogen. In fuel cell mode, they have obtained a maximum system energy efficiency of 62.7%, while in electrolyser mode they have obtained a maximum system energy efficiency of 70%. Moreover, they have conducted a parametric analysis to show how the efficiency values varies as function of the fuel utilization and the recirculation fraction, for both SOFC and SOEC operation mode. In SOFC, keeping constant the current density and increasing the fuel utilization, the system efficiency initially has increased, up to reach a maximum value. Over this working condition, a decrease in its value has been noted. The same happen when the recirculation flow is varied. On the other hand, for the SOEC mode, the efficiency value increases with higher steam utilization and stack power.

1.4 Scope and method of the thesis

In literature, many studies have been presented on Power-To-Power systems, based on solid oxide technology. However, in many cases they are not hydrogen-based systems, but make use of carbonaceous fuels, like syngas or natural gas, and often the studies found on this topic are the result of simulation of analytical models[40 42 44 45].

Moreover, particular attention in literature is given to the thermal self-sustainability of the system, and in all the cases analysed this is done through the installation of a thermal energy storage (TES) [42 43], which recovers the heat produced in SOFC mode to exploit it in SOEC mode.

In this thesis, the aim is the experimental study of a hydrogen-based reversible solid oxide stack, to test its performance in both fuel cell and electrolyser mode.
The objective is to define its performance in reversible operation, though the calculation of the stack round-trip efficiency, to investigate the operation of the stack in the framework of a Power-To-Power system, as distributed energy storage.

To do this, a stack characterization will be performed, and the stack efficiency will be calculated in both the SOFC and SOEC operation modes.

In the test campaign, two different working conditions will be considered: variable and constant fuel (or steam, in SOEC mode) utilization factor. The tests will be performed respectively in control voltage and in control current, for different stack temperatures, defined as the set point inlet streams temperatures.

Then, the stack efficiency values, for both the SOFC and SOEC mode, will be used to obtain the stack round-trip efficiency. To obtained it, a high current working zone for both the SOFC and SOEC will be considered, in which the performances of the stack are optimal, and the auxiliaries' consumptions can be assumed constant. The stack round-trip efficiency will be calculated for that region. The relative uncertainty associated to the stack round-trip efficiency will be calculated too.

Moreover, after having performed the stack characterization in SOFC and SOEC mode, a test campaign for the system characterization will be proposed.
However, the experimental analysis on the reversible system will not be carried out for the scope of this thesis, because of some technical problems to the test bench which was to be tested. Nevertheless, the system analysis will be proposed in the perspective of futures studies on the system, and it aims at investigating its performances and the thermal self-sustainability working point in both operation modes. Differently from the majority of the works found in literature, no TES integration will be considered.

This experimental work is part of the ComESto project framework, which stays for Community Energy Storage. It is a project financed in the context of PON (Programma Operativo Nazionale) ''Ricerca e Innovazione'' 2015-2020 and promoted by Miur, which aims to the development of a distributed storage system for the renewable energy, in the framework of an energy community. The main principles on which the project is based are self-production, self-consumption, storage and energy sharing. These are the same principles of a smart grid system, in which the energy is

produced and consumed as much as possible in the energy community, maximizing the self-consumption thanks to smartness of the grid and to digital systems.

Another point under investigation in ComESto project is understanding which could be the potentialities and which the limits of a system like this, even analysing the impact that the system could have in less developed countries, where electric infrastructures are weak.

The storage technologies involved in the project are many, some more innovative than others. They include the classical batteries and supercapacitors, the unconventional storage technologies like Power-To-Power systems and the electric vehicles, which can be considered as a storage system, able to inject power into the grid or at home when needed (Vehicle-to-Grid, V2G and Vehicle-to-Home, V2H)[47].

The ComESto system is situated in Fondazione Bruno Kessler (FBK) facility, in Trento, where the experimental activity has been performed.
It is constituted by a solid oxide stack, heat exchangers and auxiliary components. It represents an unconventional storage which could be located in the energy scenario described above. For this reason, the aim is to test its performance and realize a map of the working area of the stack, to know in which conditions it can operate and with which efficiency values.

The tests will be performed on the stack SB-G8-21, realized by SolidPower. For the stack characterization, it will be mounted on the test bench TB-2500, present in FBK facility too. A design of experiment (DoE) will be prepared to define the tests organization for the definition of the stack performances, in both SOFC and SOEC operation modes.

For the system's characterization proposed, the ComESto test bench will be presented, and a DoE will be prepared even in this case, to define the tests organization for both the SOFC and SOEC system.

Therefore, the structure of this study can be summarized as follows.
In chapter 2, the description of the technical characteristics of the stack and of the test bench on which it is tested will be presented.

The design of experiment (DoE) prepared for the stack characterization in both SOFC and SOEC mode will be presented too. The DoE consists in the preparations of some tables which define the set-up of the tests to carry out.
Finally, the ComESto system and the proposed DoE for the system in SOFC and SOEC will be reported.

In chapter 3, the results obtained from the stack characterization carried out in FBK facility will be shown and elaborated, using Python. The *V-I* curves will be plotted, and the stack efficiencies will be calculated, in order to obtain a detailed mapping of the various working region of the stack.
From the results of the stack characterization, in particular from the stack efficiencies in SOFC and SOEC, the stack round-trip efficiency will be finally calculated.

Finally, in chapter 4 the conclusions of the study will be presented.

2.Materials and Method

2.1 Stack characterization

The stack characterization has been performed in both SOFC and SOEC mode, with the aim to map the performances of the stack in reversible operation. In the next sections, the technical characteristics of the stack and of the test bench used for the experimental analysis will be presented, together with the design of experiment tables, which summarized the test campaign carried out in both SOFC and SOEC mode.

2.1.1 Stack specifications

The stack tested is composed by 70 solid oxide cells and it has been realized by SolidPower.
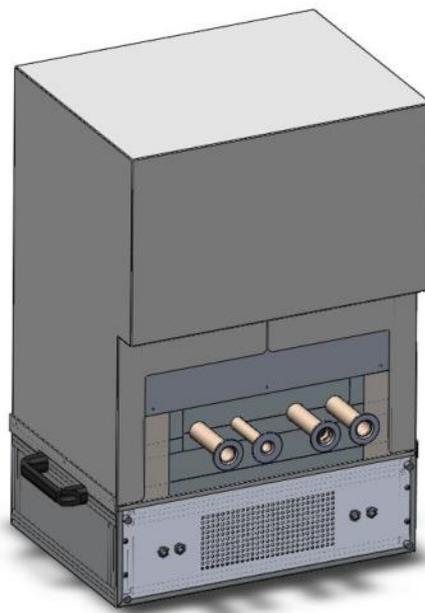
Figure 1: 3D representation of the stack used for the tests at FBK facility, realized by SolidPower.

The main parameters of the stack are shown in the table below.

Active surface area	80 cm^2
Number of cells	70 cells
Cluster for voltage probe	8 clusters (7 clustersx9 cell + 1clusterx7 cells)
Thermocouple sensor	9 thermocouples type K • 2x fuel/steam inlet line • 1x air inlet line • 1x fuel/steam outlet line • 1x air outlet pipe • 1x top stack side • 1x bottom stack side • 2x heater control

	No temperature sensors are present in the middle cells.
Inner electrical heater	2x Heater element Code VF508A12S Voltage supply: 220 V AC Max power: 2.2 kW

Table 1: Technical characteristics of the stack box present in FBK laboratory, realized by SolidPower.

The current limitation for the stack is equal to 70 A, to prevent overheating and failures, while the maximum voltage that can be set corresponds to 115 V, corresponding to an average voltage of 1.64 V for each cell.

Two inner electrical heaters are present in the stack, for an additional thermal control of the streams.

The stack materials are the followings: the anode is made with nichel oxide NiO, the cathode material is lantanium strontium manganite (LSM), while the electrolyte is made with yttria stabilized zirconia (YSZ).

2.2.2 Test bench characteristics

The testing activities of the stack have been performed on the test bench TB2500 present in FBK facility, supplied by SolidPower.

Figure 2: 3D representation of the test bench TB2500 present in FBK facility and used for the stack testing activity.

Originally, the test bench was designed to test the stack in SOFC operation. For this reason, it has been updated to work in SOEC mode. The main additional features included in the test bench are:

- Power unit up to 10 kW with wide span of current (0-140 A) and voltage (0-200 V).
- Inlet hydrogen line.

- Software modification to test electrolysis operation.

Moreover, it has been equipped with proper control software to modify any aspect necessary for the testing and characterization. A fully automated procedure can be easily implemented with a compiler embedded in the control, allowing to set sequential and repetitive testing procedures.

The range of operation of the main components of the test bench, with the correspondent uncertainties of the measurements is reported in the table below. It is important to know the technical limitations of the stack and of the test bench experimentally analysed, in order to correctly prepare the experimental set-up in the DoE tables.

Parameter	Value/Span	Uncertainty	Unit
Water flow	0-2200	± 0.5 % F.S.	g/h
Steam production	0-2000	-	g/h
Steam Temperature	150-500	1.5	°C
Hydrogen flow	0-44	± 0.7%	Nl/min
Air flow	0-400	-	Nl/min
Anode temperature	0-800	1.5	°C
Cathode temperature	0-800	1.5	°C
Voltage (Electronic Load)	0-160	<0.1 %	V
Current (Electronic Load)	0-200	<0.2%	A
Voltage (Power Unit)	0-200	<0.1 %	V
Current (Power Unit)	0-140	<0.2%	A

Table 2: Range of operation of the main components and flows of the test bench TB2500.

It can be noticed that the maximum steam flow rate is limited by the maximum flow rate supported by the steamer.

The maximum temperatures reached by the electric heaters is 800 °C (air, hydrogen, steam and stack's heaters). However, on the air line, the maximum air temperature that can be reached at the inlet of the stack is 780 °C, thanks to the good thermal insulation of the pipe.
On the steam line, the maximum steam temperature that can be reached at the inlet of the stack is 745 °C, because of higher thermal losses.

The electronic load used in SOFC mode is produced by EA ELEKTRO-AUTOMATIK with producer code EA-EL 9160-200 and a peak power $P_{peak} = 4.8 \text{ kW}$, while the power supply used in SOEC mode has the producer code EA-PSI 9200 140, with a peak power $P_{peak} = 10 \text{ kW}$.

2.1.3 Design of Experiment (DoE)
The design of experiment (DoE) is a statistical approach which aims at evaluating the effects of some factors on the result of an experiment. The steps to build an efficient DoE can be summarized as follow.

Firstly, is necessary to determine all the factors which can influence the result of the experiment we are going to perform. To do this, is necessary to identify dependent and independent variables in the process to be investigated. The independent variables are those which can be decided to vary, and on the basis of this variation then the response of the experiment will be analysed, through the values assumed by the dependent variables, not controllable.

The next step consists in defining the values that each factor can assume, considering the range of applicability for each independent variable. In this step it is important to choose a proper number of values, in order to obtain a good understanding of the process but also to not have too many tests to perform, which would represent a time-consuming approach.

The aim of the stack characterization is to obtain a detailed mapping of the stack, identifying the best working regions in terms of performances. To do this at the beginning a limited number of tests is planned. Then, the number of tests can be increased if a deeper level of detail is required.

Finally, the way in which the tests must be performed has to be decided, through the construction of some tables. These tables define which variables, between the independent ones, must vary in a continuous way (ramp variation, little steps of variation are decided) and which ones must vary with already defined values.

At this point, the tests can be carried out following the designed procedure and, for each value of the factors, the ramp variation of the decided variable is performed, and the values assumed by the dependent variables are registered.

To elaborate the results, it is important to determine which is the most impacting factor on the results of the experiment and how the interaction between different factors influences the results. In literature there are some methods which allow to do this though the compilation of some tables and the application of well-defined rules.
Considering an energy system, the typical variables considered in these cases are temperature, pressure, current, voltage, flow rates, and thermal and electric powers.

In this thesis, the scope of the testing activity is to map the performance of the stack in reversible operation. To obtain this result, the tests in SOFC and SOEC mode have been carried out separately in the stack, in order to identify a working zone with high stack efficiency for the two configurations. Through these values, the round-trip efficiency of the stack is obtained. This latter defines the performance of the stack in the Power-To-Power configuration, when the reversible operation is required, as in the framework of a distributed storage system in a nano-grid.

In the next sections, the DoE for the stack tests in SOFC and SOEC mode is presented. It schematically represents the tests that have been performed in FBK facility on the stack.

2.1.4 DoE - SOFC mode
To characterize the stack, the current-voltage (*V-I*) curves have been obtained. To carry out the tests, it is possible to operate with a control voltage (CV) or a control current (CC) strategy.
The test campaign in SOFC has been performed at:

- Variable fuel utilization *FU*
- Constant fuel utilization *FU*

Initially the tests have been performed in control voltage, with variable fuel utilization, keeping fixed the inlet hydrogen flow rate. Then, the tests have been performed in control current, keeping constant the fuel utilization, varying both the inlet hydrogen flow rate and the current.

Variable fuel utilization

At the beginning a series of tests in CV have been carried out, with variable fuel utilization (*FU*).

In CV operation, the stack voltage has been varied in continuous (defining a ramp variation) from a maximum value equal to 89 V, until to a minimum one V_{min}.

The minimum voltage for the stack represents a security value to not exceed, to avoid the oxidation of the catalyst materials of the cells. In the case of nickel, this value is equal to 0.7 V for each cell, but it varies with the temperature. So, considering that in the stack there are 70 cells and assuming the minimum value of 0.7 V/cell, the minimum stack voltage corresponds to 49 V.
However, to maintain a security level, the minimum stack voltage has been fixed to 54.4 V and so the voltage ramps have been performed considering a range between 89 and 54.4 V. The voltage ramps have been made with a ramp variation equal to 0.5 V/min, for both the ramp-up and ramp-down, to maintain a good thermal equilibrium in the stack.

The current variation has been observed in time.

Being the tests performed at variable fuel utilization, the input hydrogen mass flow rate has been maintained constant to the value of 19.8 Nl/min. This flow rate is associated to the maximum current value $I_{max} = 32\ A$ for the SOFC, and it has been calculated as indicated in the equation 26, assuming a maximum fuel utilization *FU*=80%.

$$\dot{n}_{H_2} = \frac{I}{z \cdot F \cdot FU} \cdot n_c$$	(26)

In the equation above, I is the current equal to 32 A, z is the oxidation number (*z*=2 for the hydrogen), *F* is the Faraday constant equal to 96485 $\frac{C}{mol}$ and n_c is the cell number, equal to 70. $\dot{n}_{H_2}$ is expressed in $\frac{mol}{s}$.

Multiplying for 22.414 $\frac{Nl}{mol}$ the hydrogen flow rate results equal to 19.8 Nl/min.

The maximum current is calculated considering the maximum current density equal to 0.4 $\frac{A}{cm^2}$ and considering that the stack has a total surface equal to 80 cm^2. The maximum value for the current density is associated to the minimum voltage value previously cited, to avoid the catalyst oxidation in SOFC mode.

The air inlet flow rate has been maintained fixed to 250 Nl/min, corresponding to an excess of air $\lambda = 5$, defined as the ratio between the real and stoichiometric flow rates ($\frac{air\ real}{air\ stoichiometric}$). The stoichiometric amount of air can be calculated considering that are necessary 2.5 $\frac{l_{air}}{lH_2}$.

Five stack temperatures have been analysed: 650, 660, 670, 680 and 690 °C. The stack temperature has been imposed fixing the heater's temperatures of the inlet streams (air and hydrogen) and of the stack. The temperature has been varied after the end of each single voltage ramp and some

minutes have been waited between one ramp and the other, for the thermal stabilization of the inlet and outlet streams.

Performing these tests, the fuel utilization has varied because the ratio between the current and the fuel flow rate has varied. Therefore, different efficiencies for different fuel utilization values will be obtained.

In the table below is summarized the organization of the tests in control voltage. In blue is indicated the variable obtained as result from the tests.

Hydrogen Inlet mass flow rate in the stack $\dot{Q}_{in,H2}$ [Nl/min]	Air mass flow rate $\dot{Q}_{air}$ [Nl/min]	Stack Temperature [˚C]	Stack voltage [V]	Stack current [A/cm²]	Fuel utilization [%]
19.8	250	650	Voltage ramp between 89 V and 54.4 V	0-0.4	0-90
		660			
		670			
		680			
		690			

Table 3: Table for the design of the tests for the stack characterization in SOFC operation mode.

From these tests, the *V-I* curves will be derived and derived quantities as the stack efficiency will be calculated in the results section, in chapter 3.

<u>Constant fuel utilization</u>

To keep constant the fuel utilization, the tests have been performed with a control current strategy.

In this case two load conditions have been defined: the full load and the partial load, corresponding to the 20% of the full load.
The full load condition corresponds to the hydrogen flow rate equal to 19.8 Nl/min, associated to the maximum current in SOFC operation ($I_{max} = 32\ A$), considering *FU*=80%. Therefore, the partial load, for the same *FU* value, corresponds to a current of 6.4 A.

Three different stack temperatures have been analysed (650, 670 and 690 °C) and, for each temperature, two different fuel utilizations have been tested (*FU*=40% and *FU*=80%), with the scope to map the stack's performances.
For each temperature, the tests have been performed defining a ramp variation for the inlet hydrogen flow rate, from 3.96 Nl/min (which is the partial load condition, corresponding to 20% of the full load, equal to 19.8 Nl/min) up to 19.8 Nl/min.

The current has been increased automatically with a script, in order to maintain the fuel utilization constant.
In the ramp-up of the hydrogen flow rate, the *FU* has been fixed to 40%. Reached the maximum limit for the flow rate (19.8 Nl/min), the current has been increased up to 32 A, keeping fixed the amount of hydrogen, to reach a FU equal to 80%.

Then, the ramp-down of the hydrogen flow rate has been performed, while the current value has been automatically decreased, to maintain a constant FU=80%.

Being these tests performed with a control current strategy, a security exit condition has been imposed in the script which automatically controlled the current. The condition established the test interruption, in case the stack voltage went below the minimum value allowed to prevent the catalyst oxidation.

In the table below is summarized the organization of the tests at constant fuel utilization in SOFC mode.

Stack Temperature [°C]	Steam utilization [%]	Air inlet flow rate in the stack [Nl/min]	Stack current [A]	Hydrogen inlet mass flow rate in the stack [Nl/min]	Stack voltage [V]
650	40				
	80				
670	40	250	Ramp from 3.24 A to 32 A	Ramp from 3.96 to 19.8	54.4-70
	80				
690	40				
	80				

Table 4: Table of the tests for the stack characterization in SOEC operation mode, constant steam utilization.

2.1.5 DoE - SOEC mode

To characterize the stack performances in SOEC, the test campaign has been performed at:

- Variable Steam Utilization U_{steam}
- Constant Steam Utilization U_{steam}

Variable Steam Utilization

In this case, the tests have been performed with a control voltage strategy. The inlet steam flow rate has been fixed to its nominal value equal to 1672 g/h. The voltage has been varied with a ramp equal to 0.25 V/min, starting from the open circuit voltage (OCV), which was approximately 60 V, up to 98 V and the correspondent current value of the stack has been measured. The air mass flow rate and the hydrogen amount in the steam have been maintained fixed (their values are reported in the table below). Once that the maximum voltage was reached, it was decreased to 0 V. The voltage ramp-up and the ramp-down have been repeated for 8 different stack temperatures (680, 690, 700,710, 720, 730, 740, 750 °C). For each working point, the steam utilization U_{steam} has been calculated, from the Faraday law. In fact, varying the current but keeping fixed the inlet steam, the steam utilization has varied during the test.

In the table below is summarized the scheme of the test performed with variable steam utilization in electrolyser mode. The variables indicated in blue (current and steam utilization) are those obtained as result.

Steam Inlet mass flow rate in the stack $\dot{m}_{in,H_2O}$ [g/h]	Air flow rate [Nl/h]	Stack Temperature [°C]	Stack voltage [V]	Stack current [A/cm²]	Steam utilization [%]
1672	85.728	680	Ramp from OCV (60 V) to 98 V	0-0.8	0-90
		690			
		700			
		710			
		720			
		730			
		740			
		750			

Table 5: Table of the tests for the stack characterization in SOEC operation mode, variable steam utilization.

Constant Steam Utilization

In this case, the tests have been performed in control current. The desired value of steam utilization has been fixed (25%, 50%, 75% and 90%) and then the current and the inlet steam flow rate have been varied proportionally, to maintain their ratio constant. The stack voltage has been measured. This operation has been repeated for each value of steam utilization. The current has been varied with a ramp from 0 up to 64 A, while the steam has varied from 6.384 Nl/h up to 29.712 Nl/h.

In this case there is not a limit of maximum current, because there are not problems of oxidation caused by too low voltage values in the cells. The maximum limit of 64 A is imposed just because of the flow limit of the steamer, equal to 2000 g/h, and considering a maximum steam utilization equal to 90%.

As consequence of the steam flow rate variation, the hydrogen amount to inject with the steam has varied too, to maintain its concentration in the mixture constant (equal to 10% in volume).

For each value of steam utilization, the tests have been performed for four different stack temperatures (710, 720, 740 and 750 °C).

The inlet air mass flow rate in the stack has been maintained fixed to the value of 85.728 Nl/h.

In the table below is summarized the organization of the tests with constant steam utilization. In blue is indicated the variable measured.

Stack Temperature [˚C]	Steam utilization [%]	Air inlet flow rate in the stack [Nl/h]	Stack current [A]	Steam inlet mass flow rate in the stack [Nl/h]	Hydrogen in the steam [Nl/h]	Stack voltage [V]
710	25					
720	50	85.728	Ramp from 0 to 64 A	From 6.384 to 29.712	From 0.638 to 2.971	OCV (approximately 60 V) to 105 V
740	75					
750	90					

Table 6: Table of the tests for the stack characterization in SOEC operation mode, constant steam utilization.

2.2 System characterization

In the following sections, the ComESto system will be described, in both the SOFC and SOEC working modes, though the process flow diagrams (PFDs).

The system is composed by the stack previously described and by the auxiliary components, which include a series of heat exchangers, the blower and the electric heaters for the stack and for the inlet streams in the stack. The tanks in which the hydrogen is stored in SOFC mode are not included in the system control volume.

A DoE for the system characterization in both SOFC and SOEC mode will be proposed but it will not be experimentally performed because out of the scope of this thesis. However, the tests are proposed for future studies on the ComESto test bench, to characterize it from the electric and thermal point of view.

2.2.1 System description- SOFC mode

In the fuel cell operation mode, observing the Process Flow Diagram (PFD) of the system in figure 3, it can be noticed that the input streams in the system are hydrogen (red arrow) and air (blue arrow), while the output streams from the system are the exhausted air and an exhausted stream composed by residual steam and excess of hydrogen not reacted (red arrow which exits from the stack).
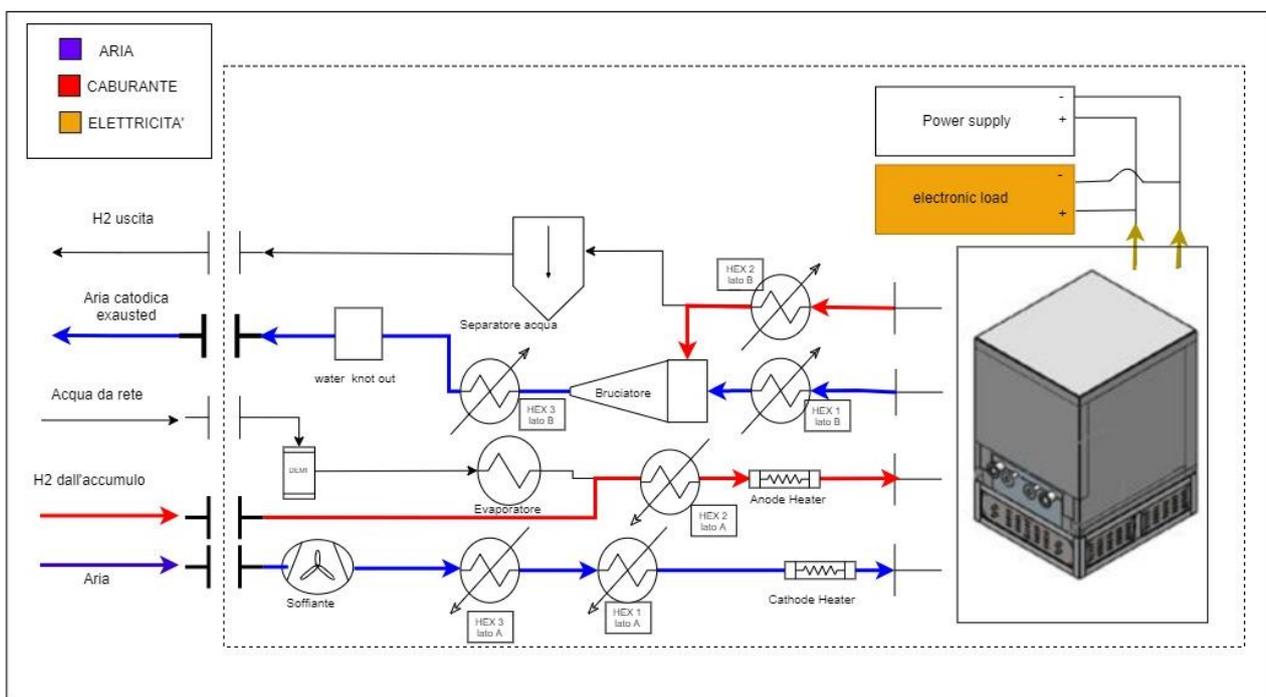
Figure 3: PFD of the system in fuel cell mode.

Focusing on the hydrogen inlet flow, it comes from two hydrogen tanks located outside the laboratory. The hydrogen in the tanks is stored at a pressure $p = 200$ bar and at ambient temperature, while the hydrogen stream which enters in the system must have a minimum absolute pressure equal to 8 bar. When it enters it is preheated by a heat-exchanger (HEX2), which recovers heat from the exhausted stream of steam and hydrogen previously cited.

The hydrogen tanks respect the standard N5, which defines purity characteristics of the hydrogen used, corresponding to 99.999%.

Then, the hydrogen is further heated-up by the anode heater present on the line. The heaters are electric resistances. Finally, it enters in the anode of the stack.

The inlet air is injected in the system by means of a blower. The blower works in 3 phases at 220 V and its angular speed is modulated regulating its frequency through an inverter. This is a closed loop control system, which ensures the flow rate control of the air stream.
Air then is preheated by two heat-exchangers (HEX3 and HEX1), which exploit the heat exchange with the exhausted air from the stack. Moreover, a cathode heater is present.

As mentioned above, the heat from the outlet streams is recovered for the inlet ones. In particular, for the exhausted steam and hydrogen flow, there is one recovery heat-exchanger (HEX2), while for the exhausted air flow, two recovery heat-exchangers (HEX1 and HEX3) are present. HEX3 represents an additional heat recovery, due to the combustion of the excess of hydrogen not reacted in a burner. This amount of heat is variable, depending on the amount of hydrogen given in input to the system, and it is an important parameter for the thermal self-sustainability that is wanted to be achieved, as will be explained in the DoE section 2.2.4.

Finally, the exhausted air which exits from HEX3 provides the cogeneration thermal power which is wanted to be calculated using the equation 27 below. The temperature of 50 °C is assumed as reference one for a building application, for which the cogeneration power is supposed to be used. Therefore, measuring the output air temperature from HEX3, the thermal power can be obtained.

$P_{th} = \dot{m}_{air} \cdot c_{p,air} \cdot (T_{air,out} - 50)$	(27)

Before to exit from the system, the air passes in the water chiller. It is a plates heat-exchanger, and its function is to cool- down the air, to avoid releasing it in the ambient at a too high temperature, and to allow the condensation of the humidity present in it. The water mass flow rate and the temperature of the inlet water in the chiller are fixed. The water flow rate is fixed to the value of 10 l/min, while the water inlet temperature is equal to 8 °C.

The electrical power produced in fuel cell mode exits from the stack and it is discharged in an electronic load. The electronic load is produced by EA ELEKTRO-AUTOMATIK, with producer code EA-EL 9084-340B. It can work in a voltage range 0÷80 V and in a current range 0÷340 A, considering a peak power $P_{peak} = 4.8$ kW.

The burner previously cited is a catalytic reactor, in which hydrogen/residual steam mixture and air enter. The burner has been built to work with a hydrogen volumetric flow equal to 20÷25 slpm (standard liter per minute) mixed with a steam volumetric flow equal to 20÷25 slpm, both at an input temperature of $T = 800$ °C. The design air volumetric flow is equal to 400 slpm, at an input temperature $T = 650$ °C. However, in the present study the input flow rate of hydrogen in the burner will not be fixed, but it will vary with the input hydrogen flow provided to the system. Moreover, it is important to notice that the amount of excess of hydrogen determine the heat

recovery from the burner and so it represent an important variable to investigate the self-sustainability of the system.

Finally, because of the high temperatures in the burner, the ignition is spontaneous and ignition system is not necessary, due to the presence of a catalytic burner able to burn quite low concentration of H_2 in the air flow.

In the photos below, some details of the ComESto test bench are shown. In particular, in figure 4 the boxes which contains the heat exchangers of the system are shown.

In figure 5, is shown the box which contains the electric heaters, to heat-up the inlet fluids in the stack.

Figure 4: Photo of the boxes in which are contained the heat exchangers of the ComESto system, which transfer heat from the outlet streams from the stack to the inlet ones.

Figure 5: Photo of the box which contains the air electrical heaters to heat-up the inlet air in the stack.

In both the figures 4 and 5, it is possible to see the vermiculite, a good thermal insulator, to guarantee the thermal insulation of the hot streams which have to enter in the stack. Moreover, it has been chosen even for safety reasons: it lets pass possible hydrogen leakages, without blocking them in the system.

In figure 6 and 7, it is possible to see the ComESto system as a whole.
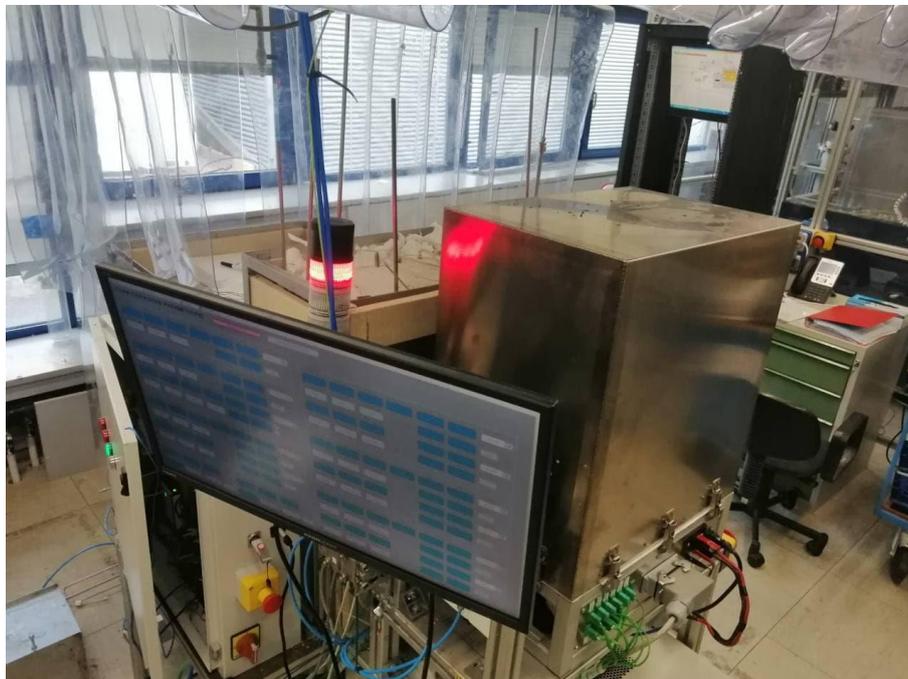
Figure 6: Picture of the ComESto test bench. In the picture it is possible to see also the monitor for the control system.

Figure 7:Picture of the ComESto test bench.

2.2.2 System description- SOEC mode

In the electrolyser operation mode, as input streams in the system there is the water flow and the air flow, while the outlet streams are the hydrogen produced and the exhausted air flow, as shown in in the PFD in figure 8. Air is inserted to clean the system, taking away the oxygen produced in the stack, and for thermoregulation function of the cells. So, in the exhausted air flow there is the air inserted plus the oxygen produced in the stack.
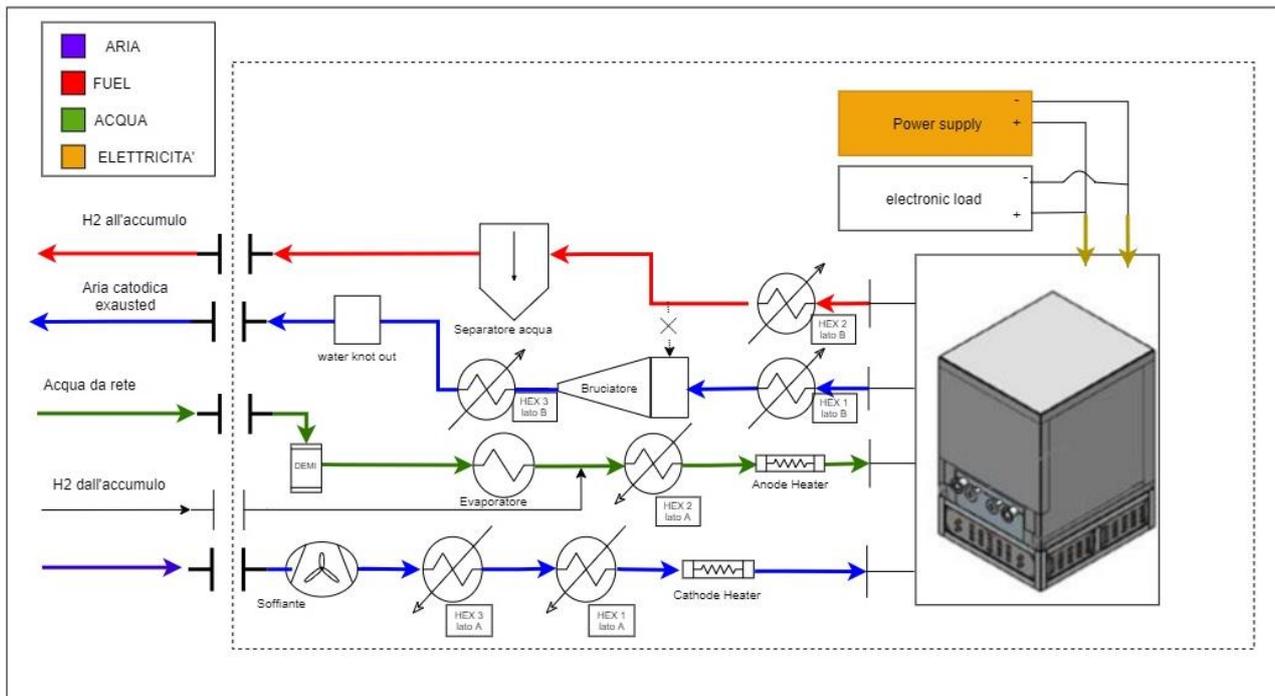
Figure 8: PFD of the system in electrolyser mode.

The water comes from the water network at a pressure between 3 and 5 bar, therefore a pump is not needed. Before to enter in the SOEC system, it is pre-treated using some resins to reduce the conductivity of water and so to eliminate the salts present in it, which would damage the steamer. The water purity reached is of quality II, < 2µS/cm^2.

In the steamer the water enters at ambient pressure, because of the presence of a valve which decreases the pressure level. The water enters in the evaporator to exit as steam and then to be mixed with hydrogen, usually with a ratio $\frac{H_2}{steam}$ of 10% in volume. The hydrogen is necessary because, in absence of reducing atmosphere, if small short-circuits are present at cell level, the nickel (the catalyst) tends to oxidate, with consequent expansion and stack's break up.

The steam is heated up in a heat-exchanger (HEX2), thanks to the heat transfer with the outlet hydrogen flow produced from the stack. Finally, it is additionally preheated in the anode heater on the line. Here it is important to specify that in the PFD the nomenclature is referred to the SOFC operation, for this reason the heater for the steam is indicated as anode heater even if the steam enters at the cathode of the SOEC.

The air enters in the system by means of the blower previously described and is preheated by the heat exchanger HEX3, through the heat transfer with exhausted cathodic air, and the heat-exchanger HEX1 present on the air line.
Additional heat is provided by the cathode heater before the entrance of the air in the cathode stack. So, the exhausted air passes in heat-exchanger HEX1 and HEX3 before to release the remaining heat to the water chiller, to be then expelled in the ambient.

Even in this case, the cogeneration power can be calculated considering the air outlet temperature from the heat-exchanger HEX 3 and considering a final use air temperature for domestic applications equal to 50 °C.

The hydrogen produced passes in the heat-exchanger HEX2, to transfer heat to the steam flow which enters in the stack. Then, as it contains some residual steam, it is sent in the water separator. The water separator is formed by two condensers. In the first step the steam present in the hydrogen produced is separated from the gas through simple condensation due to the contact of the steam/gas mixture with the cold metal of the condenser in which it flows. So, the water is separated, and it flows in the water drainpipe. Then, the gas separated flows in a second condenser which is taken cold by a chiller, called steam trap. Here, the gas goes up to be expelled because it is lighter than steam, while the residual steam goes to an accumulator, which will be automatically discharged when completely full.
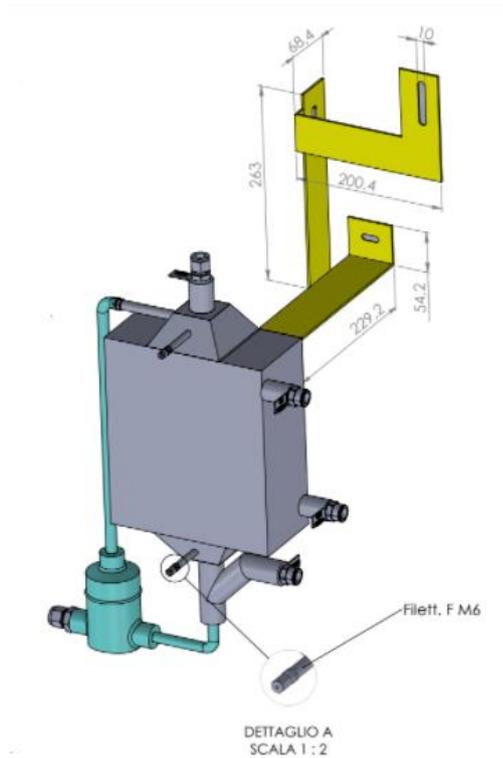
Figure 9: 3D representation of the water separator, realized by FBK.

The hydrogen produced and separated is expelled at ambient pressure outside by means of an extractor hood, in a point on the roof where there is no risk of combustion. The hood has a defined hydrogen flow rate, able to ensure a security state in the laboratory. In case of problems, the test bench has an alarm system which reports an excessive presence of hydrogen in the ambient.

The electric power is provided to the stack through a power supply EA-PSI 9200 140, with a voltage range 0÷160 V and a current range 0÷140 A, considering a peak power $P_{peak} = 10$ kW.

The system disposes also of an uninterruptible power supply (UPS), which provides power in case of a black-out occurs to allow to the electrolyser to continue to work.

2.2.3 Technical limits of the system

In the following tables are reported the technical limits of the main streams and components of the of the ComESto test bench.

These limits are reported because they must be taken into account for the DoE preparation. In fact, in the designing phase of the experiments, the range values established at which test the system must be coherent with the technical limit of the system analysed.

Hydrogen Flow $\dot{m}_{H_2}$		
Set Point	Min	0 [g/min]
	Max	6 [g/min]
Ramp	Min	0 [g/min/min]
	Max	2 [g/min/min]

Table 7: Set point and ramp limits for the hydrogen line.

Cathodic Air Flow $\dot{m}_{air}$		
Set Point	Min	0 [Nl/min]
	Max	400 [Nl/min]
Ramp	Min	0 [Nl/min/min]
	Max	400 [Nl/min/min]

Table 8: Set point and ramp limits for the cathodic air flow line.

Water Cathode Flow $\dot{m}_{steam}$		
Set Point	Min	0 [g/h]
	Max	2200 [g/h]
Ramp	Min	0 [g/h/min]
	Max	1000 [g/h/min]

Table 9: Set point and ramp limits for the cathodic water line.

However, the maximum water flow rate which can be supplied is 2000 g/h, limited by the evaporator (steam production limit).

Water Chiller $\dot{m}_{H_2O}$		
Set Point T	Min	0 [Nl/min]
	Max	400 [Nl/min]
Ramp T	Min	0 [Nl/min/min]
	Max	400 [Nl/min/min]

Table 10: Set point and ramp limits for the water chiller.

Heater Cathode T		
Set Point	Min	0 [˚C]
	Max	800 [˚C]
Ramp	Min	0 [˚C/min]
	Max	5 [˚C/min]

Table 11: Set point and ramp limits for the heater cathode.

Heater Anode T		
Set Point	Min	0 [˚C]
	Max	800 [˚C]
Ramp	Min	0 [˚C/min]
	Max	5 [˚C/min]

Table 12: Set point and ramp limits for the heater anode.

Inner Heaters stack T		
Set Point	Min	0 [˚C]
	Max	800 [˚C]
Ramp	Min	0 [˚C/min]
	Max	5 [˚C/min]

Table 13: Set point and ramp limits for the inner heaters.

Heater Steamer T		
Set Point	Min	150 [˚C]
	Max	500 [˚C]

Ramp	Min	0 [°C/min]
	Max	5 [°C/min]

Table 14: Set point and ramp limits for the heater steamer.

Concerning the pressures, the flows in the test bench work at ambient pressure, making exceptions for the hydrogen for which a minimum absolute pressure of 8 bar is required at the inlet of the system.

2.2.4 DoE - SOFC system

In this section, a DoE is proposed for the system characterization in fuel cell operation mode.

Firstly, a table to list all the dependent and independent variables involved in the system analysis has been made, in order to understand which variables could be interesting investigate.

The inlet air and hydrogen mass flow rates, and the inlet temperatures of these streams have been assumed as independent variables. On the other side, as dependent variables, the efficiency of the system, the cogeneration thermal power and the power consumption of the blower, expressed in W/m^2 have been considered. Moreover, it could be interesting even investigate the thermal power which can be recovered for the inlet streams from the heat exchanger disposed on the streams' lines (HEX1, HEX2, HEX3). Particular attention can be paid on the heat exchanger 3 (HEX3), which recovers the heat of the flue gas of the burner where the excess of hydrogen is burnt.

Independent variable	Dependent variable
Inlet Air Mass flow Rate ($\dot{m}_{in,air}$)	Air Outlet Temperature from burner ($T_{outlet,air}$)
Inlet Hydrogen Mass flow Rate ($\dot{m}_{in,H_2}$)	Thermal Power recovered in HEX3 ($P_{th,HEX3}$)
Air Inlet Temperature ($T_{in,air}$)	System Efficiency (η_{SOFC})
Hydrogen Inlet Temperature (T_{in,H_2})	Cogeneration Thermal Power (P_{th})
	Power Consumption of the Blower (P_{blower})

Table 15: Dependent and independent variables in SOFC operation

The performances of the system could be evaluated through the system energy efficiency. Moreover, the thermal behaviour of the system could be investigated, focusing on the conditions which allow to reach the thermal self-sustainability and finally on the calculation of the cogeneration power.

The aim is to reach the thermal self-sustainability point, in which there is no need to provide heat to the inlet fluids to reach the set point temperatures of the streams. This could be possible by burning the excess of hydrogen sent to the stack in the burner, to recover the heat and provide it internally in the system to heat-up the inlet streams in the stack, without an external energy expenditure. In fact, in normal operation condition the inlet streams are heated-up by the heat-exchangers and by the electric heaters. The aim is to eliminate the contribute of the electric heaters. To find this working point, different output power conditions must be tested in order to find the optimal amount of inlet hydrogen to send to the stack.

Then, for the cogeneration power, a building application could be considered, and so it could be calculated assuming a typical final use temperature of 50 °C.

An indicator used to evaluate the thermal self-sustainability could be the system efficiency: higher is its value, lower is the power to provide in input to the system and better is the thermal self-sustainability condition.

Therefore, two values for the hydrogen mass flow rate $\dot{m}_{H_2}$ can be proposed for the tests in then DoE, corresponding to the full load and the minimum load (33% of full load hydrogen mass flow rate). The full load condition can be calculated considering a maximum current of 32 A for the SOFC and a maximum fuel utilization of 80%.
Then, for each hydrogen mass flow rate, one air mass flow rates can be considered and three stack temperatures for each test.

The hydrogen inlet temperature can be fixed to the value of 690 ˚C. The mass flow rate of water in the chiller is not controllable and so it must be fixed to the value of 10 Nl/min, as for the water temperatures at inlet of the chiller, fixed to 8 °C.

The dependent variables which are wanted to be investigated are the temperature of outlet air from burner, the efficiency of the SOFC system and the thermal power recovered in cogeneration.
To investigate the thermal self-sustainability, the power required from the electrical heaters for the inlet streams must be analysed and the working condition (the inlet mass flow rate of hydrogen in the system) for which there is no need to provide this power must be checked.

The system efficiency and the cogeneration thermal power are derived quantities. The cogeneration power can be calculated knowing the air mass flow rate and the outlet air temperature from the heat exchanger number 3 (HEX3). The temperature difference of the air stream can be calculated considering a reference temperature of 50 ˚C, which is assumed to be the air utilization temperature in building energy applications.

| $P_{th} = \dot{m}_{air} \cdot c_{p,air} \cdot (T_{air,in} - 50)$ | (28) |

The system efficiency can be calculated in different ways. In this case, the control volume to consider is constituted by the stack and the heat exchangers, excluding the tanks in which the hydrogen is stored before to be used.
Two different formulations for the system efficiency can be considered and their results can be compared.
The first formula, reported in equation 29, takes into account the electric and the cogeneration output, while in input it considers the power content of the hydrogen and the power input P_{aux} given to the auxiliary components, including the electric heaters to heat-up the inlet streams:

| $\eta_{SOFC,system} = \dfrac{P_{el} + P_{th}}{P_{aux} + \dot{m}_{H_2} \cdot LHV_{H_2}}$ | (29) |

What is expect from this formula is that, increasing the input hydrogen, the amount of not reacted hydrogen will increase and so the amount of hydrogen which will burn in the burner. This will cause an increase of the heat recovery in HEX3 and will consent to decrease the thermal power provided

by the heaters, decreasing P_{aux}. The input hydrogen flow rate which allows to maximize the system efficiency has to be investigated.

Finally, the system efficiency can be calculated even considering the exergy of the streams, as reported in the formula below:

$$\eta_{SOFC,system} = \frac{P_{el} + P_{th}}{E_{ex,in} - E_{ex,out} + P_{aux}}$$	(30)

$E_{ex,in}$ and $E_{ex,out}$ are the total exergy for the input and output streams, respectively.

In the table 16 is summarized the design of the tests described for the system characterization. In blue are indicated the dependent variables to investigate.

SOFC – System characterization

Hydrogen Inlet mass flow rate in the stack $m_{\dot{H}_2,in}$ [g/min]-	Air Inlet mass flow rate in the stack $\dot{m}_{air,in}$ [Nl/min]	Inlet Air Temperature in the stack $T_{air,in}$ [˚C]	Inlet Hydrogen Temperature in the stack $T_{H_2,in}$ [˚C]	Water mass flow rate chiller $\dot{m}_{w,chiller}$ [Nl/min]	Air Outlet Temperature from burner $T_{air,burner}$ [˚C]	System Efficiency η_{SOFC}	Cogenreation Power P_{th} [kW]
Full load (100%) 1.855	250	600			TBD (To Be Defined)	TBD (To Be Defined)	TBD (To Be Defined)
		650					
		690					
			690	10			
Minimum load (33%) 0.612	250	600			TBD (To Be Defined)	TBD (To Be Defined)	TBD (To Be Defined)
		650					
		690					

Table 16: Table for the design of the tests for the system characterization in SOFC operation mode.

2.2.5 DoE - SOEC mode

In this section, a DoE is proposed for the system characterization in electrolysis operation mode. Even for the system in SOEC mode, some proposals of tests to characterize its performance and its thermal behaviour are presented. They could be useful for future analysis on the ComESto system but not for the aim of this thesis.

As in the previous case, a table with the list of the dependent and independent variables involved in the process has been prepared.

Independent variable	Dependent variable
Inlet Air Mass Flow Rate ($\dot{m}_{in,air}$)	Steam Utilization (U_{steam})
Inlet Steam Temperature ($T_{in,steam}$)	Stack Efficiency (η_{SOEC})
Inlet Air Temperature ($T_{in,air}$)	Outlet Hydrogen Temperature (T_{out,H_2})
Current (I)	Outlet Air Temperture ($T_{out,air}$)
% Hydrogen in the inlet steam (% $H_{2,in}$)	Hydrogen produced ($\dot{m}_{out,H_2}$)
Inlet Steam Mass Flow Rate in the stack ($\dot{m}_{in,steam}$)	Cogeneration Thermal Power (P_{th})
	Heater's Electrical Power ($P_{th,input}$)
	Power Consumption of the Blower (P_{blower})

Table 17: Dependent and independent variables in SOFC operation.

The independent variables taken into account are the air and steam inlet mass flow rates and temperatures, the current provided to the electrolyser and the percentage of hydrogen mixed with the input steam.

The dependent variables, considered for all the system, function of the independent ones, are the hydrogen produced, the cogeneration thermal power, the thermal power provided in input to the heaters, the efficiency of the system in SOEC operation, the thermal power recovered in the heat exchangers on the streamlines, the outlet temperatures of air and steam, the steam utilization and finally the power consumption of the blower, expressed in W/m².

In the system analysis, the system efficiency and the cogeneration thermal power in electrolysis mode could be evaluated. Moreover, even in this case the working point of thermal-self sustainability could be determined. To do this, the system can be analysed working at different voltages, in thermoneutrality and in exothermicity. In fact, in condition of thermoneutrality, the stack is neutral from the thermal point of view, and this means that heat is not produced neither absorbed. So, the inlet streams exit from the stack at the same temperature at which they have entered.

On the other hand, in exothermicity, the stack releases heat and so the inlet streams are heated-up at the outlet of the stack. In this analysis, interest must be focused on the cogeneration and the thermal power recovery for the thermal self-sustainability of the system. Therefore, an important parameter is represented by the efficiency of all the system and not only of the stack. For this reason, it is more interesting investigate the behaviour of the system at voltage values higher than the thermoneutrality voltage. In fact, a thermal self-sustainable system, means a system with higher efficiency, because the energy expenditure to provide in input in the form of thermal power (though the electric heaters) decreases.

The thermoneutrality voltage is calculated as follows[48]:

$$V_{th} = \frac{\Delta h_{reaction}}{z \cdot F}$$	(31)

where $\Delta h_{reaction}$ is the enthalpy variation of the steam electrolysis reaction, z is the oxidation number of the hydrogen ($z=2$) and F is the Faraday's constant equal to 96485 C/mol.

Therefore, for the characterization of the system the analysis can be carried out imposing the voltage value and applying a ramp variation to the inlet steam mass flow rate, from 0 g/h up to 1500 g/h, with step variations equal to 100 g/h/min. Then, the inlet air mass flow rate in the stack can be fixed on two different values, 100 Nl/min and 350 Nl/min. For the air inlet temperature in the stack, only one value could be assumed, equal to 750 °C, having as reference an optimal working temperature for electrolysers.

At the same way, the steam inlet temperature will be fixed to 400 °C for each voltage value tested.

The ratio $\frac{H_2}{inlet\ steam}$ between the flow rates is kept constant for all the tests and equal to 10% in volume.

For the chiller, the water mass flow rate and the water temperature must be fixed, to the same values reported for the SOFC mode.

The independent variables which can be investigated during the tests are the mass flow rate of hydrogen produced $\dot{m}_{out,H_2}$, the efficiency of the SOEC system η_{SOEC} and the cogeneration thermal power P_{th}.

The system efficiency, as said before for the SOFC system, can be calculated it in two different ways, considering the energy efficiency and the exergy efficiency.

$\eta_{SOEC,system} = \dfrac{\dot{m}_{H_2} \cdot LHV_{H_2} + P_{th}}{P_{aux} + P_{el}}$	(32)

$\eta_{SOEC,system} = \dfrac{E_{ex,out} - E_{ex,in} + P_{th}}{P_{el} + P_{aux}}$	(33)

Then, the product of the efficiencies in SOFC and SOEC mode provides the round-trip efficiency of the reversible system (r-SOC system efficiency).

The table 18 summarizes the design of the experiments which could be carried out on the system in SOEC mode. In blue are indicated the dependent variable to investigate.

SOEC – System characterization

Control voltage	Inlet Steam Mass Flow Rate in the stack $\dot{m}_{in,steam}$ [g/h]	Inlet Air Mass Flow Rate in the stack [Nl/min] $\dot{m}_{in,air}$	Inlet Air Temperature in the stack $T_{in,air}$ [°C]	Inlet Steam Temperature in the stack $T_{in,steam}$ [°C]	% Hydrogen in the inlet steam $H_{2,in}$	Inlet Water Mass Flow Rate in chiller $\dot{m}_{in,w}$ [l/min]	Hydrogen produced $\dot{m}_{out,H_2}$ [l/min]	Efficiency η_{SOEC} [-]	Cogeneration Thermal Power P_{th} [kW]
Vth	From 0 g/h to 1500 g/h with steps equal to 100 g/h/min	100	750	400	10%	10	TBD	TBD	TBD
		350							
V>V$_{th}$	From 0 g/h to 1500 g/h with steps equal to 100 g/h/min	100	750	750	10%	10	TBD	TBD	TBD
		350							

Table 18: Table for the design of the tests for the system characterization in SOEC operation mode.

3. Results and Discussion

In this chapter, the experimental results obtained from the stack characterization tests will be presented. For each operation mode, SOFC and SOE, the results for both variable and constant utilization factor will be reported and discussed.

To the presentation of the data collected will follow an elaboration section, in which the main electrical quantities useful to characterize the stack performances will be derived. As consequence, the stack efficiency, for both SOFC and SOEC in each working condition, will be obtained.

The data elaboration has been performed through Python.

Finally, thanks to the information on the performances in SOFC and SOE, the stack efficiency of the reversible system (r-SOC) will be computed, for the variable utilization factor working condition.

The relative uncertainty associated to this stack round-trip efficiency will be calculated.

3.1 SOFC mode – Variable Fuel Utilization

3.1.2 Presentation of results

In this section the results obtained from the tests performed at variable fuel utilization are shown.

The tests have been carried out with a control voltage strategy, for five different stack temperatures (650, 660, 670, 680, 690 °C). Therefore, the voltage has been varied with a ramp (ramp-up and ramp-down alternatively) in the range between the OCV value (89 V) and the minimum voltage allowed, in order to not damage the cells (54.4 V).

The input hydrogen flow rate has been kept constant, while the current has varied following the voltage variation. As consequence, the fuel utilization has varied with the time.

The trends of the voltage and current in time are shown in the figures below, together with the trend in time of the outlet air temperature from the stack (figures 4-8).

It can be noticed that the voltage and the current have an opposite increasing trend (when one increases the other decreases), typical of power generation system based on electrochemical reaction like battery. In fact, with the increasing of the current, the voltage values decrease with respect to the OCV voltage value, and the difference of voltage is associated to the mass transport losses, due to internal irreversibility.

In SOFC operation mode, the behaviour of the stack is always exothermic. This can be observed looking at the trend of the outlet air temperature as function of the time, in figures 4-8. When the current increases, the outlet air temperature increases too, because the internal irreversibility increases. On the other hand, when the current decreases, the heat released from the stack decreases too, and so the outlet air temperature decreases with respect to the initial condition at t=0.

During the voltage ramps, after having reached the voltage set point, the voltage value set has been kept constant for a certain time in order to reach the thermal equilibrium in the stack. However, it can be noticed that the current value continues to change (increasing or decreasing). This happen

because at the beginning the thermal equilibrium is not reached yet, and so the stack temperature continues to vary, causing the variation of the cells' resistance and so the current variation.
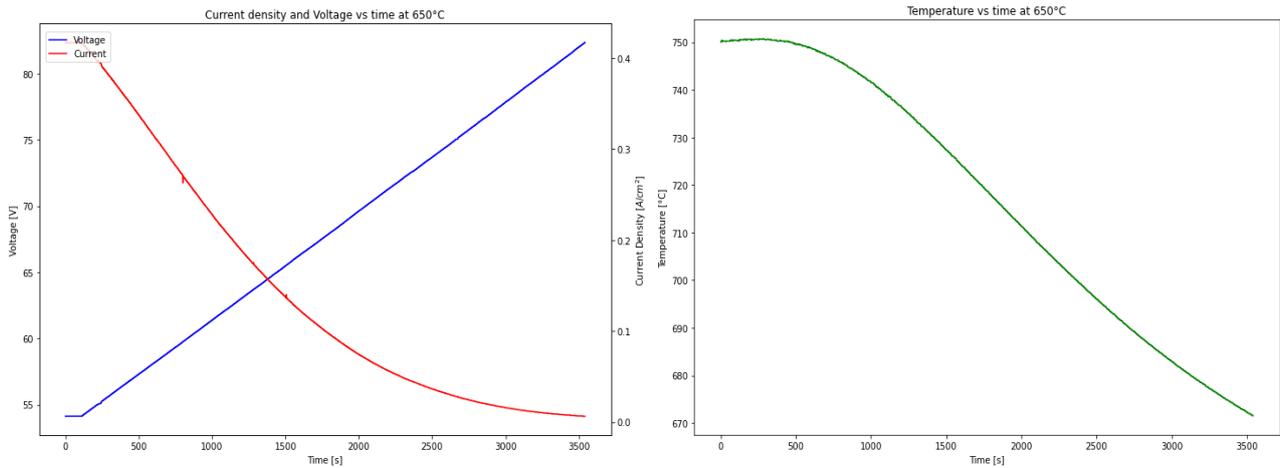

Figure 10: Trends of current and voltage as function of time (on the left) and trend of the outlet air temperature as function of time (on the right), for T_{stack}=650 °C.

In figure 11, the trend of the outlet air temperature as function of the time initially decreases even if the current always increases. Probably, in this case the temperature was not still stabilized. In fact, the previous test had been carried out at $T_{stack} = 670 \,°C$, and the current had a decreasing trend in that case (and so even the outlet air temperature).
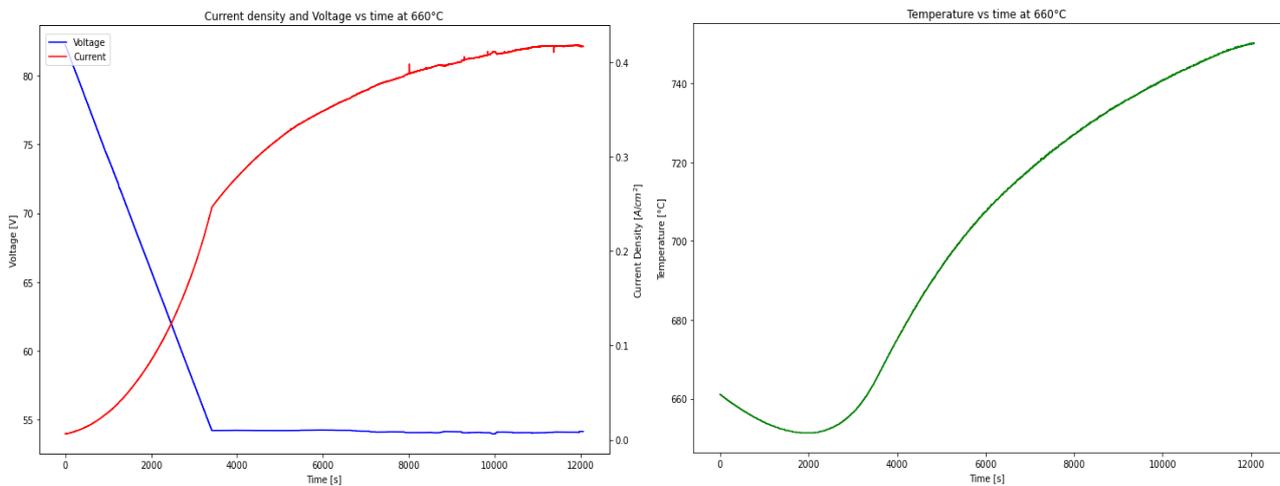

Figure 11: Trends of current and voltage as function of time (on the left) and trend of the outlet air temperature as function of time (on the right), for T_{stack}=660 °C.
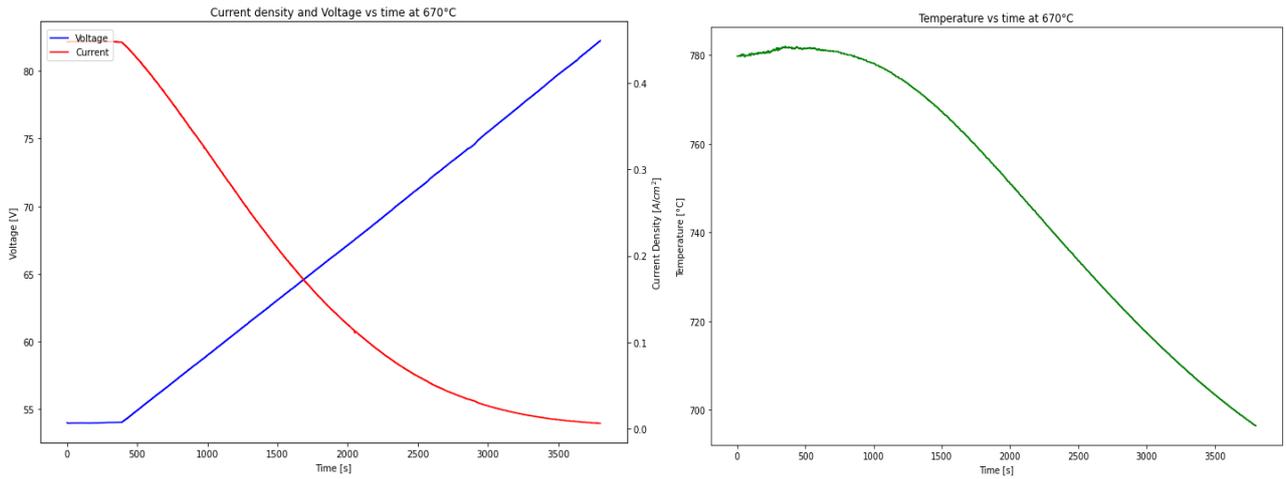
Figure 12: Trends of current and voltage as function of time (on the left) and trend of the outlet air temperature as function of time (on the right), for T_{stack}=670 °C.
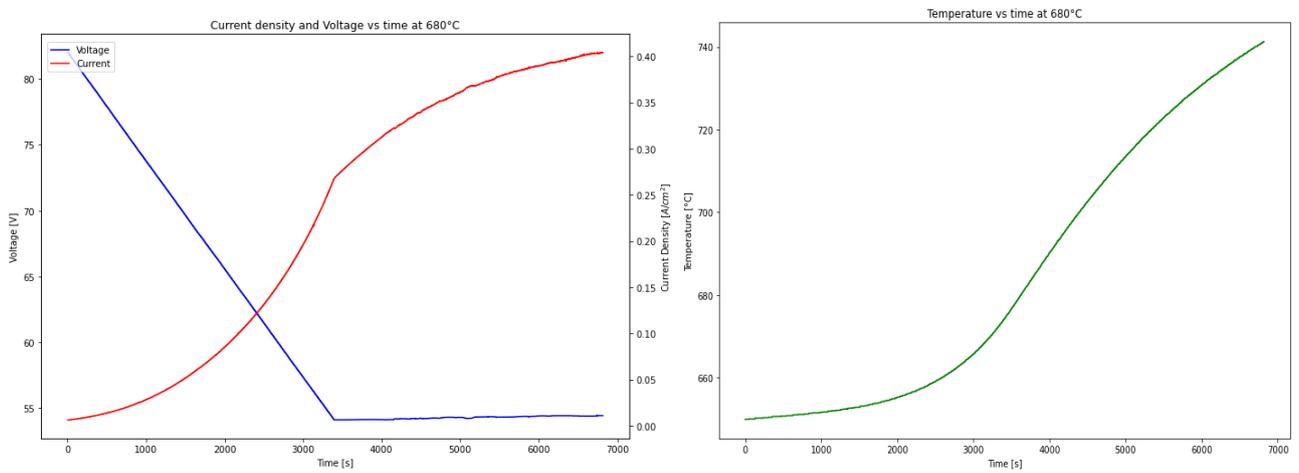

Figure 13: Trends of current and voltage as function of time (on the left) and trend of the outlet air temperature as function of time (on the right), for T_{stack}=680 °C.
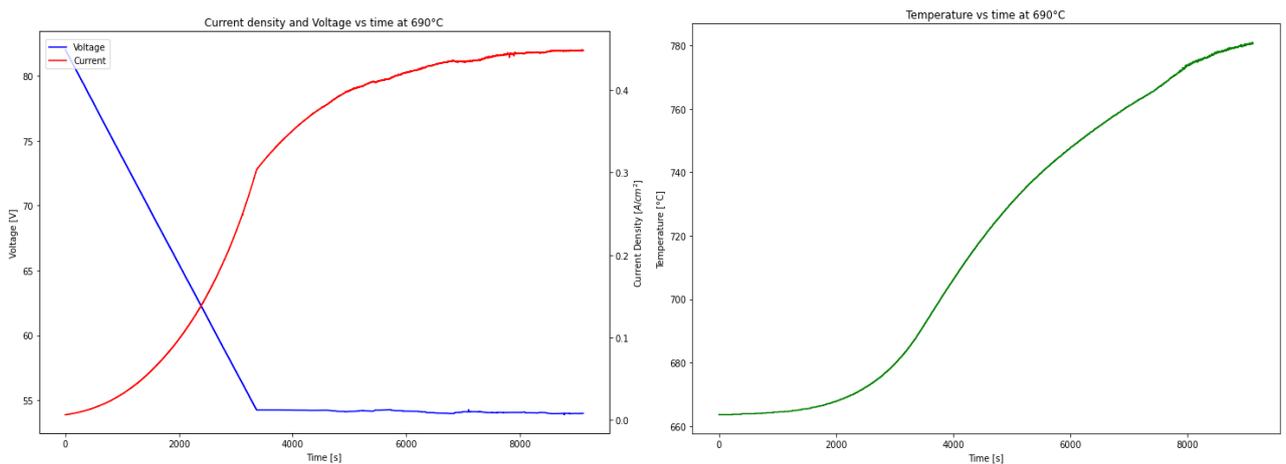

Figure 14: Trends of current and voltage as function of time (on the left) and trend of the outlet air temperature as function of time (on the right), for T_{stack}=690 °C.

3.1.2 Elaboration and Discussion

The data shown in the previous section have been elaborated to obtain the *V-I* curves for the stack.

As shown in figure 15, the stack voltage has been plotted as function of the current density, for the different stack temperatures analysed. The stack voltage taken into account is the sum of the voltages of the 8 single clusters of cells, in which 8 probes are present. This is done to have a more precise stack voltage, not affected by the cables' voltage losses.

Moreover, on the lateral colour bar is shown the outlet air temperature from the stack, indicated on the plot for each point of the curves.

As can be seen from the figure 15, higher current density values are associated to higher outlet air temperatures, considering the same voltage value. In fact, the ohmic voltage drop can be considered as the main overpotential loss in the case of solid oxide cell, and it is modelled through Area Specific Resistance (ASR) of the stack. The ASR decreases with the increase of temperature and as consequence the voltage losses decrease (it can be noticed with a decrease in the slope of the curves with the increase of temperature).

The outlet air temperature is considered in the analysis, because it is considered as the best approximation representative of the stack temperature, because of its highest flow rate in the stack. The air stream, therefore, represent the thermal vector in the analysis.
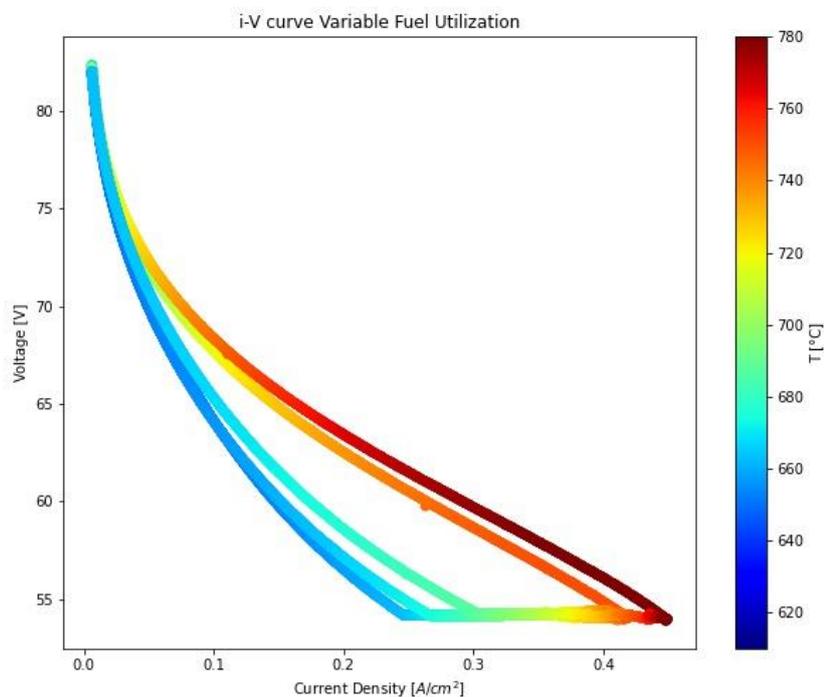

Figure 15: *V-I* curves for different stack temperatures, in SOFC mode with variable fuel utilization. On the colour bar is shown the outlet air temperature, indicated for each point of the curves.

After the elaboration of the *V-I* curves, the stack efficiencies have been calculated.

The stack efficiency in the electrochemical cells can be defined as the product between three different energy efficiency[15]:

$$\eta_{total} = \eta_{thermodinamic} \cdot \eta_{electric} \cdot \eta_{fuel} \tag{34}$$

- The thermodynamic efficiency $\eta_{thermodinamic}$ is defined as the ratio between the Gibb's free energy variation and the enthalpy variation of the reaction. The Gibb's free energy variation represent the work which can be obtained by the electrochemical reaction, while the enthalpy variation represents the total energy that the fuel would release if burned in an isobaric transformation. Therefore, the thermodynamic efficiency expresses the energy ratio comparing the use of the fuel in the electrochemical reaction with the use of the fuel in a combustion reaction.

$$\eta_{thermodinamic} = \frac{\Delta g_{reaction}}{\Delta h_{reaction}} \tag{35}$$

The Gibb's free energy variation of the reaction is presupposed to be lower than the enthalpy variation, assuming the $\Delta h_{reaction}$ as the maximum energy made available by the reaction. In fact, the specific enthalpy variation of the reaction can be expressed as the sum between the specific Gibb's free energy variation and the irreversibility associated to the reaction and to the transport phenomena in the stack, released in the form of heat (see equation 36). Increasing the stack current value, the irreversibility generated in the stack increases. Therefore, the term $T \cdot \Delta s_{reaction}$ increases and the work available by the electrochemical reaction $\Delta g_{reaction}$ decreases, causing a decrease in the thermodynamic efficiency.

$$\Delta h_{reaction} = \Delta g_{reaction} + T \cdot \Delta s_{reaction} \tag{36}$$

- The electric efficiency $\eta_{electric}$ is defined as the ratio between the operative voltage and the OCV voltage.

$$\eta_{electric} = \frac{V}{V_{OCV}} \tag{37}$$

The OCV voltage can be calculated through the Nernst formulation, reported in equation 38.

$$V_{OCV} = \frac{-\Delta g(T, P_i)}{z \cdot F} = \frac{-\Delta g(T, P_0)}{z \cdot F} - \frac{R \cdot T}{z \cdot F} \cdot ln \frac{\prod_i^P P_i/P_0}{\prod_i^R P_i/P_0} \tag{38}$$

It represents the maximum stack voltage, in the equilibrium condition, when no current flow is present and no irreversibility due to transport phenomena are generated in the stack. For this reason, it is called open circuit voltage. In equation 38, T is the temperature at which the reaction occurs (approximated with the stack temperature), while P_i and P_0 are respectively the partial pressure of the streams in the stack and a reference pressure, usually 1 bar. It can be noticed that

the OCV voltage is influenced by the operative conditions in the stack. In particular, it decreases when the stack temperature increases and/or when the partial pressure of reactants decreases.

Therefore, the electric efficiency takes into account the irreversibility associated to the mass transport phenomena in the stack, when the external circuit is closed and the current starts to flow. Even in this case, the electrical efficiency decreases with the increase of current.

- The fuel efficiency η_{fuel}, also known as fuel utilization *FU*, is the ratio between the reacted fuel and the total fuel given in input in the stack. It takes into account that not all the fuel inserted in the stack will react. For the stack, it is defined as follows:

| $$\eta_{fuel} = FU = \frac{I \cdot n_c}{z \cdot F \cdot \dot{n}_{fuel}}$$ | (39) |

In equation 39, n_c represents the number of cells in the stack, I is the stack current, z is the oxidation number of the fuel, F is the Faraday's constant equal to 96485 C/mol and $\dot{n}_{fuel}$ is the molar flow rate of fuel given in input to the stack.

In this study, the stack efficiency has been calculated firstly considering only the electric efficiency and then adding the fuel efficiency contribution, to observe the effect of the fuel utilization on the stack performances.

These efficiencies in the following analysis have been defined theoretical and empirical, respectively, to underline the influence of the fuel utilization factor.

Therefore, summarizing:

| $$\eta_{SOFC,theoretical} = \frac{V}{V_{OCV}}$$ | (40) |
| $$\eta_{SOFC,empirical} = \frac{V}{V_{OCV}} \cdot \eta_{fuel}$$ | (41) |

The thermodynamic efficiency has not been considered, and as maximum reference level the OCV has been assumed, to avoid difficulties in the Gibb's free energy estimation.

For the OCV voltage, the experimental value has been used in the formulations 40 and 41. It has been defined for each stack temperature analysed, observing the voltage value associated to the null current condition, prior the application of current. However, in the expression of the efficiencies, the OCV voltage has been considered constant for a certain stack temperature, even if the temperature in the stack increases with the increase of current. Moreover, it has been compared with an operative voltage value V sensible to the temperature variation in the stack. Therefore, an approximation has been done in the calculation.

In figure 16, the trends for the theoretical and empirical stack efficiency are shown, as function of the current density. On the colour bar is indicated the air outlet temperature from the stack.

The following considerations can be done:

- For the same current density value, higher stack efficiency values (both the theoretical and the empirical) can be obtained when the outlet air temperature is higher, because at parity of current density the voltage values are higher, due to lower ASR.
- For the empirical efficiency, at parity of efficiency, lower current density values when the temperature increases.
- The fuel efficiency is lower for lower current density, while it increases when current increases. Therefore, this explains the higher empirical efficiency values for higher current density, being in that region the fuel utilization higher than in the low current density region.
- Maximum value of empirical stack efficiency stays around 55%, for high current density working zone and high outlet air temperatures.
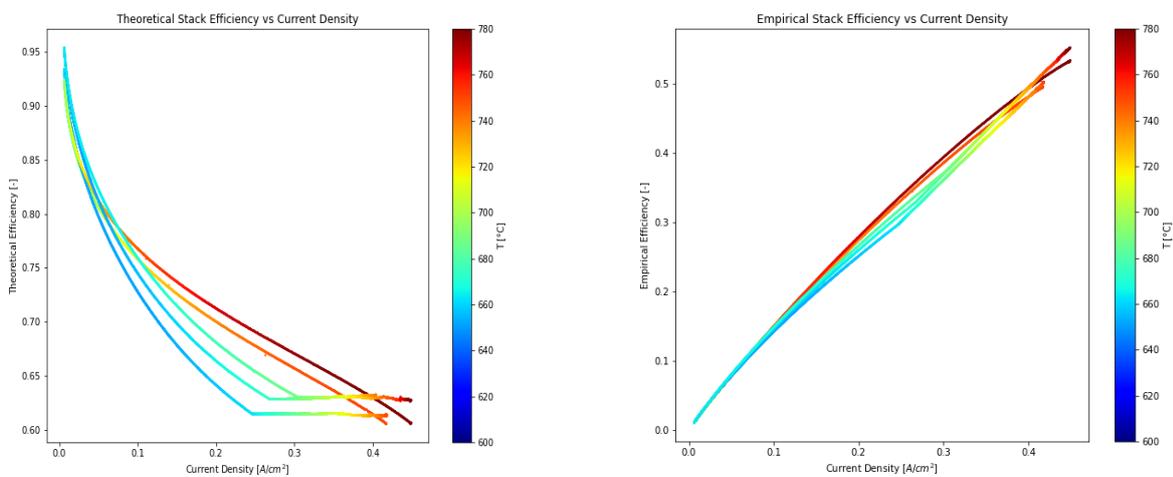

Figure 16: Theoretical Stack efficiency (on the left) and empirical stack efficiency (on the right) as function of the current density, for different T_{stack}, with variable fuel utilization. In the colour bar is represented the outlet air temperature from the stack, indicated for each point of the curves.

Finally, the area specific resistance (ASR) for the stack has been calculated and it has been plotted as function of the stack efficiencies previously calculated.

The ASR has been calculated with the equation 42, for each stack temperature tested.

$$ASR = \frac{V_{OCV} - V}{i}$$	(42)

The main assumption related to the ASR can be summarized below:

- The ASR represents the overall stack resistance, but it is modelled as if the stack was a simple electric circuit, considering the Ohm's law.
- The ASR is not a real electric resistance, but it is approximated as it was, as it takes into account the resistance in the transport phenomena of the electrons and ions in the external circuit and in the electrolyte, respectively.

- It models only the overpotential losses present in the middle part of the *V-I* curves, which have a linear trend as function of the current. However, for the solid oxide cells they are a good approximation to take into account the global overpotential losses.

In equation 42, the stack voltage V has been calculated considering the voltage value of the last cluster of the stack. In fact, in this part of the stack the temperature should be closer to the outlet air temperature, which influence the behaviour of the ASR.

It is to mention that in the ASR calculation only current values higher than 1 A have been taken into account, to avoid the influence of activation overpotential phenomena for example, typical of low current values, which cannot be described by an ohmic behaviour.

In the following figures, the ASR has been plotted as function of the theoretical and empirical stack efficiency previously described and calculated.
These plots have been made to show to a characteristic mapping of the stack, independent from the current flow.
In figure 17, the trend of the ASR as function of the theoretical stack efficiency is shown, for three different stack temperatures (660, 680 and 690 °C). Both the relations with the outlet air temperature and with the fuel utilization are shown in the colour bar.

The tests performed at 650 °C and 670 °C have been excluded because the thermal equilibrium condition has not been respected during the tests, and so the results would not be precise.

From the figure 17 it is possible to notice that:

- The ASR increases with the increase of the stack theoretical efficiency (this latter, in fact, is higher for lower current values).
- To lower ASR values are associated higher temperatures.

Concerning the relation with the fuel utilization, it is possible to notice that:

- To higher fuel utilization values are associated lower ASR values. Higher fuel utilizations are in fact associated to higher currents and, therefore, to higher temperatures.
- To the increase of the theoretical efficiency is associated the decrease of the current and of the fuel utilization. Therefore, the increasing of the ASR value can be observed.
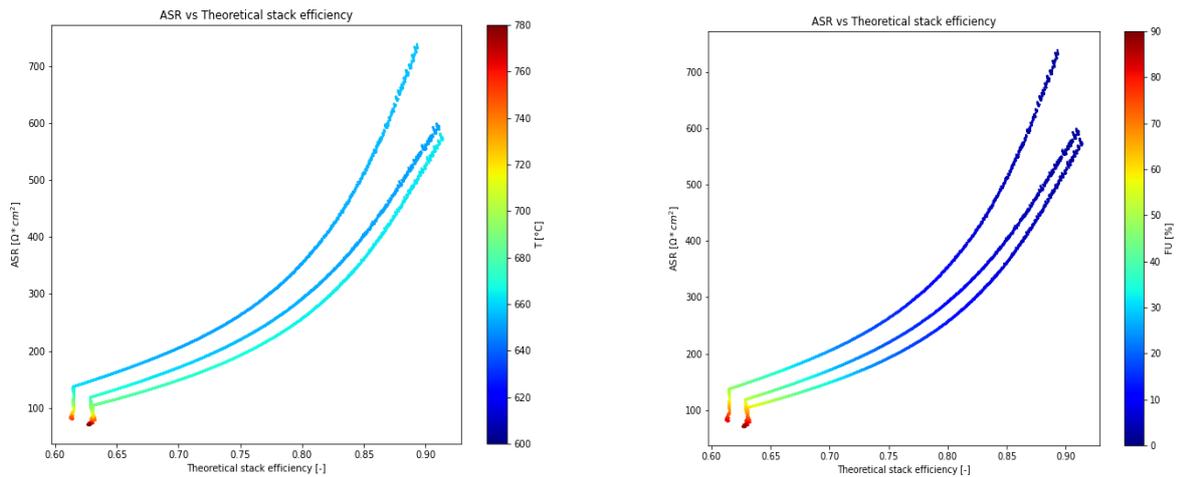
Figure 17: Trend of the ASR as function of the theoretical stack efficiency, for three different stack temperatures (660, 680 and 690 °C) in SOFC mode. In the colour bar is shown the outlet air temperature from the stack (on the left) and the fuel utilization (on the right) for each point of the curves.

In figure 18, though a 3D plot is summarized the relation between the ASR, the theoretical stack efficiency, the outlet air temperature from the stack and the fuel utilization, to have a complete mapping of the stack behaviour in SOFC mode.
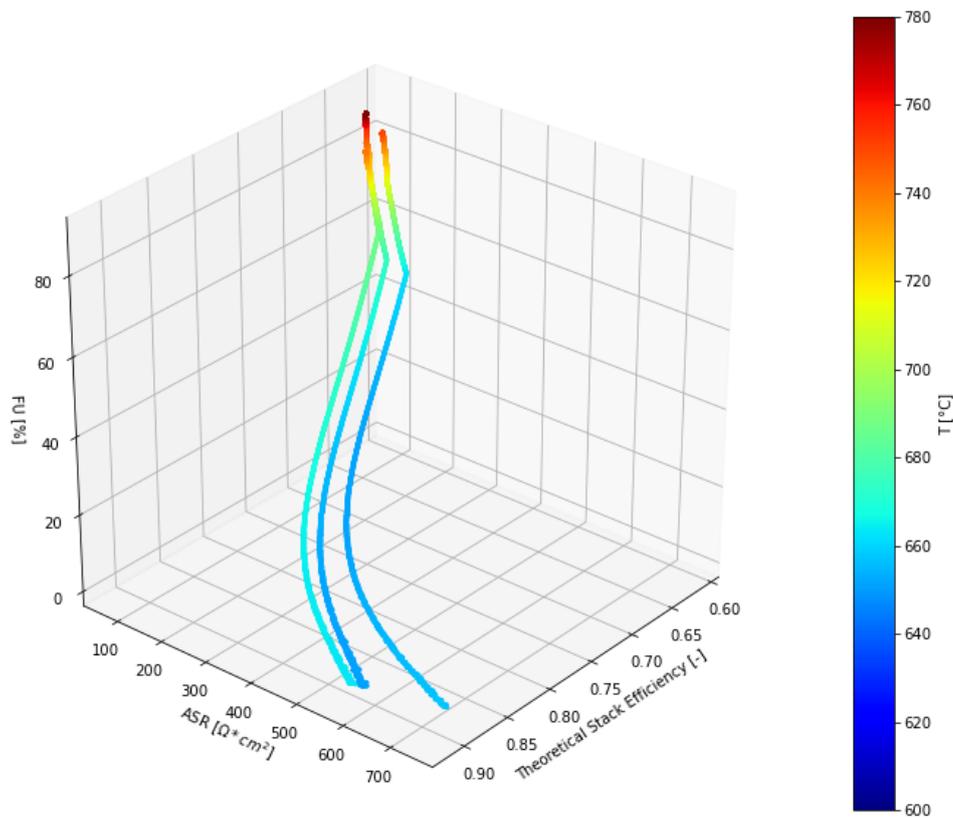

Figure 18: 3D plot of the ASR trend in SOFC mode as function of the theoretical stack efficiency and the fuel utilization. In the colour bar is indicated the outlet air temperature for each point of the curves.

Moreover, the trend of the ASR has been plotted even as function of the empirical efficiency, as shown in figure 19.

In this case, the ASR decreases with the increase of the empirical efficiency. In fact, higher currents are associated to higher values of empirical efficiency and, therefore, in this working region temperatures are higher. So, it is interesting to underline even in this case the relation of the ASR with the temperature.

These considerations can be summarized as follows:

- Higher empirical stack efficiency values are reached for lower values of ASR.
- The condition of lower ASR values is associated to higher outlet air temperatures.
- To the increase of the ASR is associated a decrease of the outlet air temperature and a decrease of the empirical efficiency.
- To higher currents are associated higher fuel utilizations (being the hydrogen flow rate fixed). Therefore, for higher fuel utilizations the ASR values are lower.
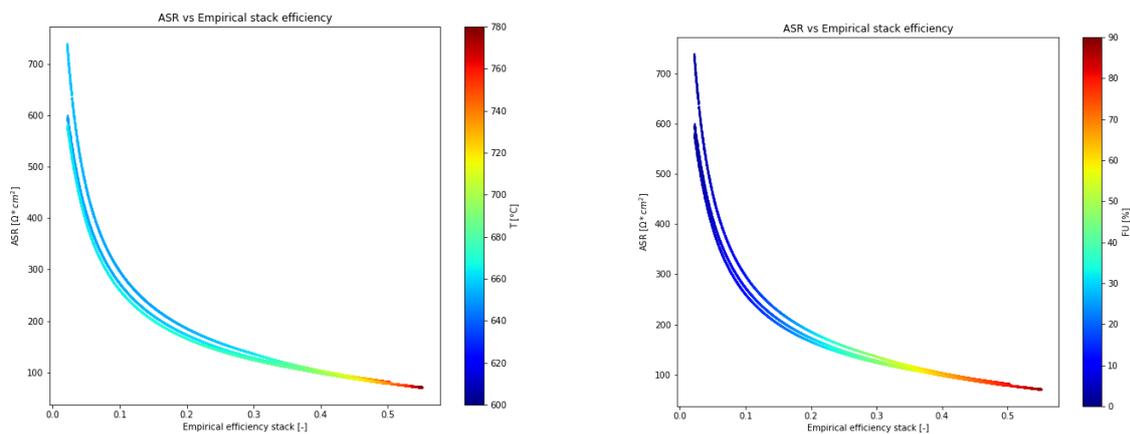

Figure 19: Trend of the ASR as function of the empirical stack efficiency, for three different stack temperatures (660, 680 and 690 °C) in SOFC mode. In the colour bar is shown the outlet air temperature from the stack (on the left) and the fuel utilization (on the right) for each point of the curves.

In figure 20, a 3D plot which summarized these relations is shown.
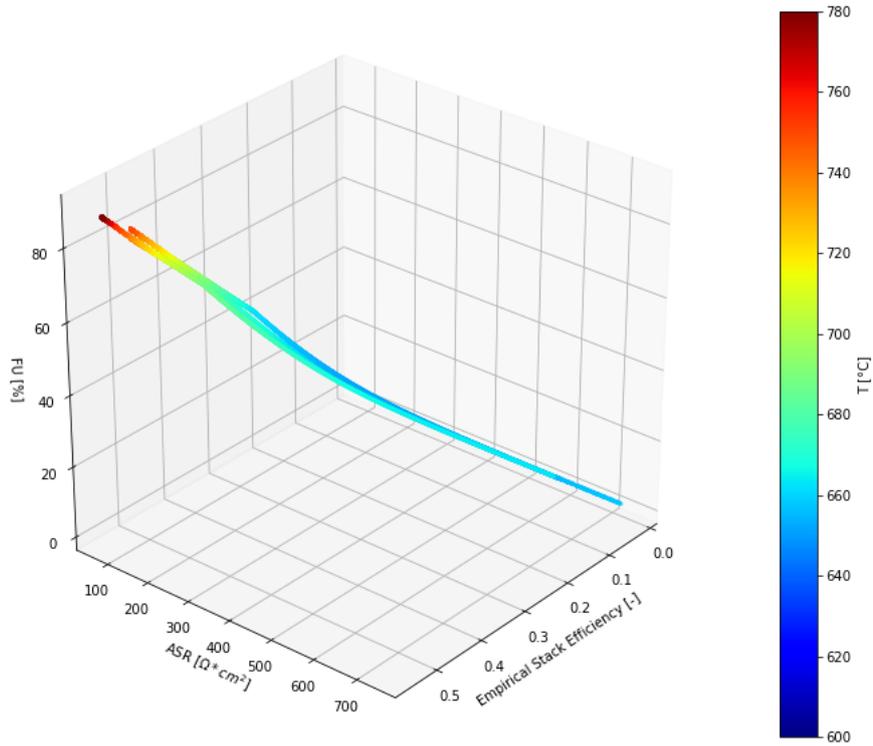
Figure 20: 3D plot of the ASR trend in SOFC mode as function of the empirical stack efficiency and the fuel utilization. In the colour bar is indicated the outlet air temperature for each point of the curves.

The behaviour of the ASR, as shown, is strongly related to the temperature. In fact, the ASR represents the overall cells resistance and with the increase of the temperature both the kinetic of the materials used in the stack and the kinetic of the reaction increase.

The relation between the ASR and the temperature can be modelled in first approximation with the Arrhenius-type profile, expressed in equation 43.

$$ASR(T) = ASR_0 \cdot e^{\frac{E_a}{R} \cdot (\frac{1}{T} - \frac{1}{T_0})} \tag{43}$$

In the equation 43, T_0 is a reference temperature, chosen arbitrarily, ASR_0 is the ASR value associated to the reference temperature, R is the universal gas constant equal to 8314 $\frac{J}{mol \cdot K}$, T is the actual stack temperature and E_a is the activation energy of the fuel cell reaction.

Plotting the natural logarithm of the ASR as function of the reciprocal of the stack temperature minus the reciprocal of the reference temperature (Arrhenius plot), a linear trend should be obtained (see figure 21). As reference temperature T_0, the value 800 °C has been chosen.

In equation 44, the Arrhenius model is indicated

$$\ln ASR = \ln ASR_0 - \frac{E_a}{R \cdot T} + \frac{E_a}{R \cdot T_0} \tag{44}$$
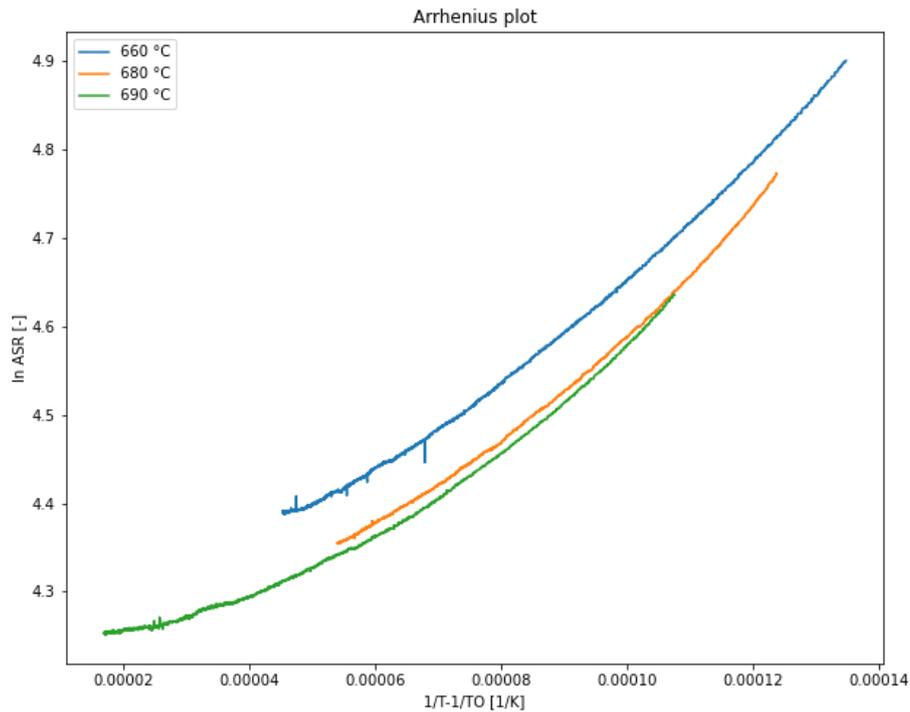
Figure 21: Arrhenius plot at variable fuel utilization, for different stack temperatures.

Even in this case, the plot has been made for the three stack temperatures for which the thermal equilibrium condition has been respected.

The unknown parameters (ASR_0 and E_a) have been derived through a linear fitting of the experimental data, using the least square method.
To apply the least square method, the variance and covariance have been calculated, through which the angular coefficient and the intercept of the fitted curve have been obtained. The equations used for the calculations are reported below:

The variance equation:

$$\sigma_x^2 = \frac{\sum_{i=1}^n (x_i - \bar{x})^2}{n}$$	(45)

The covariance equation:

$$\sigma_{xy} = \frac{\sum_{i=1}^n (x_i - \bar{x}) \cdot (y_i - \bar{y})}{n}$$	(46)

The equation for the angular coefficient for the linear fitting:

$$m = \frac{\sigma_{xy}}{\sigma_x^2}$$	(47)

The equation for the intercept:

$q = \bar{y} - m \cdot \bar{x}$	(48)

By looking at the slope and at the intercept of the linear fitting the parameters ASR_O and E_a of the Arrhenius law have been evaluated, through the equations 49 and 50 reported below:

$m = \dfrac{E_a}{R} \quad \blacktriangleright \quad E_a = m \cdot R$	(49)

$q = \quad \ln ASR_0 \quad \blacktriangleright \quad ASR_0 = e^q$	(50)

The values obtained are reported in figure 22, where the linear fitting is plotted.
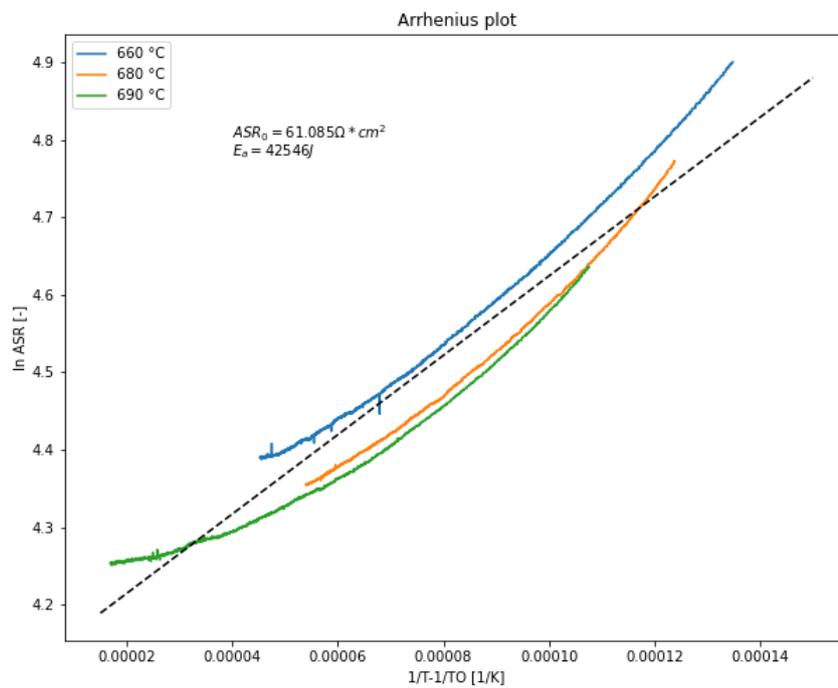

Figure 22: Arrhenius plot for SOFC at variable fuel utilization, with the linear fitting plotted applying the least square method. The parameters ASR_0 and E_a of the Arrhenius model have been calculated ($ASR_0 = 61.085 \,\Omega \cdot cm^2$ and $E_a = 42546 \, J$).

3.2 SOFC mode – Constant Fuel Utilization

3.2.1 Presentation of results

In this section, the results obtained from the tests performed at constant fuel utilization are presented.

The tests have been carried out at three different stacks temperatures (650, 670 and 690 °C). The stack temperature has been imposed fixing the set point temperature for the heaters of the stack and of the of the inlet streams (air and hydrogen).

The tests have been performed with a control current strategy: the current has been varied with a ramp, going from a partial load condition up to a full load working condition, to map the performance of the stack in different possible working zones.

The partial load has been defined as the 20% of the full load condition. This last one has been defined considering the maximum current value equal to 32 A in SOFC mode (maximum current density equal to 0.4 A/cm^2). Therefore, the corresponding hydrogen flow rate associated to the full load condition has been calculated through the Faraday law, assuming a maximum fuel utilization equal to 80%. It is equal to 19.8 Nl/min. Then, the hydrogen flow rate corresponding to the partial load has been calculated too, equal to 3.96 Nl/min.

Initially, a ramp-up of the hydrogen flow rate has been performed, from the partial load to the full load. The current has been varied automatically though a prepared script, imposing a constant fuel utilization of 40%. Therefore, considering the flowrates cited above and a fuel utilization equal to 40%, the current has varied from 3.24 A up to 16.24 A.

As can be seen from figures 23-25 below, once the hydrogen set point has been reached, it has been maintained constant. The current has been maintained constant for a certain time, to reach the thermal equilibrium. After having reached the temperature stabilization, the current has been increased up to the maximum value (32A) keeping fixed the hydrogen flow rate, to reach the fuel utilization equal to 80%.

Finally, after having reached the thermal stabilization, the ramp-down of the hydrogen flow rate has been started, automatically regulating the current value to keep constant the fuel utilization to the 80%. Therefore, in the ramp down the current has varied between 32 A and 6.4 A.

In the figures 23-25 below are shown the trends of the current, hydrogen flow rate and air outlet temperature, expressed as function of time, which show graphically what has been described above.

As can be seen, the air outlet temperature increases with the increase of current in the stack.
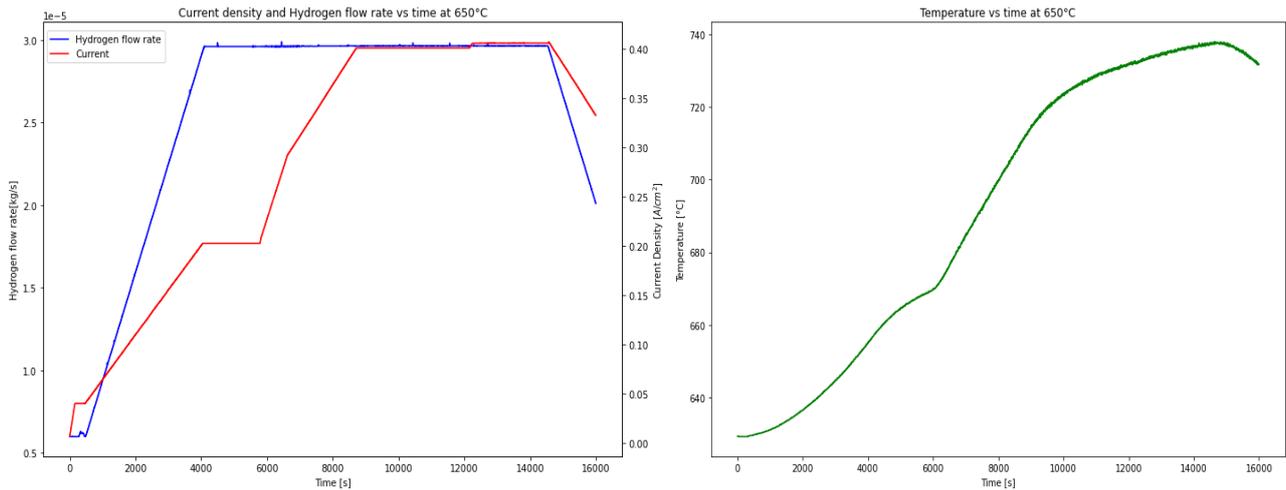
Figure 23: Trend of the current and of the hydrogen flow rate (on the left) and of the outlet air temperature (on the right) as function of the time, at T$_{stack}$=650 °C.
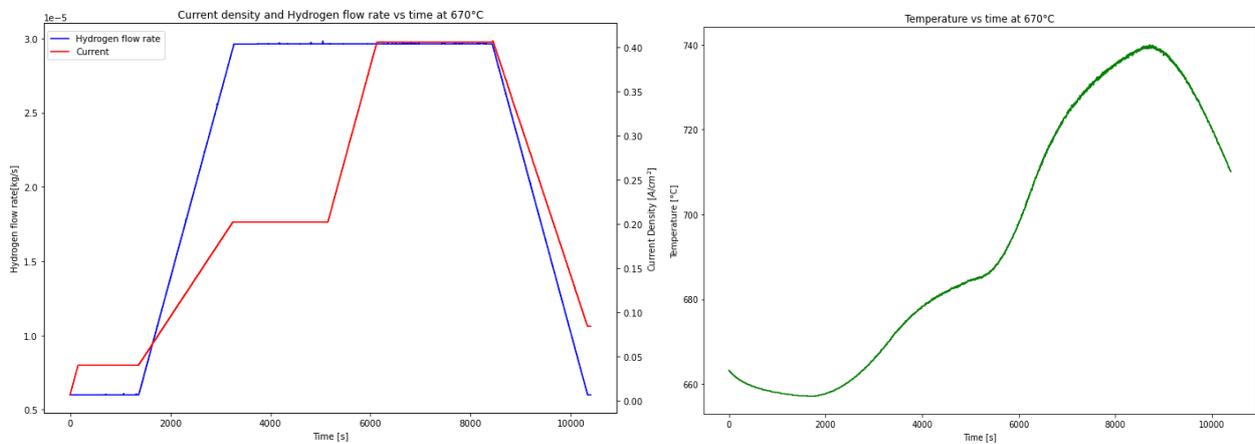

Figure 24: Trend of the current and of the hydrogen flow rate (on the left) and of the outlet air temperature (on the right) as function of the time, at T$_{stack}$=670 °C.
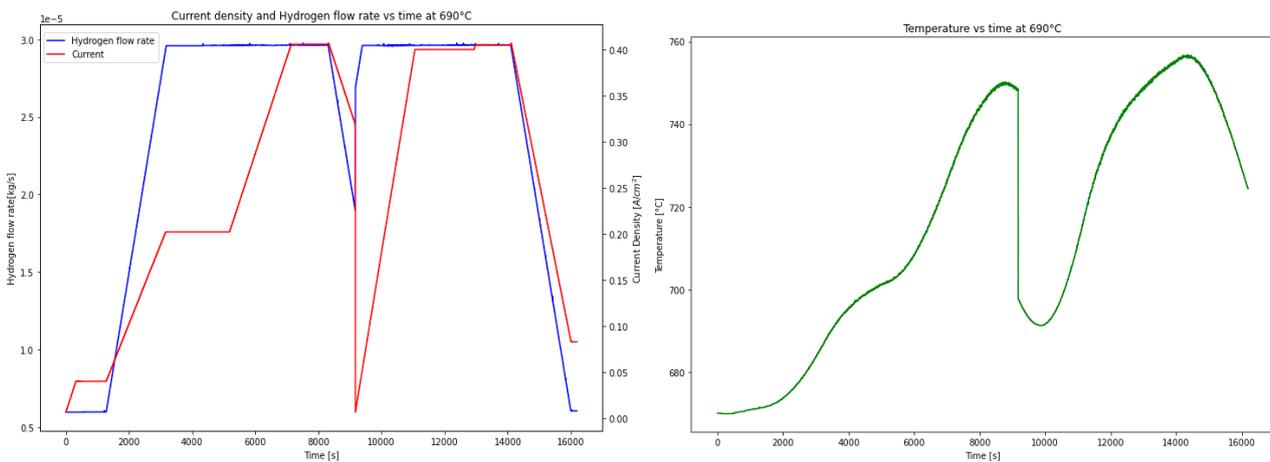

Figure 25: Trend of the current and of the hydrogen flow rate (on the left) and of the outlet air temperature (on the right) as function of the time, at T$_{stack}$=690 °C.

For the test at T$_{stack}$=650 °C, in the ramp-down some problems there have been with the automatic control of the current in the script. In fact, the fuel utilization in the ramp-down of the current has

not been maintained constant to the value of 80%, but it has continued to increase with the time, as can be seen from figure 26.
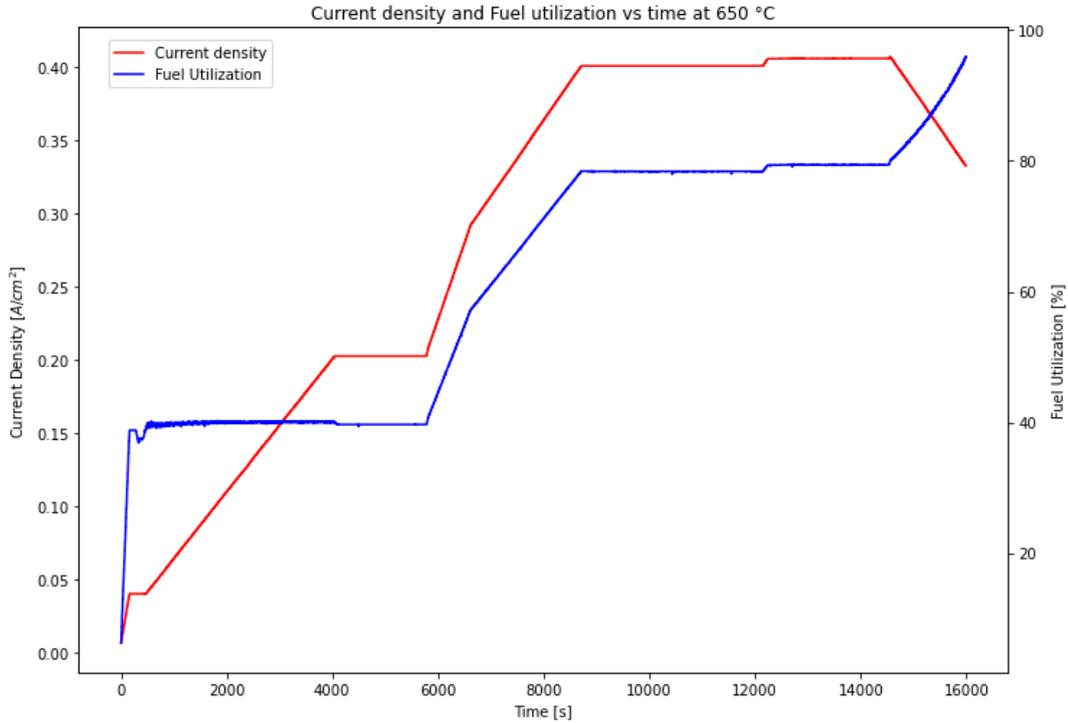

Figure 26: Trend of current density and fuel utilization as function of time, for T_{stack}=650 °C.

For this reason, in the next graphs the results obtained with the tests at T_{stack}=650 °C will not be presented.

On the other hand, the test performed at T_{stack}=690 °C has been interrupted automatically by the control system of the test bench, because the minimum stack voltage threshold had been overcome. In fact, when the stack is operated in control current, the risk is that the stack operates at a voltage value lower than the minimum allowed. To avoid this, a security alert has been inserted in the script to interrupt the test in case the minimum voltage threshold was overcome.

In the test at T_{stack}=690 °C, the hydrogen flow rate has been decreased too rapidly with respect to current flow. Therefore, the fuel utilization has increased too much, moving the working point of the stack in the concentration overpotential region, and causing a strong voltage decrease.
After the interruption, the test at T_{stack}=690 °C has been restarted and the data have been collected.

3.2.2 Elaboration and Discussion
The data obtained from the tests have been elaborated and the *V-I* curves have been obtained, which show the trend of the stack voltage as function of the current density.

The cells which compose the stack are divided in 8 clusters, each one composed by 9 cells, a part the last one which is composed by 7 cells. The stack voltage plotted is the sum of the voltages of the 8 clusters.

To plot the *V-I* curves, the trends with different fuel utilization (ramp-up and ramp-down of the current) have been separated. In figure 27, the curves for the stack temperatures equal to 670 and 690 °C are reported, for both the constant fuel utilization cases of 40% and 80%.

As can be seen from figure 27, for the fuel utilization equal to 40% the maximum current density reached is equal to 0.2 A/cm^2, while for the fuel utilization equal to 80% the maximum current density is equal to 0.4 A/cm^2, because the current has been continued to increase to reach a higher FU.

Moreover, in the case of FU=80%, the outlet air temperature is higher than the case of FU=40%. This causes a decrease in the slope of the *V-I* curves for the *FU*=80%, in which the voltage decreases slower increasing the current density.

Finally, from the figure 27 can be observed that in a certain region of the plot, at parity of current density, for FU=40% higher stack voltage values can be obtained with respect to the case FU=80%. This aspect will influence the trend of the stack efficiency.
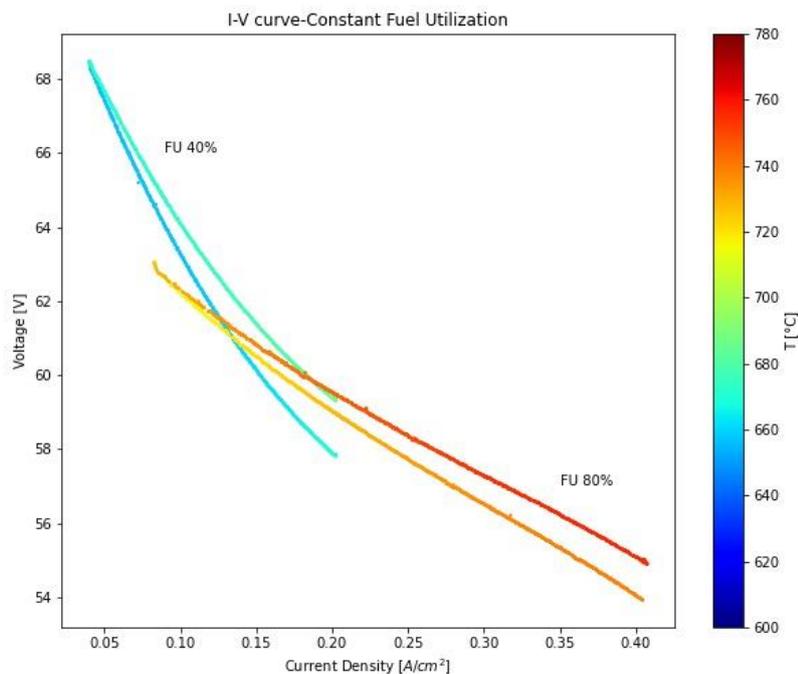

Figure 27: *V-I* curves for constant fuel utilizations (40% and 80%), for two different stack temperatures T$_{stack}$=670 °C and T$_{stack}$=690 °C.

Then, the stack efficiency has been calculated, considering a theoretical and empirical value. The difference between them stays in the fuel utilization factor, taken into account in the calculation of the empirical efficiency.
The considerations done on the efficiency calculation for the variable fuel utilization condition are valid even for this case of constant fuel utilization.

The theoretical efficiency has been calculated as follows:

$$\eta_{SOFC,theoretical} = \frac{V}{V_{OCV}} \qquad (51)$$

In equation 51, V represents the stack voltage, while V_{OCV} is the open circuit voltage associated to the stack temperature tested.

The empirical efficiency has been calculated multiplying the theoretical efficiency for the fuel utilization factor at which the tests have been performed.

$$\eta_{SOFC,theoretical} = \frac{V}{V_{OCV}} \cdot FU \qquad (52)$$

Their trends can be observed in figure 28 and 29.

For the theoretical efficiency some considerations can be done:

- Increasing the current density, the efficiency value decreases, because of the decrease in the stack voltage value.
- At parity of fuel utilization, higher efficiencies are associated to higher outlet air temperatures. In fact, the open circuit voltage decreases with the increase of the stack temperature and so the ratio $\frac{V}{V_{OCV}}$ is higher for higher stack temperature.
- At parity of current density, in the region of low current density values, the stack efficiency is higher for the case of lower fuel utilization (40%) than in the case of higher fuel utilization (80%). This could be explained with the lower voltage values associated to those current density, in case of higher FU. These lower voltage values could be linked to the concentration losses, typical of the working zone with higher values of fuel utilization.
- At parity of efficiency, higher current density values are associated to higher outlet air temperatures.

For what concern the empirical efficiency, it has been calculated considering in the formula the impact of the fuel utilization factor. Therefore, its value will be lower than that of the theoretical efficiency, considering that not all the fuel inserted will react in the stack.

So, considering the empirical stack efficiency trend, it can be noticed that maximum efficiency values stay around 58% for the case of FU=80% and 32% for the case of FU=40%, considering a T_{stack}=690 °C.
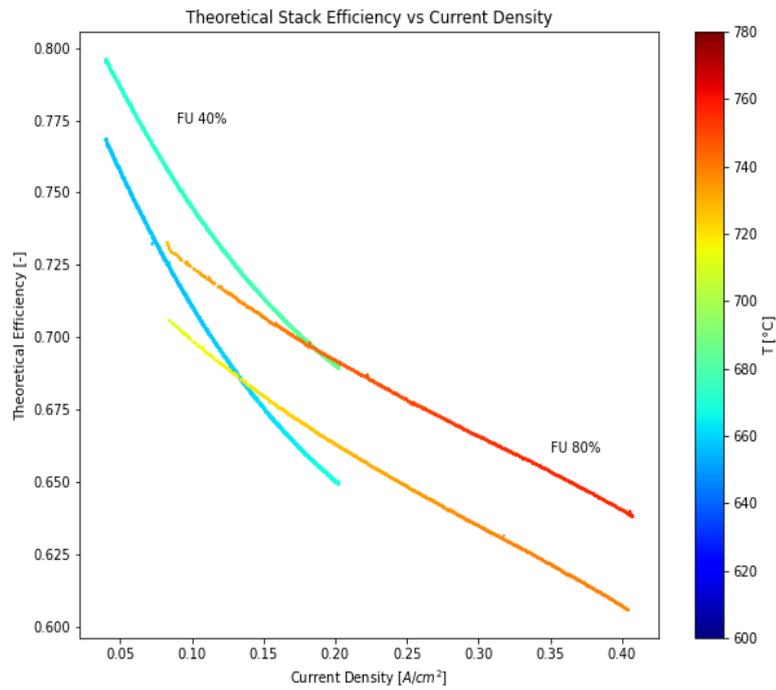
Figure 28: Theoretical stack efficiency at constant fuel utilization (40% and 80%), for T_{stack}=670 °C and T_{stack}=690 °C.
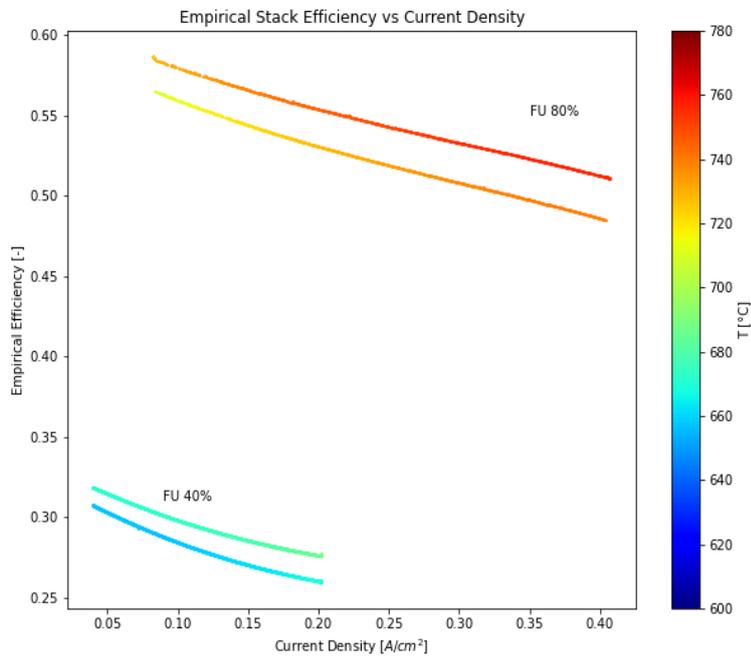

Figure 29: Theoretical stack efficiency at constant fuel utilization (40% and 80%), for T_{stack}=670 °C and T_{stack}=690 °C.

Finally, as previously said, even in this case the OCV voltage in single trend is assumed constant and taken at the initial stack temperature, fixed as set point for the inlet streams. This is an approximation, because the temperature of the outlet streams progressively increases with the

increase of current and so even the stack voltage should progressively decrease. This approximation could lead to an underestimation of the stack efficiency values, because the stack voltage value at a higher temperature is compared with the OCV voltage associated at a lower temperature.

To be more precise, the OCV voltage should be calculated for each point of the curve, being the temperature variable along it.

3.3 SOEC mode – Variable Steam Utilization

3.3.1 Presentation of results

In this section the results obtained from the tests performed in SOEC mode, at variable steam utilization, are presented. These tests have been carried out with a control voltage strategy.

The voltage has been varied with a ramp and the correspondent current value has been measured. The inlet steam flow rate has been kept constant. As consequence the steam utilization of the stack has varied linearly with the different current values.

In the following plots the trends of the stack current and stack voltage as function of the time are shown. It is possible to observe that the voltage has been varied with a linear ramp-up equal to 0.25 V/min (from the OCV, around 60V, up to 98 V) and a linear ramp-down equal to 1 V/min. The current has varied as consequence of the voltage variation.

These ramp variations have been carried out for different stack temperatures (680, 690, 700, 710, 720, 730, 740 and 750 °C). The trends of the voltage, current and outlet air temperature, for three different stack temperatures (680, 710, 740 °C), taken as samples, are presented below in figures 30-32.
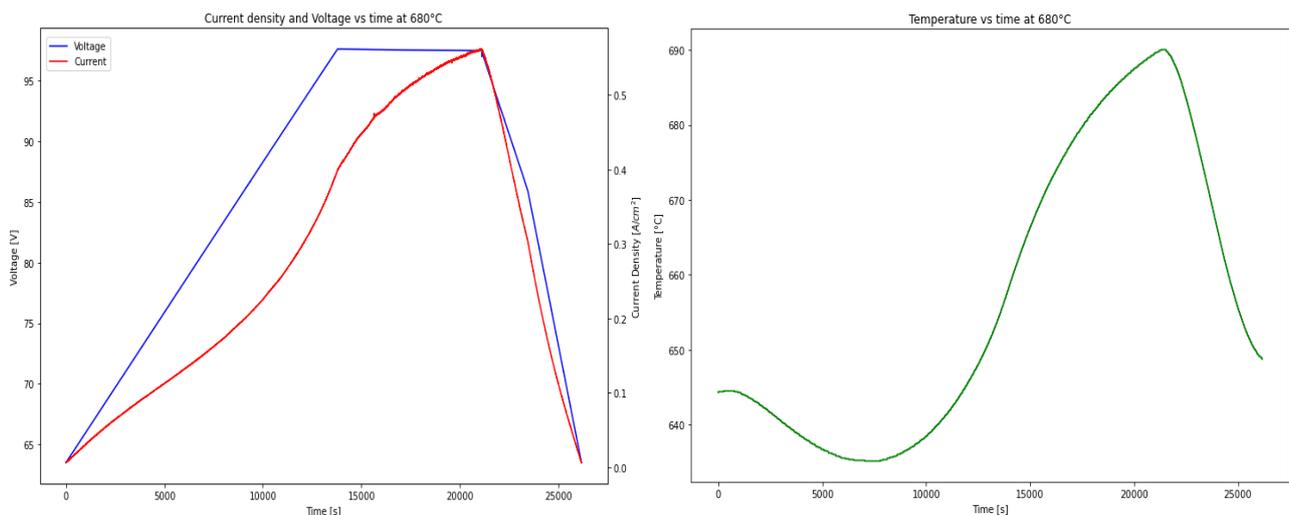

Figure 30: Current density and voltage with respect to time (on the left) and air outlet temperature as function of the time (on the right), for T_{STACK}=680 °C.
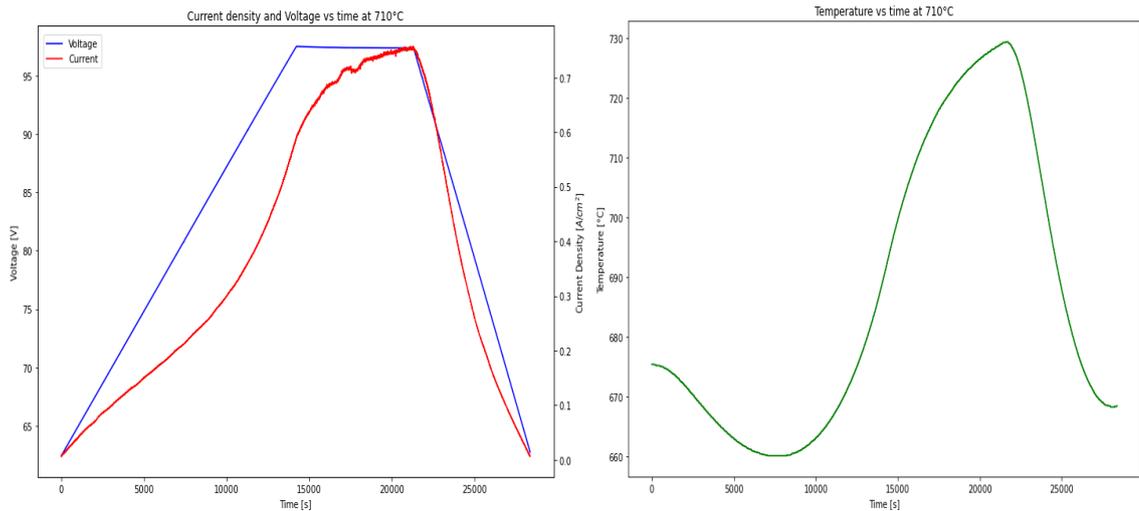
Figure 31: Current density and voltage with respect to time (on the left) and air outlet temperature as function of the time (on the right), for T_{STACK}=710°C.
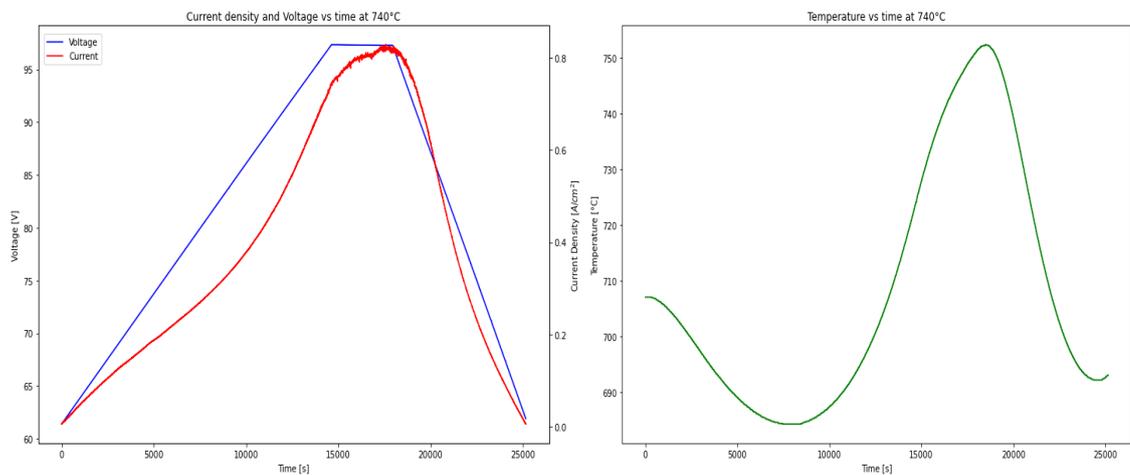

Figure 32: Current density and voltage with respect to time (on the left) and air outlet temperature as function of the time (on the right), for T_{STACK}=740°C.

When the voltage has reached the maximum value, before to start the ramp-down, it has been maintained to a constant value to reach the thermal equilibrium of the inlet and outlet stack streams. It can be noticed that even when the voltage is not varied, the current continues to increase. This happens because even when the stack voltage is kept constant, the cells have not reached the thermal equilibrium and the temperature continues to increase. So, the cells resistance decreases, and the current continues to increase.

However, when the current reaches its maximum values, some irregularities can be noticed in its trend. They are present because for those current values the steam utilization is high and so all the steam which is injected in the stack is soon consumed, generating some instabilities in the cells.

For what concern the trend of the outlet air temperature from the stack as function of the time, it follows a cyclic path with the increase of the voltage: initially it decreases, then it increases up to a maximum value. This happens because of the endothermic and exothermic behaviour of the stack in SOEC mode. In fact, at the beginning the stack works in endothermic condition and the

66

temperature of the outlet air decreases, with respect to the initial condition at t=0. After a certain time, the temperature starts to increase, up to the point in which it reaches the initial value. In this point (around t=1200 s), the thermoneutrality condition has been reached, because the air exits at the same temperature at which it has entered.

Then, the outlet air temperature continues to increase with the increase of the voltage, overcoming the initial value. In this area, the stack works in exothermicity condition and so the voltage has overcome thermoneutral voltage value. Finally, in the last part of the plot, the outlet air temperature decreases again because of the decreasing of the stack voltage (ramp-down). This means that the voltage decreases toward the thermoneutral voltage. Therefore, the stack still works in exothermicity, but the heat produced decreases, and so the outlet air temperature decreases too.

3.3.2 Elaboration and Discussion

In the elaboration step, the *V-I* curves have been realized, for the 8 different stack temperatures analysed. The stack temperature is defined as the temperature fixed to the heaters of the inlet streams (air and steam) and it is assumed to be the inlet temperature of the streams, neglecting the thermal dispersions up to the inlet of the stack.

On the colorbar is shown graphically the air outlet temperature for each point in the curve, which is assumed to be representative of the temperature variation in the stack for the different working conditions, because of its high flow rate.

In figure 33, all the *V-I* curves for the different stack temperatures have been plotted on the same graph.
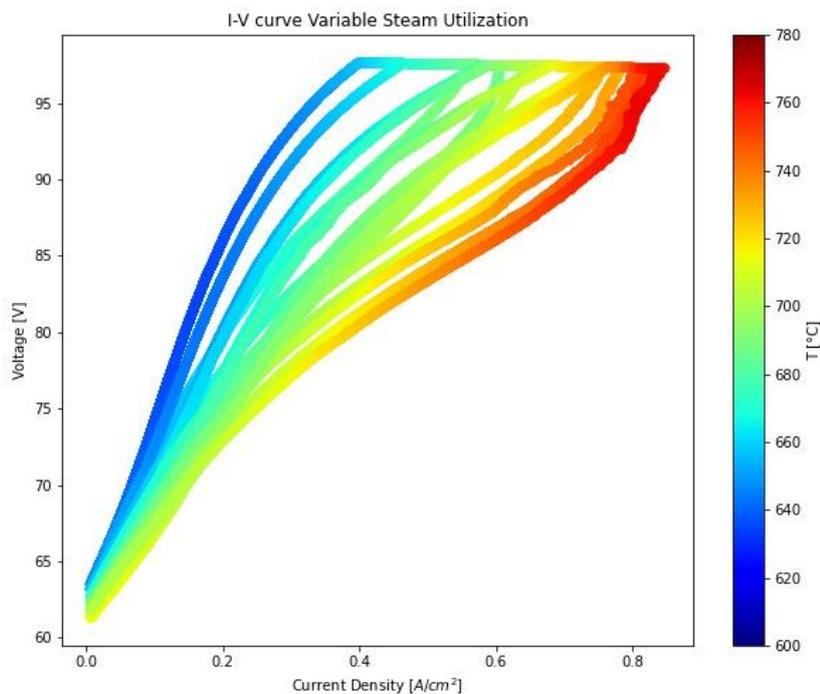
Figure 33: *V-I* curves for different stack temperatures.

It can be noticed how increasing the stack voltage the stack current increases too.

Even in this plot it is possible to see that even when the voltage is kept constant, the current continues to increases. Moreover, increasing the stack temperature, the slope of the curves decreases, and so for the same voltage values the current is higher at higher temperatures. This can be explained through the decreasing of the cells resistance with the increase of the temperature.

Considering the curves for one single temperature, it can be noticed that during the increase and decrease of the voltage ramp, the current does not follow the same cycle but an hysteresis cycle is present. In fact, during the decreasing ramp, the current values are higher than those had during the increasing ramp, at parity of voltage value. This happen because when the voltage is decreased the cells are already heated-up and the cells resistance is lower. This can be noticed observing the the air oultet temperature represented in the colorbar, which is higher during the decreasing ramp of the voltage with respect to the air oultet temperature during the increasing ramp.

Concerning the stack efficiency, it has been calculated using two different formulations, summarized below:

- Theoretical stack efficiency
- Empirical efficiency

The theoretical stack efficiency has been calculated as follows:

$$\eta_{SOEC,theoretical} = \frac{\dot{m}_{H_2} \cdot LHV_{H_2}}{P_{el}}$$

(53)

At the denominator as input has been considered the electrical power P_{el} given in input to the stack, calculated as the product between voltage and current, while at the numerator as output has been considered the power content of the hydrogen produced, where $\dot{m}_{H_2}$ is its mass flow rate and LHV_{H_2} is the hydrogen low heating value, equal to 120 MJ/kg.

The theoretical stack efficiency can be expressed even as the ratio between the thermoneutral voltage of the stack V_{th} and the operative voltage of the stack V, as reported in the equation 54, obtained explicating the terms at numerator and denominator present in equation 53.

$$\eta_{SOEC,theoretical} = \frac{V_{th}}{V}$$

(54)

In fact, the LHV_{H_2} can be considered equal to the enthalpy variation of the reaction, being this latter defined as the total energy released in the oxy-reduction reaction.

The thermoneutral voltage V_{th} is defined as the ratio between the variation of the enthalpy in the steam electrolysis reaction and the product of the oxidation number of the hydrogen (*z*=2) and the Faraday's constant (*F*=96485 C/mol), as reported in equation 55. It represents the cell voltage in condition of thermoneutrality. To obtain the stack value, the result obtained from equation 55 has to be multiplied for 70 (number of cells in the stack).

For the single cell V_{th} has resulted equal to 1.393 V.

$$V_{th} = \frac{\Delta h_{reaction}}{z \cdot F} \qquad (55)$$

The enthalpy of reaction $\Delta h_{reaction}$ is function of the temperature at which the reaction occurs (approximated with the stack temperature). Considering that tests have been performed at different temperatures, an average temperature value between the minimum and the maximum one (680 and 750 °C, respectively) has been considered. The enthalpy of the reaction considered in equation 55 has been associated to this temperature, equal to 715 °C.

Once the temperature has been defined, the enthalpy variation has been calculated as the difference of enthalpy between the products (outlet flows) and reagents (inlet flows) in the stack. As outlet flows only the hydrogen and the oxygen have been considered, while as inlet flow only steam has been considered. Their enthalpy, function of the temperature, has been calculated through the polynomial formulation taken from NIST database and expressed in the equation 56, with respect to the reference state (corresponding to T=25 °C and p=1 atm).

$$h = A \cdot t + B \cdot \frac{t^2}{2} + C \cdot \frac{t^3}{3} + D \cdot \frac{t^4}{4} - \frac{E}{t} + F - H \qquad (56)$$

A, B, C, D, E, F and H are some constants, defined for a specific substance and for a certain temperature on the NIST database. t is the temperature expressed in kelvin and divided for 1000.

$$t = \frac{T\ [K]}{1000} \qquad (57)$$

To obtain the thermoneutral voltage value for all the stack, the value obtained from formula 55 has been multiplied by 70 (the number of cells in the stack). Then, equation 54 has been applied and the theoretical stack efficiency has been calculated. It is defined theoretical because it does not take into account the steam utilization factor.

Concerning the empirical efficiency, it has been calculated as shown in equation 58, considering the contribution of the steam utilization U_{steam}.

$$\eta_{SOEC,empirical\ efficiency} = \frac{V_{th}}{V} \cdot U_{steam} \qquad (58)$$

The plots obtained from the efficiencies analysis are shown below.

The theoretical and empirical stack efficiency as function of the current density, for all the stack temperatures analysed, are shown in figure 34.
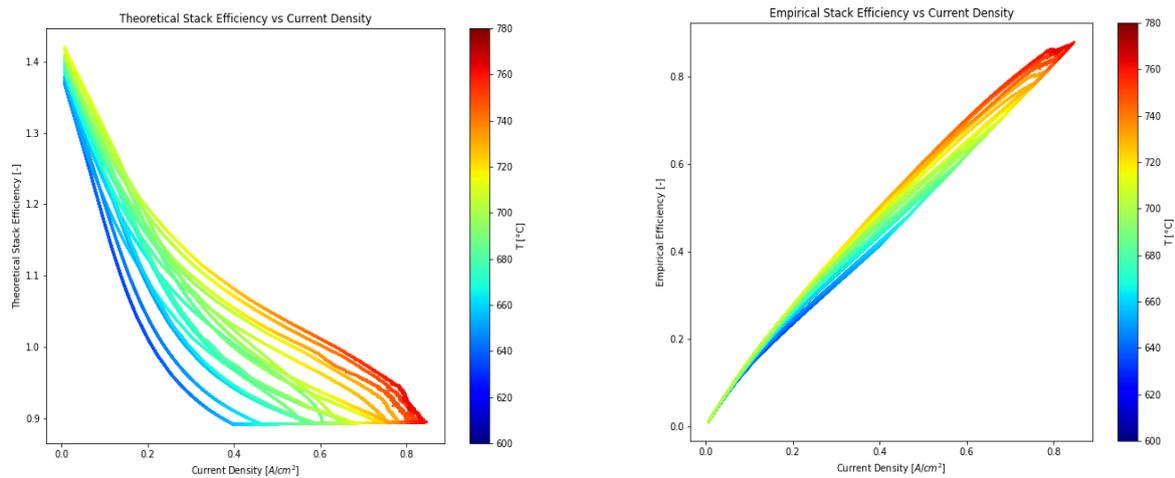
Figure 34: The theoretical stack efficiency (on the left) and the empirical stack efficiency (on the right) as function of the current density, for different stack temperatures (680, 690, 700, 710, 720, 730, 740, 750 °C).

From these efficiency curves it can be noticed that the theoretical efficiency is higher than 1 for some current density values (and therefore for a certain range of voltage values). This happen when the stack works at voltage values V lower than the thermoneutral voltage V_{th}.

In this case, the stack works in endothermicity condition, and the thermal input $T \cdot \varDelta s$ required from the stack occupies a consistent part in the energy requirement. However, in the theoretical stack efficiency formulation as energy input at the denominator only the electrical input $\varDelta g$ is considered. Therefore, efficiencies higher than 1 are possible in this working condition. Reaching the thermoneutral voltage, the stack efficiency value is 1.

The thermoneutral voltage increases with the stack temperature (because it depends on the enthalpy of the reaction). Therefore, the correspondent current density associated to 100% of stack efficiency increases with the increase of temperature.

Continuing to increase the voltage, over the thermoneutral voltage, the efficiency continues to decrease and below the thermoneutral voltage the stack works in exothermicity. In this condition, the thermal input required by the reaction is covered by the heat released to the irreversibility of the mass transport phenomena in the stack, while the electric input increases. This explains the decrease of the theoretical efficiency with the increase of the stack voltage.

Finally, it is interesting to note how the theoretical efficiency varies with the stack temperature. Increasing the stack temperature, higher values of efficiency can be obtained for the same value of current density or observing it from another point of view, higher current density can be obtained for the same value of efficiency. This means that at parity of hydrogen production smaller cells can be used, and so it is possible to reduce the costs.

However, the trend of the theoretical efficiency does not represent a realistic efficiency of the stack, because it does not consider the steam utilization. To have a more realistic behaviour of the performance of the stack, the empirical efficiency has to be observed, shown on the right in the figure 34.

Observing the trend of the empirical efficiency as function of the current density, it can be seen that it increases increasing the current density. This behaviour is opposite with respect to that of the theoretical efficiency. The only difference between the two trends is made by the steam utilization factor. In the empirical efficiency, the theoretical efficiency is multiplied for the steam utilization to take into account the real behaviour of the stack, considering that there is the utilization factor for the steam which is injected in the stack.

For lower current density, the steam utilization is low and so, even if the ratio $\frac{V_{th}}{V}$ is high, the empirical efficiency results lower with respect to the working conditions with higher current density.

The effect of the temperature is also relevant: increasing the stack temperature, for the same current density values, the empirical efficiency increases. This is due to the increase of the $\frac{V_{th}}{V}$ ratio (V_{th} is higher for higher temperature of reaction) and to the increase of the steam utilization with the increase of temperature, due to the higher current values reached.

After the efficiency analysis, the behaviour of the area specific resistance (ASR) has been analysed, to have a more complete map of the performance of the stack in electrolysis mode. The ASR has been plotted as function of the theoretical efficiency and empirical efficiency of the stack. The effect of the stack temperature and of the steam utilization have been considered too in the plots.

The ASR has been calculated as described in the SOFC section, as the ratio between the difference between the operative stack voltage and the open circuit voltage (OCV) (at numerator) and the operative current density (at the denominator).

$$ASR = \frac{V - V_{OCV}}{i}$$	(59)

In the stack tested, 8 clusters are present and for each of them the voltage is measured with sensors.

The V term present in the ASR formulation has been calculated starting from the voltage value of the last cluster near the outlet of the stack (cluster 8). This cluster is composed by 7 cells; therefore, the cluster voltage has been divided for 7 and then multiplied for 70 (total number of cells) to obtain an approximated value for the stack voltage V.

This last cluster has been chosen considering that it is near the outlet of the stack and so it will be at a temperature quite similar to that of the outlet air, which influence the ASR trend. Therefore, the ASR calculated will be associated in a more precise way to that temperature.

Similarly to the SOFC case, the trend of the ASR as function of the stack efficiencies has been plotted.

In figure 35, the trend of ASR as function of the theoretical efficiency is expressed, with the indication of the outlet air temperature and of the steam utilization on the colour bar.

It can be noticed how, considering the same value of stack efficiency, the ASR decreases with the increase of the stack temperature. The ASR, in fact, as previously said, represents the equivalent overall resistance of the cells and it is function of the temperature.

However, the following comments can be reported:

- The curves initially increase, up to a maximum value, and then they decrease with the increase of theoretical efficiency of the stack. This could be explained with the cyclic behaviour of the outlet air temperature with the variation of the stack voltage (see plots of the voltage and temperature as function of the time, reported in the results section).

- Concerning the relation with the steam utilization, it is possible to notice how at higher currents (lower theoretical efficiencies) corresponds higher steam utilization. Therefore, even in this case, lower ASR are associated to higher steam utilization values.
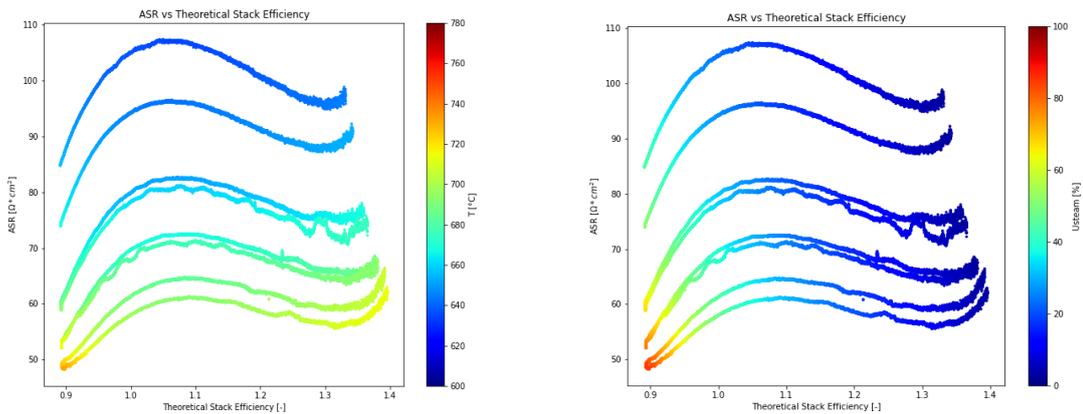
Figure 35: Trends of the ASR as function of the theoretical efficiency, for the different stack temperatures (680, 690, 700, 710, 720, 730, 740, 750 °C). In the colour bar is indicated the outlet air temperature (on the left) and the steam utilization (on the right), calculated for each point in each curve.

In figure 36 the relations between ASR, theoretical stack efficiency, outlet air temperature and steam utilization are summarized.
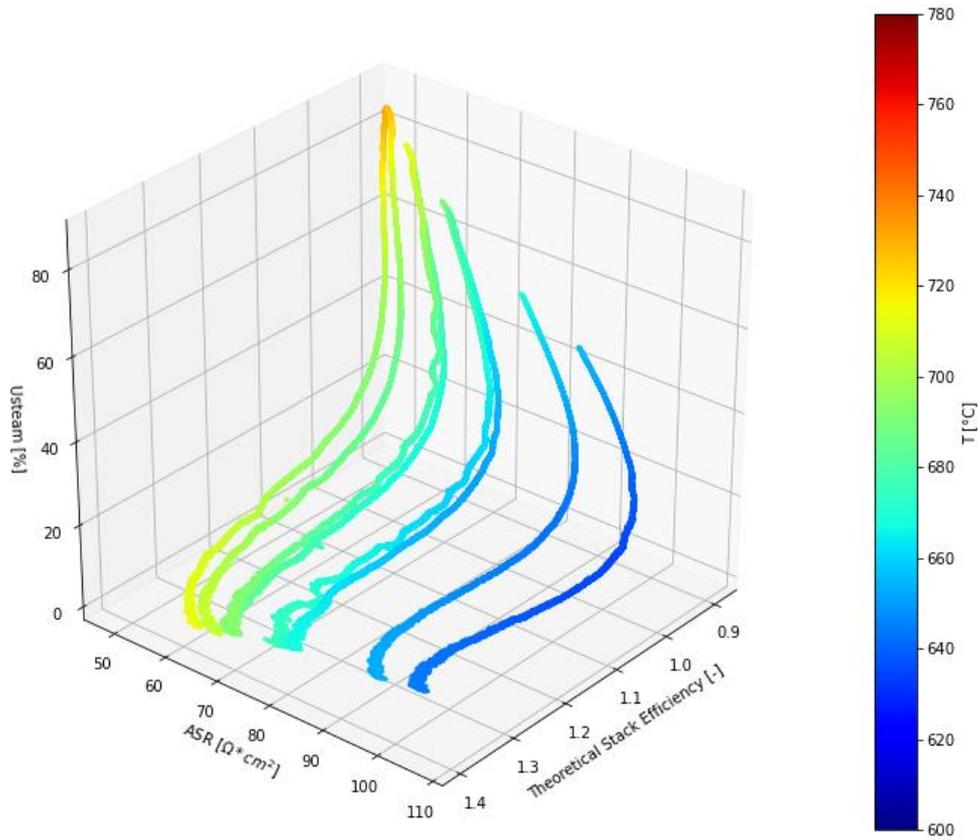
Figure 36: 3D plot with the representation of the ASR trends as function of the theoretical stack efficiency and steam utilization. In the colour bar is represented the outlet air temperature for each point in each curve.

Finally, the ASR has been plotted also as function of the empirical stack efficiency.

Even in this case, as for the plot in function of the theoretical efficiency, a cyclic trend of the ASR can be seen, associated to the variation of the outlet air temperature with the stack voltage variation.

As reported for the others plots, the lowest ASR value, for a certain stack temperature tested, is associated to the highest steam utilization value reached in that test.

In a 3D plot, shown in figure 38, the relation between the ASR, the empirical stack efficiency, the outlet air temperature and the steam utilization has been summarized.
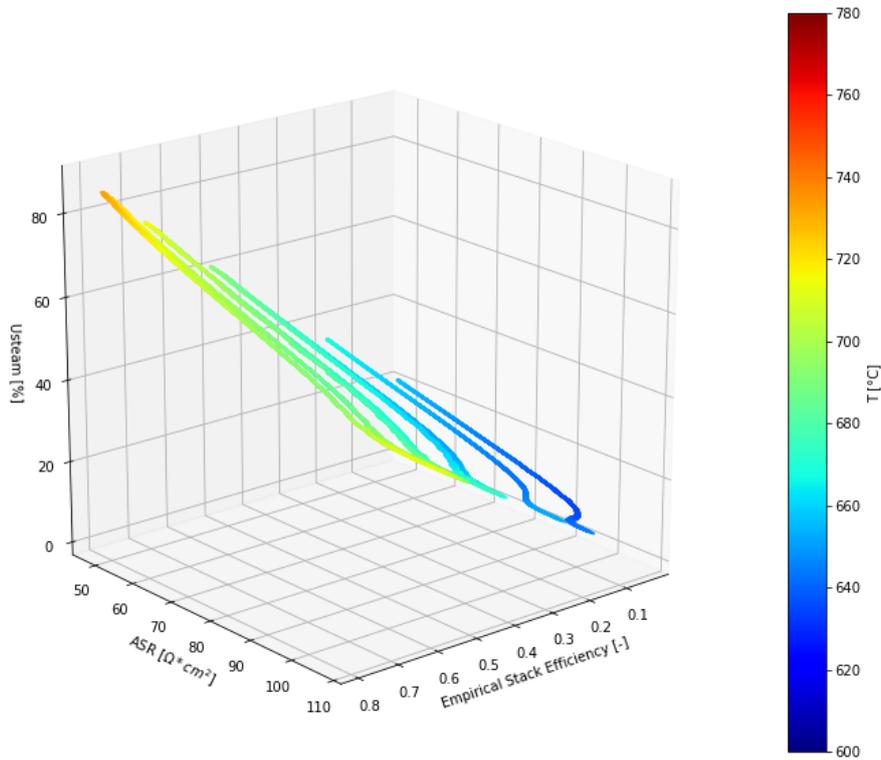

Figure 38: 3D plot with the representation of the ASR trends as function of the empirical stack efficiency and steam utilization. In the colour bar is represented the outlet air temperature for each point in each curve.

Finally, in analogy to the analysis carried out for the SOFC mode, the Arrhenius plot has been realized, for the different stack temperatures, as shown in figure 39.

The same considerations done for the SOFC case are valid also in this SOEC case. It is a graph of the natural logarithm of the ASR as function of the inverse of the stack temperature T minus the inverse of the reference temperature ($T_0 = 800\ °C$), expressed in Kelvin.

The Arrhenius trend is linear, and it decrease when the temperature increases (with the decrease of the inverse of temperature).
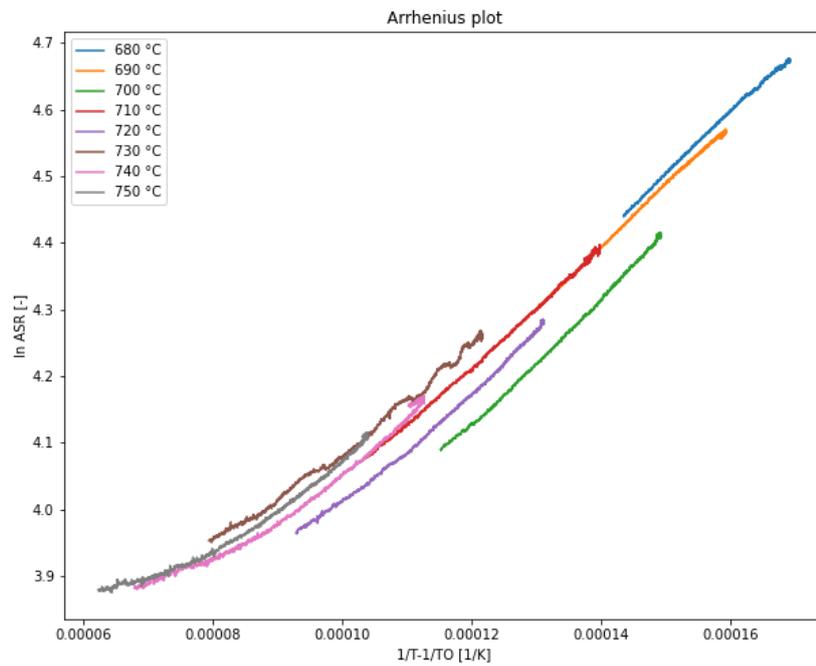
Figure 39: Arrhenius plots for the different stack temperatures (680,690, 700, 710, 720, 730, 740, 750 °C).

Even in this case a linear fitting has been plotted in figure 40, applying the least square method, and the Arrhenius parameters ASR_0 and E_a, corresponding respectively to the ASR at the reference temperature T_0 and to the activation energy of the reaction, have been calculated. Their values are reported in figure 40.
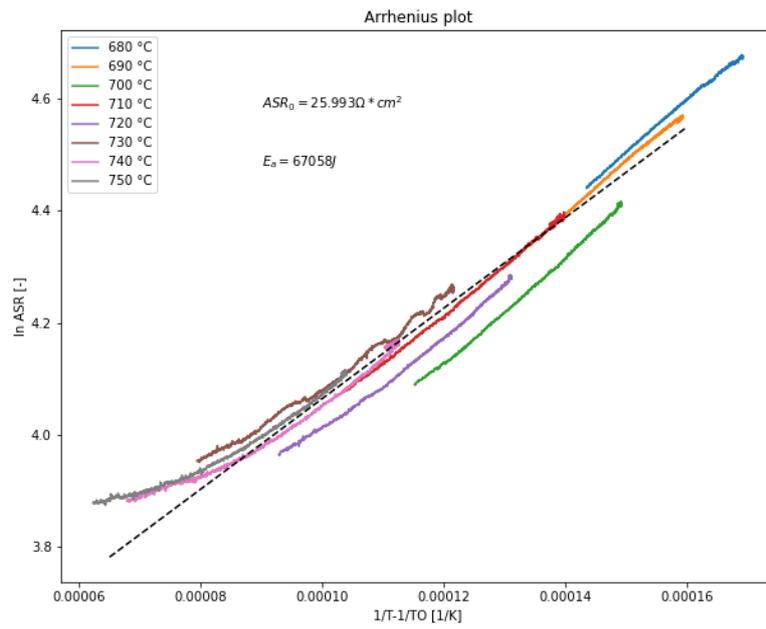
Figure 40: Arrhenius plot for SOEC at variable steam utilization, with the linear fitting plotted applying the least square method. The parameters ASR_0 and E_a of the Arrhenius model have been calculated ($ASR_0 = 25.993 \ \Omega \cdot cm^2$ and $E_a = 67058 \ J$).

3.4 SOEC mode – Constant Steam Utilization

In this case, the tests have been performed in control current. The current has been varied with a ramp and the correspondent voltage value has been measured. Moreover, to keep constant the steam utilization, the inlet steam flow rate has been varied proportionally with the current.

Four stack temperatures have been analysed (710,720,740 and 750 °C) and for each temperature the current has been varied with a ramp to reach four different values of steam utilization (25, 50,75, 90 %).

The stack voltage has varied as consequence of the current variation.

3.4.1 Presentation of results

In the plots below are reported the current and voltage variations as function of the time.
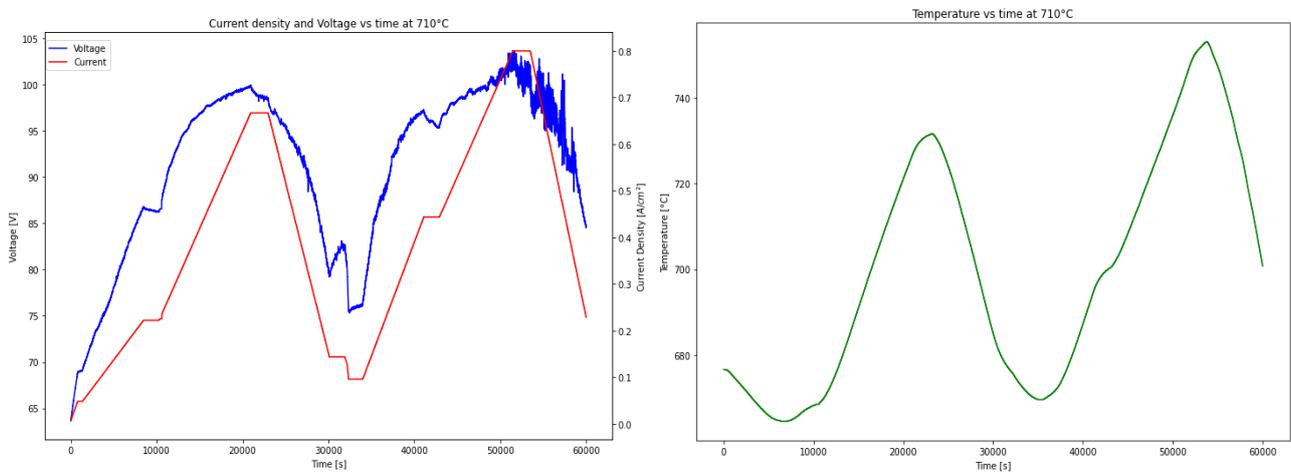
Figure 41: Trends of the stack voltage and current (on the left) and of the outlet air temperature (on the right) as function of the time, at constant steam utilization, for T_{stack}=710 °C.
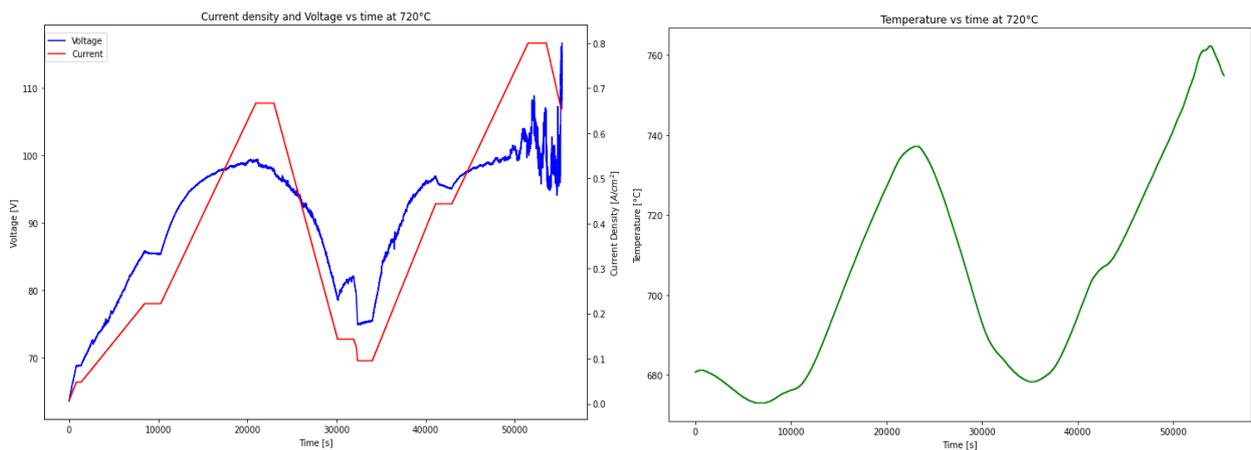
Figure 42: Trends of the stack voltage and current (on the left) and of the outlet air temperature (on the right) as function of the time, at constant steam utilization, for T_{stack}=720 °C.
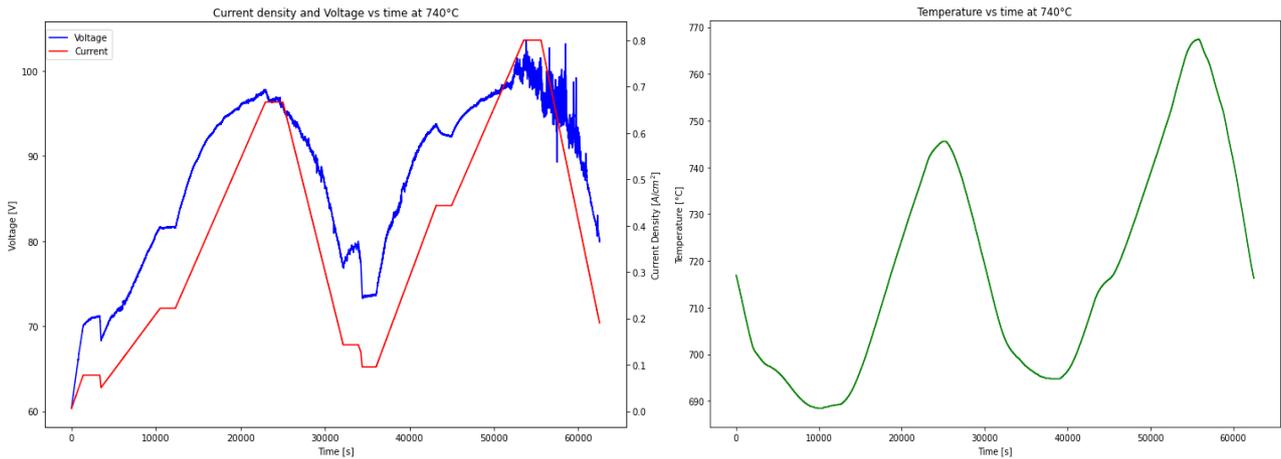
Figure 43: Trends of the stack voltage and current (on the left) and of the outlet air temperature (on the right) as function of the time, at constant steam utilization, for T_{stack}=740 °C.
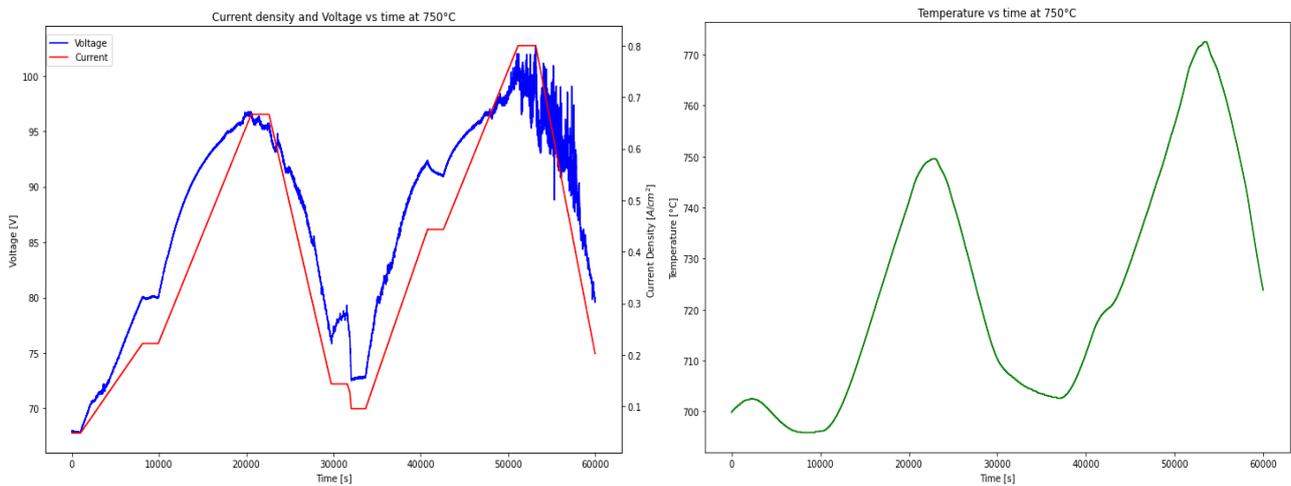

Figure 44: Trends of the stack voltage and current (on the left) and of the outlet air temperature (on the right) as function of the time, at constant steam utilization, for T_{stack}=750 °C.

With the voltage variation, even the stack temperature has varied with a cyclic path, as described for the case with variable steam utilization. Moreover, for the second current ramp variation the peak temperatures reached are higher because of the higher values of current.

3.4.2 Elaboration and Discussion

In figure 45, the *V-I* curves have been realized, for the different stack temperatures, for each steam utilization value.

In the colour bar is indicated the temperature of the outlet air from the stack.
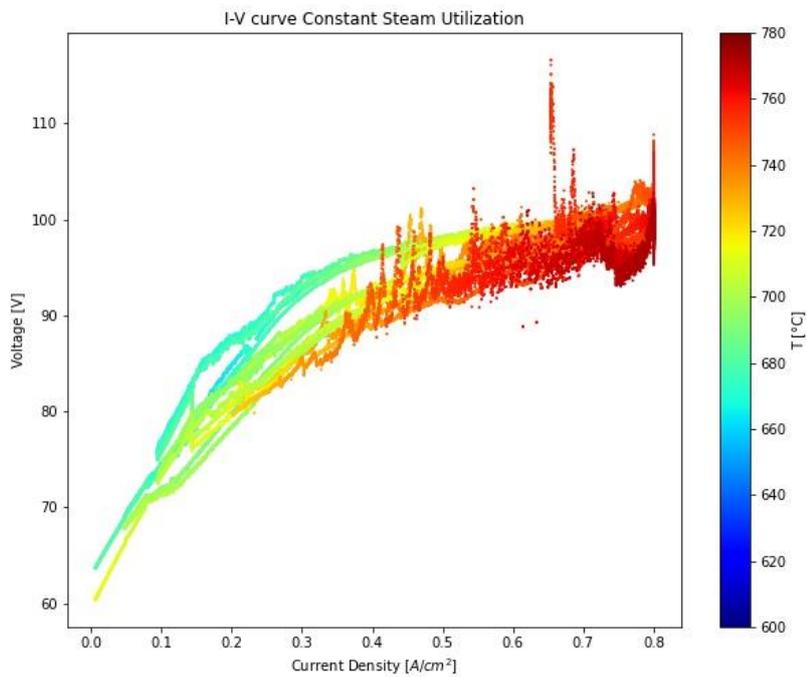
Figure 45: i-V curve at constant steam utilization (25, 50, 75 and 90%). For each steam utilization value, different stack temperatures have been plotted (710, 720, 740 and 750 °C).

From the figure 46, the detail of the different *V-I* curves associated to different values of constant steam utilization can be seen. It is interesting to mention how to higher steam utilizations are associated higher current values. Moreover, for a same steam utilization value, at parity of current, the voltage is lower for the curves at higher temperature.

The curves at high steam utilization (90%) present an irregular trend, due to the high current values and, therefore, to the concentration overpotential region.
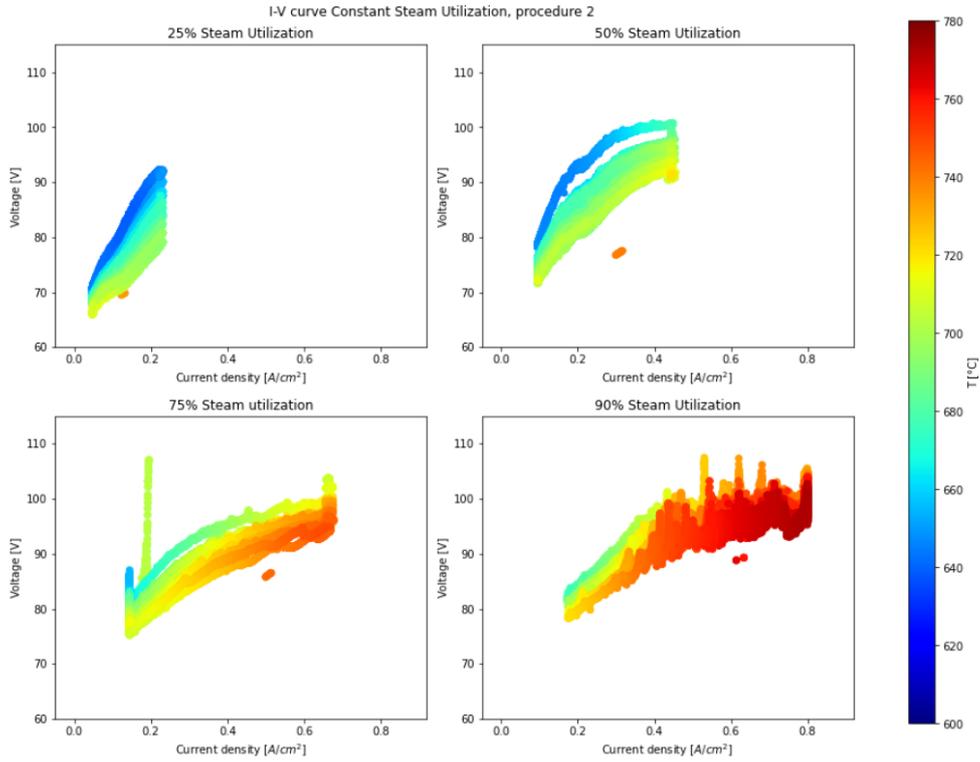
Figure 46: *V-I* curves, separated on the basis of the different steam utilization.

Then, the efficiency analysis has been performed, calculating two stack efficiencies. Therefore, the theoretical and empirical stack efficiencies have been calculated and plotted. They have been calculated as reported in the SOEC variable steam utilization section.

Therefore, the theoretical efficiency has been calculated as shown in in equation 60:

$$\eta_{SOEC,theoretical} = \frac{V_{th}}{V}$$	(60)

The empirical efficiency has been calculated as shown in equation 61:

$$\eta_{SOEC,empirical\ efficiency} = \frac{V_{th}}{V} \cdot U_{steam}$$	(61)

The trends of the stack efficiencies are reported in figure 47 and 48, for each steam utilization value, at the different stack temperatures tested.

In figure 48, it can be noticed how the stack efficiency trends are differentiated when the steam utilization factor is considered. At higher steam utilizations, higher stack efficiencies values are associated.

A linear fit for the empirical efficiency at each steam utilization has been made. It can be noticed that the temperature increases with the steam utilization. Additionally, the stack efficiency increases with the temperature and, therefore, with the steam utilization.

80

Finally, at parity of steam utilization, both the stack efficiencies decrease with the increase of current density, as reported for the SOFC case at constant fuel utilization, because of the increase of the overvoltage losses.
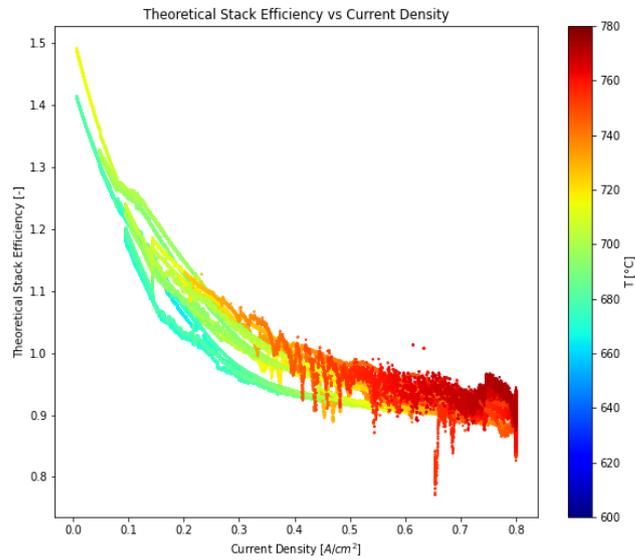
Figure 47: Theoretical stack efficiency as function of current density, at constant steam utilization (25, 50, 75 and 90%). For each value of steam utilization, different stack temperatures have been plotted (710, 720, 740 and 750 °C).
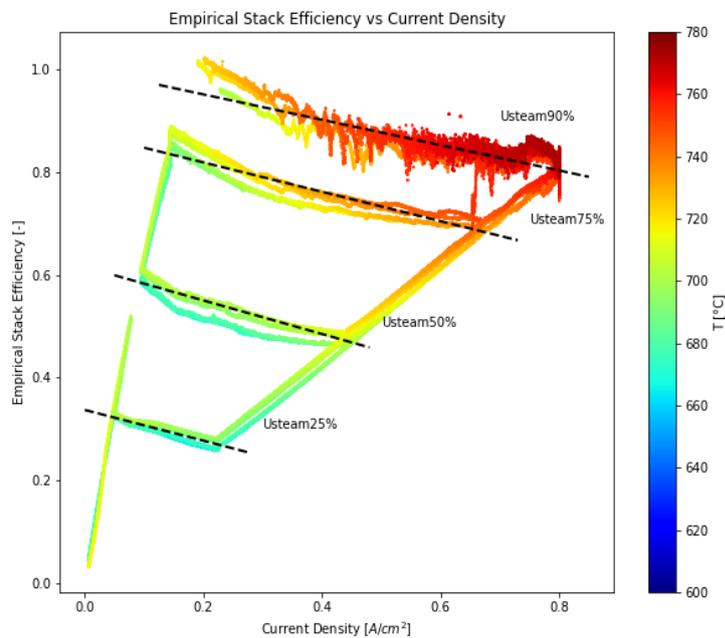

Figure 48: Empirical stack efficiency as function of current density, at constant steam utilization (25, 50, 75 and 90%). For each value of steam utilization, different stack temperatures have been plotted (710, 720, 740 and 750 °C).

3.5 Stack Round-Trip Efficiency

The round-trip efficiency of the stack has been calculated starting from the stack efficiencies in the SOFC and SOEC modes.

It has been defined only for the variable fuel/steam utilization working condition.

For the calculation of the round-trip stack efficiency, the following assumptions have been made:

- The round-trip efficiency of the stack has been calculated considering the empirical stack efficiency of the single operation modes. In fact, it has been considered more relevant to represent the stack performances, with respect to the theoretical stack efficiency.
- It has been calculated for a defined performance range of both the SOFC and SOEC operation mode. This range has been chosen in the high current region, where the empirical performances of the stack are optimal, and the BoP consumptions can be assumed constant (because the auxiliary components are designed to work in the high-performance region of the stack).
- The round-trip stack efficiency is referred only at the stack performances in reversible working condition, and it does not take into account of the BoP and of the hydrogen storage.
- In the calculation of the round-trip efficiency of the stack, an equivalent production and consumption of hydrogen, respectively in the SOEC and SOFC mode, is assumed.
  Therefore, being the maximum current in SOFC the half of the maximum current in SOEC (reached when the OCV voltage is applied), to have the same hydrogen amount involved, if the same current flow is considered, the time of operation in SOFC mode must be double with respect to the time of operation in SOEC.
- The round-trip efficiency has been calculated only for the variable fuel/steam utilization operating condition. In fact, in the case of constant fuel/steam utilization it would not be appropriate to make a comparison of the stack efficiencies considering the same utilization factor, because the fuels involved are different (hydrogen for the SOFC and steam for the SOEC). So, the comparison based on the same value of fuel utilization would not be significative.

3.5.1 Variable fuel/steam utilization

For the determination of the round-trip efficiency, as previously said, the empirical stack efficiency has been considered in both SOFC and SOEC mode.

A working zone has been defined for both the operation modes, corresponding to the region from the 60% up to the 100% of the maximum power of the stack. In this region in fact, the stack performances are optimal, and the BoP losses can be assumed constant and low, being the components designed to work at higher current and high efficiency of the stack.
The working region considered is indicated in the figures below, for the SOFC and SOEC plot.
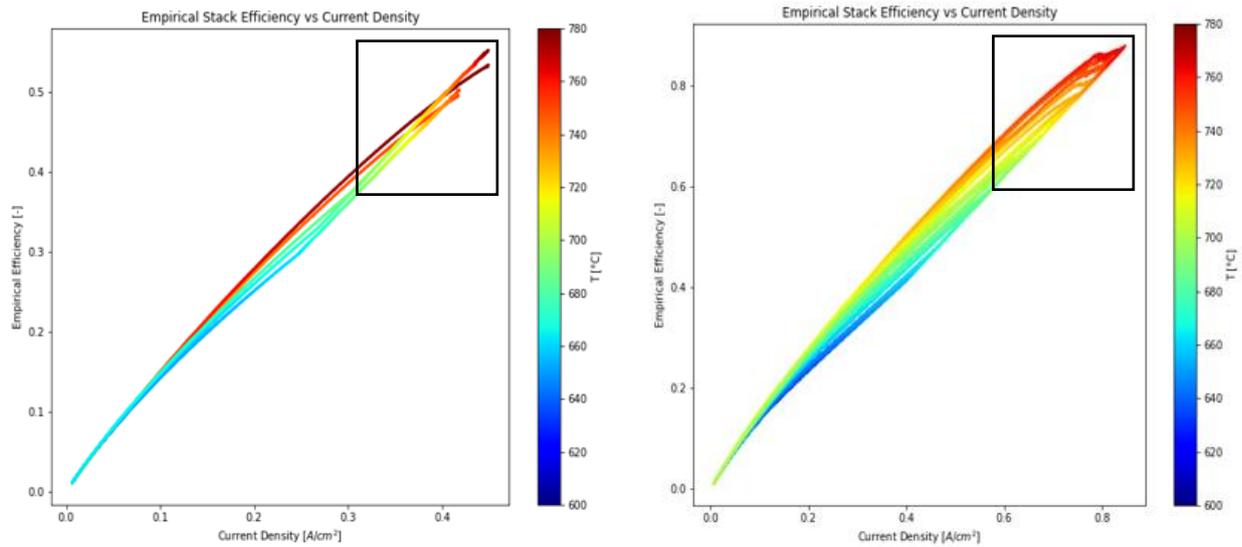
Figure 49: Empirical stack efficiency for SOFC mode (on the left) and SOEC mode (on the right), at variable fuel utilization value. In the figure is shown the typical working region for the SOFC and SOEC, usually corresponding to high current density.

In these working regions identified, the current for the SOFC is comprised between the current density 0.4 A/cm^2 and 0.3 A/cm^2, while the current for the SOEC is comprised between 0.8 A/cm^2 and 0.6 A/cm^2.

The empirical stack efficiency for the SOFC in this area varies between the 35% and the 60%, while for the SOEC it varies between the 58% and the 90%. Therefore, it is possible to define a range for the stack round-trip efficiency, though a product between the extreme values for the single SOFC and SOEC working mode. It stays in the range between the 20% and the 54%.

To this round-trip efficiency is associated an uncertainty, related to the uncertainty of the measurement instruments for the stack electric quantities and the stack flows.

Therefore, to calculate the uncertainty associated to the round-trip efficiency, firstly the uncertainty associated to the single SOFC and SOEC empirical stack efficiency has been calculated.

For the calculation of the uncertainty associated to a derived measurement, the formula expressed in the equation 62 has been used[49], in which *x,z* and *u* are the quantities involved for the *q* calculation.

| $$\frac{\delta q}{q} = \sqrt{\frac{\delta x^2}{x} + \frac{\delta z^2}{z} + .. + \frac{\delta u^2}{u}}$$ | (62) |

Being these efficiencies defined as a voltage ratio multiplied for the utilization factor, the uncertainty in their calculation will be linked to the uncertainties in the voltage and current measuring instruments and in the streams measuring instruments.

For the SOFC:

$$\frac{\delta\eta_{SOFC}}{\eta_{SOFC}} = \sqrt{\frac{\delta V^2}{V} + \frac{\delta FU^2}{FU}}$$

(63)

The voltage measuring instrument in SOFC has a relative uncertainty equal to 0.1% with respect to the measured value, while the uncertainty of the fuel utilization is calculated considering the uncertainty associated to the current flow and to the hydrogen flow measured, being the *FU* a derived quantity.

$$\frac{\delta FU}{FU} = \sqrt{\frac{\delta I^2}{I} + \frac{\delta\dot{m}_{H_2}^2}{\dot{m}_{H_2}}}$$

(64)

The relative uncertainty associated to the current measurement in SOFC is equal to the 0.2%, while the relative uncertainty of the hydrogen flow rate is equal to the 0.8% of the measured value.

Therefore, the relative uncertainty $\frac{\delta\eta_{SOFC}}{\eta_{SOFC}}$ associated to the empirical stack efficiency in SOFC is equal to the 0.8%.

For the SOEC:

$$\frac{\delta\eta_{SOEC}}{\eta_{SOEC}} = \sqrt{\frac{\delta V^2}{V} + \frac{\delta U_{steam}^2}{U_{steam}}}$$

(65)

The voltage measuring instrument in SOEC has a relative uncertainty equal to 0.1% with respect to the measured value, while the uncertainty of the steam utilization is calculated considering the uncertainty associated to the current flow and to the steam flow measured.

$$\frac{\delta U_{steam}}{U_{steam}} = \sqrt{\frac{\delta I^2}{I} + \frac{\delta\dot{m}_{H_2o}^2}{\dot{m}_{H_2o}}}$$

(66)

The relative uncertainty associated to the current measurement in SOEC is equal to the 0.2%, while the relative uncertainty of the steam flow rate is equal to the 0.6% of the measured value.

Therefore, the relative uncertainty $\frac{\delta\eta_{SOEC}}{\eta_{SOEC}}$ associated to the empirical stack efficiency in SOEC is equal to the 0.6%.

Finally, the relative uncertainty associated to the stack round-trip efficiency can be calculated with the equation below:

$$\frac{\delta\eta_{RT}}{\eta_{RT}} = \sqrt{\frac{\delta\eta_{SOFC}^2}{\eta_{SOFC}} + \frac{\delta\eta_{SOEC}^2}{\eta_{SOEC}}}$$

(67)

To the round-trip efficiency is associated a relative uncertainty equal to 1%.

4. Conclusions

In the present thesis, a Power-To-Power system has been experimentally analysed in FBK facility, to perform the stack characterization in both SOFC and SOEC operation mode.
The aim was to obtain a map of the stack performances in SOFC and SOEC mode, and, finally to characterize the stack in reversible operation, as in a Power-To-Power case study, through the round-trip efficiency calculation.

To do this, the stack has been tested separately in SOFC and SOEC mode. For each operation mode, the tests have been performed in two different working condition:

- Variable fuel/steam utilization factor
- Constant fuel/steam utilization factor

The tests performed with variable utilization factor have been performed with a control voltage strategy: the voltage has been varied in continuous through a ramp, having fixed the maximum and minimum value. The inlet fuel flow rate (or steam, in SOEC) has been maintained fixed, while the current has varied as consequence of the voltage variation. Therefore, varying the ratio between the current and the inlet fuel/steam flow rate, the utilization factor has varied for each working point, reaching the 90% for both the SOFC and SOEC operation mode. Five different stack temperatures have been analysed in SOFC and eight stack temperatures in SOEC.

On the other hand, the tests performed with constant utilization factor have been performed with a control current strategy. In this case, the current has varied automatically through a ramp, following the variation of inlet fuel/steam in the stack, in order to keep constant the ratio $\frac{I}{\dot{n}_{fuel}}$. In this way, the utilization factor has been maintained constant. The voltage in this case has varied as consequence of the current variation. Three stack temperatures have been analysed in SOFC, while four stack temperatures in SOEC mode. The stack, for both SOFC and SOEC mode, has been tested at two different constant utilization factors, equal to 40% and 80%, in order to obtain a good mapping of the stack performances in different operating conditions.
Moreover, it is to mention that the control current strategy is more critical than the control voltage one, especially in SOFC mode, in which there is a minimum voltage constraint to not exceed, to avoid the catalyst oxidation. Therefore, during the tests in control current, in SOFC, a security control has been imposed in the control system of the test bench. If the minimum voltage was reached, the test was interrupted.

The data acquired from these tests have allowed to plot the *V-I* curves and consequently, through an elaboration phase with Python, to calculate and plot the stack efficiency values and ASR values of the stack, in both the SOFC and SOEC mode.

Two different stack efficiencies have been calculated, defined theoretical and empirical. The theoretical stack efficiency has not taken into account the utilization factor and, therefore, has shown the stack performances as if all the fuel/steam reacted. The empirical stack efficiency, on the

other hand, has considered the impact of the utilization factor on the stack performances, showing the effective behaviour of the stack. For this reason, it has been considered as an empirical efficiency.

For the tests performed at variable utilization factor, the results on the efficiency analysis can be summarized as follows:

- The theoretical efficiency, for both the SOFC and SOEC mode, has shown higher values for lower current regions, in which the irreversible losses due to transport mass phenomena are lower.
- The effect of the utilization factor has been evident on the empirical efficiency trend, higher for higher currents, because of the better exploitation of the fuel/steam injected in the stack (higher utilization factor at higher current).

For the tests performed at constant utilization factor:

- The theoretical stack efficiency has shown higher values for lower current regions, as said in the case study above.
- The empirical efficiency has shown a trend similar to that of the theoretical efficiency, but with lower efficiency values, because of the not variability of the utilization factor.

However, in all the cases, the increase of temperature has had a positive effect on the performances of the stack, because of the decreasing of the overall cells resistance (ASR) and the consequent improvement of the kinetic (of the materials and of the reaction).

Finally, after having defined the performances of the stack in SOFC and SOEC operation modes, the performances of the stack in reversible operation mode have been calculated (stack round-trip efficiency).
To do this, some hypotheses have been done. The data from the tests at variable fuel utilization have been used and the empirical efficiencies in SOFC and SOEC mode have been considered, because considered more representative of the stack behaviour. A high-performance region has been individuated for both the SOFC and SOEC operation, corresponding to the high current region. The SOFC performances in this working condition stays between 35% and 60% while the SOEC's one between 58% and 90%.

Therefore, the round-trip efficiency of the stack, working in this condition, is between 20% and 54%. A relative uncertainty of 1% is associated to the round-trip efficiency value.

For what concern the system characterization, some proposals have been presented in this thesis for both the SOFC and SOEC modes. In particular, the system's study proposed aims at evaluating the electrical and thermal performances of the system, by means of the calculation of the cogeneration power and of a thermal self-sustainability analysis. The aim of the thermal self-sustainability analysis is to eliminate the electric power given in input to the system (to heat-up the

inlet streams up to the set point temperature) exploiting the heat recovered internally in the system, increasing as consequence the global system performances.

This system characterization has not been performed for the scope of this study because of technical problems to the control system of the test bench.

However, it has been presented with the perspective of future studies on the system performances in SOFC, SOEC and in reversible operation, through the calculation of the system round-trip efficiency, similarly to what has been done for the stack characterization.

Acknowledgments

References

1. Padova, U. di. Clima, le emissioni di CO2 continuano a crescere. https://ilbolive.unipd.it/it/news/clima-emissioni-co2-continuano-crescere (2019).

2. Koutroulis, A. G., Tsanis, I. K., Daliakopoulos, I. N. & Jacob, D. Impact of climate change on water resources status: A case study for Crete Island, Greece. *J. Hydrol.* **479**, 146–158 (2013).

3. *Adaptation to a Changing Climate in the Arab Countries. Adaptation to a Changing Climate in the Arab Countries* (2012). doi:10.1596/978-0-8213-9459-5.

4. Ravetti, C. School of Engineering - Classe di Ingegneria Energetica Course: Energy Economics Water, Energy & Food Nexus.

5. No Title. https://www.ilfattoquotidiano.it/2019/09/24/clima-perche-lobiettivo-e-stare-sotto-laumento-di-due-gradi/5472082/ (2019).

6. Renewable Energy Targets. https://ec.europa.eu/energy/topics/renewable-energy/directive-targets-and-rules/renewable-energy-targets_en.

7. Chiaramonti, D. School of Engineering - Classe di Ingegneria Energetica Course: Energy Economics Water, Energy & Food Nexus.

8. Green Deal europeo. https://ec.europa.eu/info/strategy/priorities-2019-2024/european-green-deal_it.

9. NextGenerationEU. https://ec.europa.eu/info/strategy/recovery-plan-europe_it#nextgenerationeu.

10. Support Scheme.

11. Marocco, P., Ferrero, D., Lanzini, A. & Santarelli, M. Optimal design of stand-alone solutions based on RES + hydrogen storage feeding off-grid communities. *Energy Convers. Manag.* **238**, 114147 (2021).

12. Shao, Y., Yin, G., Wang, Z. & Gao, Y. Proton exchange membrane fuel cell from low temperature to high temperature: Material challenges. *J. Power Sources* **167**, 235–242 (2007).

13. Wang, L. Q. *et al.* Energy efficiency of platinum-free alkaline direct formate fuel cells. *Appl. Energy* **175**, 479–487 (2016).

14. Ibrahim Dincer, C. Z. Hydrogen and Fuel Cell Systems. in *Advanced Power Generation Systems* 143–198 (2014).

15. Na, Y., Zenith, F. & Krewer, U. Increasing fuel efficiency of direct methanol fuel cell systems with feedforward control of the operating concentration. *Energies* **8**, 10409–10429 (2015).

16. Casalegno, A. et al. Low methanol crossover and high efficiency direct methanol fuel cell: The influence of diffusion layers. *J. Power Sources* **196**, 2669–2675 (2011).

17. Langnickel, H. *et al.* Efficiency analysis of 50 kWe SOFC systems fueled with biogas from waste water. *J. Power Sources Adv.* **2**, 100009 (2020).

18. Choudhury, A., Chandra, H. & Arora, A. Application of solid oxide fuel cell technology for power generation - A review. *Renew. Sustain. Energy Rev.* **20**, 430–442 (2013).

19.   Zink, F., Lu, Y. & Schaefer, L. A solid oxide fuel cell system for buildings. *Energy Convers. Manag.* **48**, 809–818 (2007).

20.   Ananyev, M. V., Farlenkov, A. S., Eremin, V. A. & Kurumchin, E. K. Degradation kinetics of LSM–YSZ cathode materials for SOFC. *Int. J. Hydrogen Energy* **43**, 951–959 (2018).

21.   Seo, H. K., Park, W. S. & Lim, H. C. The efficiencies of internal reforming molten carbonate fuel cell fueled by natural gas and synthetic natural gas from coal. *J. Electrochem. Energy Convers. Storage* **13**, 1–10 (2016).

22.   Focus.com, R. energy. FuelCell Energy and POSCO Energy open 20 MW fuel cell park in South Korea. (2017).

23.   Hydrogen - Driving green revolution. https://ec.europa.eu/info/news/focus-hydrogen-driving-green-revolution-2021-abr-14_it.

24.   Il futuro dell'idrogeno. https://dirigentindustria.it/notizie/sviluppo-sostenibile/il-futuro-dell-idrogeno.html.

25.   Manage, M. N., Hodgson, D., Milligan, N., Simons, S. J. R. & Brett, D. J. L. A techno-economic appraisal of hydrogen generation and the case for solid oxide electrolyser cells. *Int. J. Hydrogen Energy* **36**, 5782–5796 (2011).

26.   Rb, P. & Universitario, R. Politecnico di Torino Politecnico di Torino. 87316161 (2020).

27.   Anwar, S., Khan, F., Zhang, Y. & Djire, A. Recent development in electrocatalysts for hydrogen production through water electrolysis. *Int. J. Hydrogen Energy* **46**, 32284–32317 (2021).

28.   Petrushina, I. M., Christensen, E., Bjerrum, N. J., Nikiforov, A. V & Toma, A. L. Preparation and study of IrO 2 / SiC e Si supported anode catalyst for high temperature PEM steam electrolysers. **6**, 1–9 (2011).

29.   Grigoriev, S. A., Millet, P. & Fateev, V. N. Evaluation of carbon-supported Pt and Pd nanoparticles for the hydrogen evolution reaction in PEM water electrolysers. *J. Power Sources* **177**, 281–285 (2008).

30.   Senthil Kumar, S. M. *et al.* Hydrothermal assisted morphology designed MoS2 material as alternative cathode catalyst for PEM electrolyser application. *Int. J. Hydrogen Energy* **41**, 13331–13340 (2016).

31.   Nikiforov, A. V., Petrushina, I. M., Christensen, E., Tomás-García, A. L. & Bjerrum, N. J. Corrosion behaviour of construction materials for high temperature steam electrolysers. *Int. J. Hydrogen Energy* **36**, 111–119 (2011).

32.   Soriano Moranchell, F. A. *et al.* Electrodes modified with Ni electrodeposition decrease hexavalent chromium generation in an alkaline electrolysis process. *Int. J. Hydrogen Energy* **45**, 13683–13692 (2020).

33.   Cruden, A., Infield, D., Kiaee, M., Douglas, T. G. & Roy, A. Development of new materials for alkaline electrolysers and investigation of the potential electrolysis impact on the electrical grid. *Renew. Energy* **49**, 53–57 (2013).

34.   Xie, Y., Xiao, J., Liu, D., Liu, J. & Yang, C. Electrolysis of Carbon Dioxide in a Solid Oxide Electrolyzer with Silver-Gadolinium-Doped Ceria Cathode. *J. Electrochem. Soc.* **162**, F397–F402 (2015).

35. Kaur, G., Kulkarni, A. P. & Giddey, S. CO_2 reduction in a solid oxide electrolysis cell with a ceramic composite cathode: Effect of load and thermal cycling. *Int. J. Hydrogen Energy* **43**, 21769–21776 (2018).

36. Li, H. *et al.* Chromate cathode decorated with in-situ growth of copper nanocatalyst for high temperature carbon dioxide electrolysis. *Int. J. Hydrogen Energy* **39**, 20888–20897 (2014).

37. Chauveau, F., Mougin, J., Bassat, J. M., Mauvy, F. & Grenier, J. C. A new anode material for solid oxide electrolyser: The neodymium nickelate Nd2NiO4+δ. *J. Power Sources* **195**, 744–749 (2010).

38. Berger, C., Bucher, E., Gspan, C. & Sitte, W. Crystal structure, oxygen nonstoichiometry, and mass and charge transport properties of the Sr-free SOFC/SOEC air electrode material La 0.75 Ca 0.25 FeO 3-δ. *J. Solid State Chem.* **273**, 92–100 (2019).

39. Vialetto, G., Noro, M., Colbertaldo, P. & Rokni, M. Enhancement of energy generation efficiency in industrial facilities by SOFC – SOEC systems with additional hydrogen production. *Int. J. Hydrogen Energy* **44**, 9608–9620 (2019).

40. Ferrero, D., Lanzini, A., Leone, P. & Santarelli, M. Reversible operation of solid oxide cells under electrolysis and fuel cell modes: Experimental study and model validation. *Chem. Eng. J.* **274**, 143–155 (2015).

41. Momma, A., Kato, T., Kaga, Y. & Nagata, S. Polarization behavior of high temperature solid oxide electrolysis cells (SOEC). *J. Ceram. Soc. Japan* **105**, 369–373 (1997).

42. Mottaghizadeh, P., Santhanam, S., Heddrich, M. P., Friedrich, K. A. & Rinaldi, F. Process modeling of a reversible solid oxide cell (r-SOC) energy storage system utilizing commercially available SOC reactor. *Energy Convers. Manag.* **142**, 477–493 (2017).

43. Frank, M., Deja, R., Peters, R., Blum, L. & Stolten, D. Bypassing renewable variability with a reversible solid oxide cell plant. *Appl. Energy* **217**, 101–112 (2018).

44. Khalili, M., Karimian Bahnamiri, F. & Mehrpooya, M. An integrated process configuration of solid oxide fuel/electrolyzer cells (SOFC-SOEC) and solar organic Rankine cycle (ORC) for cogeneration applications. *Int. J. Energy Res.* **45**, 11018–11040 (2021).

45. Butera, G., Jensen, S. H. & Clausen, L. R. A novel system for large-scale storage of electricity as synthetic natural gas using reversible pressurized solid oxide cells. *Energy* **166**, 738–754 (2019).

46. Peters, R. *et al.* Long-Term Experience with a 5/15kW-Class Reversible Solid Oxide Cell System. *J. Electrochem. Soc.* **168**, 014508 (2021).

47. ComESto project. http://www.comesto.eu/#Il-Progetto.

48. Laoun, B. Thermodynamics aspect of high pressure hydrogen production by water electrolysis. *Rev. des Energies Renouvelables* **10**, 435–444 (2007).

49. Taylor, J. R. Introduzione all'analisi degli errori. (2000).